VRIJE
UNIVERSITEIT
BRUSSEL

Thesis submitted in order to obtain the degree of master in Physics and Astronomy

THE STANDARD MODEL STRIKES BACK: SEARCHING FOR SEXAQUARK DARK MATTER AT THE LHC

Florian Partous

June 7, 2018

Promotor: Prof. Dr. Steven Lowette

Sciences and Bio-Engineering Sciences

Abstract

This Master thesis forms an initial feasibility study into the discovery at the LHC of the recently hypothesized stable six-quark bound state referred to as the Sexaquark, using the tools of and data collected by the CMS collaboration. The stable Sexaquark, or in short S, was proposed in august 2017 by G. Farrar in [1] and is being considered as a Standard Model dark matter candidate. Could the Standard model be making a comeback?

This work focuses on one possible way to detect this newly hypothesized bound state leveraging CMS data as well as Monte Carlo simulations. A detection strategy involving the material interactions of the S with neutrons in the CMS detector is used, giving rise to kaons and lambda baryons, which in turn decay to final state pions and protons. An investigation into the potential backgrounds involving those same final state particles is conducted, as well as a discussion of reconstruction efficiencies of those final state particles. The definition of background-discriminating cuts, followed by an S mass distribution bump hunt in 150 million events of Single Muon triggered data then becomes the goal of this work. At the end a $pp \to \bar{S}$ production cross section upper limit is estimated and compared to a previous estimation made by G. Farrar.

We conclude that no signal was seen and an upper limit, at a 95% confidence level, of the $\bar{S}$ production cross section is estimated to be $\sigma\left(pp \to \bar{S}\right) = 43\text{mb}$, which is still larger than G. Farrar's original estimate.

This work was highly off the beaten track. This is to our knowledge currently the only search for the stable Sexaquark at the LHC. We had to develop our own methods and tools through the process of trial and error in order to arrive at our current results. This had to be accomplished within the short few months that encompasses a master thesis, which presented an interesting challenge. For the first time with real data, a demonstration was given of the feasibility of a search of a low-mass signal in CMS pileup collisions.

Contents

Acknowledgments

I would first like to thank my thesis advisor and promotor Prof. Dr. Steven Lowette of the Vrije Universiteit Brussel. The door to Prof. Lowette's office (and e-mail) was always open whenever I ran into a trouble spot or had a question about my research or writing. He consistently allowed this paper to be my own work, but steered me in the right the direction whenever he thought I needed it. Prof. Lowette's willingness to give his time so generously has been very much appreciated. I am gratefully indebted to him and would not have been able to do this without him.

I would also like to thank the experts who were involved in this research project, Jarne De Clercq (PhD student at the VUB) and Prof. Dr. Ir. Pascal Vanlaer of the Université Libre de Bruxelles (ULB) for their valuable and constructive suggestions as well as for their excellent guidance during the planning and development of this thesis. Without their passionate participation and input, this work could not have been successfully completed.

I would also like to acknowledge Prof. Dr. Glennys Farrar for the insightful discussion and for coming up with the concept of the Sexaquark, the central topic of this thesis, in the first place.

Finally, I must express my very profound gratitude to my parents, brother, sister and of course my cat for providing me with unfailing support and continuous encouragement throughout my years of study and through the process of researching and writing this thesis. This accomplishment would not have been possible without them. Thank you.

Florian Partous

Chapter 1

Introduction

This chapter gives an introduction into the idea of exotic hadrons, a family of particles which the Sexaquark is the newest member of. Next up follows a more detailed explanation of what precisely a Sexaquark is, some of the history behind it as the so–called H-dibaryon, some of the general experimental strategies proposed to find the particle, and how the S is being considered as a dark matter candidate. This last part will only be touched upon very briefly, as it lies beyond the scope of this thesis. All of this closely follows the original work by G. Farrar.

1.1 Mesons, baryons and exotic hadron

Baryons are composite subatomic particles that consist of a bound state of three quarks. They are triquarks, as opposed to mesons, which are composed of one quark-antiquark pair. Baryons and mesons are part of the category of particles referred to as hadrons, which are quark-based particles in general.

As quark-based particles, baryons couple to the strong interaction, whereas leptons do not. The most familiar baryons are the protons and neutrons that make up most of the mass of the visible matter in the universe.

Each baryon has a corresponding antibaryon where the quarks are replaced by their corresponding antiquarks.

Quarks have baryon numbers of $B = 1/3$ and antiquarks have baryon numbers of $B = -1/3$. Baryons, being made of three valence quarks, have baryon number $B = 1/3 + 1/3 + 1/3 = 1$.

Over the years more exotic hadrons, which are in principle allowed by QCD (the quantum field theory describing the strong interactions), have been proposed. These include the tetraquarks, which are an exotic meson composed of four valence quarks. Several tetraquark candidates have been discovered by particle physics experiments in the last few decades. Most of the time the quark content of these states are $q\bar{q}Q\bar{Q}$, where q is a light (up, down or strange) quark and Q a heavy (charm or bottom) quark.

Next to that, hadrons made of four quarks and one antiquark ($qqqq\bar{q}$), the so-called pentaquarks, have also been proposed, although several claimed experimental observations have been contested. These exotic hadrons have baryon number $B = 1/3 + 1/3 + 1/3 + 1/3 - 1/3 = 1$. More recently, in July 2015, the LHCb collaboration announced the observation of two resonances consistent with pentaquark states in the $\Lambda_b^0\,(udb) \to J/\psi\,(c\bar{c})\,K^-\,(s\bar{u})\,p\,(uud)$ decay channel, with a combined statistical significance of 15 standard deviations. These pentaquarks are referred to as $P_c^+(4380)$ and $P_c^+(4450)$ and have quark content $uudc\bar{c}$ [4].

In principle, particles with higher quark content, such as the heptaquarks ($5q + 2\bar{q}$), nonaquarks ($6q + 3\bar{q}$), etc. could also exist. The question remains whether or not those form a bound state.

This thesis discusses the case in which a sexaquark bound state might exist, which is potentially stable, and which has been argued to be a potential dark matter candidate.

1.2 Stable Sexaquark

The *uuddss* sexaquark, from now on referred to as the 'S', is a hypothesized six-quark deeply bound state, recently proposed by R. Farrar in august 2017 in [1] and previous work. The proposed S is a spin-0, flavor-singlet, parity-even boson which is electrically neutral $Q = 0$, has baryon number $B = 2$ and strangeness $S = -2$ (due to it containing two strange quarks).

The reason the S consists of *uuddss* specifically is because this quark content allows the wavefunction's symmetries to play out very favorably for the stability of the S. More precisely, the spatial part of the S wavefunction can be fully symmetric, while simultaneously allowing the color, flavor, and spin wavefunctions to be totally anti-symmetric. This is the only 6-light-quark state for which this is the case. Farrar gives the example of the deuteron, which consists of six quarks as well, but is not spatially symmetric and behaves more like a loosely bound pair of nucleons as compared to the S which can be better thought of as a single, spatially symmetric 'buckyball' of quarks.

These wavefunction symmetry arguments render the S to be the most tightly bound state of its class, in the same way as to how the singlet hyperfine state in hydrogen is lower in energy than the triplet state.

The idea of *uuddss* being potentially a bound state was already noticed by R. Jaffe in 1977, where he used a simplified 1-gluon-exchange bag model calculation to conclude the *uuddss* state, then referred to as the H-dibaryon, to have a mass of approximately 2150MeV [5].

Using this mass, $m_{H-dibaryon} > m_p + m_e + m_\Lambda$, resulting in the H-dibaryon to have a very short lifetime determined by the weak interaction scale at $\sim 10^{-10}$ seconds.

Experiments never found sign of the existence of such a H-dibaryon state, in fact strong evidence against its existence was found [6, 7, 8, 9, 10, 11, 12]. This includes experiments looking for decays of the H-dibaryon, experiments which ended up restricting $m_{H-dibaryon} > 2$GeV to avoid neutron background, experiments requiring fast production in $S = -2$ hyper-nuclei, and fixed-target experiments where the H ends up being hard to produce. The $m_{H-dibaryon} > 2$GeV limit put on the H mass by certain experiments makes such experiments blind to the expectation for the mass to be below 2GeV, as discussed below, in order to assure stability.

G. Farrar argues that, instead of being a fairly loosely bound system, the S might be a much more deeply bound, essentially stable state due to it having a relatively low mass. The fact that the S might be stable as compared to the short lived H-dibaryon makes all previous searches for the *uuddss* state, such as the ones looking for H-dibaryon decays, irrelevant.

Due to baryon number conservation, the S would be fully stable if $m_S \leq 2\,(m_p + m_e) = 1877.6$MeV and would decay through doubly weak decay if $m_S < m_p + m_e + m_\Lambda = 2054.5$MeV, in the latter case giving it a lifetime greater than the age of the universe and making the S essentially stable [13]. This last inequality will in this thesis be used as a motivation to restrict our search for the S to masses below the 'essentially stable' threshold of 2GeV.

Lattice QCD simulations are still far from being accurate enough to either confirm or exclude the existence of the stable S. This technique uses quark masses well above their real value, making the simulations non-relativistic. In certain cases extrapolations can be used to extrapolate the hadrons consisting of those quarks to the physical quark mass limit. Unfortunately these extrapolation schemes are not available in the case of the six-quark S. This leaves currently the only way to confirm its existence to be through experiment.

A clear empirical analog for estimating the S mass based on other hadron masses does not exist. Due to the S being a scalar, chiral symmetry breaking arguments have no obvious implications for m_S [1]. Furthermore, m_S has no a priori relation to the masses of more familiar baryons. For example, the 6-quark combination $K^- \bar{K}^0 \pi^+$ has the same quark flavor content as the S, and total mass 1131MeV, but since these mesons are so-called pseudo-Goldstone bosons[1] while the S is not, there is no reason to assume the same mass for the S.

[1] Pseudo-Goldstone bosons arise in a QFT with both spontaneous and explicit symmetry breaking.
In the absence of an explicit breaking, spontaneous symmetry breaking gives rise to massless Nambu–Goldstone bosons for the exact spontaneously broken chiral symmetries. The chiral symmetries discussed however are only approximate symmetries, given their small explicit breaking. A more detailed explanation is beyond the scope of this thesis. For more information the author refers the reader to [30].

A stable sexaquark state is generally considered to be implausible by particle physicists, due to the unjustified intuition rooted in the oversimplified constituent quark model: the rule-of-thumb that for each valence light (strange) quark, an effective mass of $\sim 300\,(450)$ MeV should be added. This rule-of-thumb correctly approximates the ground-state octet and decuplet baryon masses, but due to reasons discussed in [1] can not be reliably extended to the 6-quark case. Reasons include that this naive quark model does not take into account the possible presence of pseudo-Goldstone bosons in the case of chiral symmetry breaking for pseudoscalars, the potential presence of chiral anomalies, the subtleties of relativistic dynamics in different spin or flavor combinations of quarks and gluons, the presence of non-perturbative gluons and quark dynamics, etc...

Farrar points out that, due to the invalidity of the naive but familiar rules-of-thumb, one should keep an open-mind towards the potential value of m_S.

Barely 16% of the binding energy relative to two Λ's is in fact sufficient for the S to be absolutely stable with only 10% or less for it to be essentially stable [13]. These are small binding energy contributions to the S mass compared to the *O(1)* mass differences in the meson sector between reality and what the naive quark model predicts.

From all of the aforementioned, it is reasonable to expect such a small, sub-2GeV S mass and searches for a stable S are sufficiently motivated.

1.3 Stable S as dark matter candidate

A stable or effectively stable S could potentially be a good dark matter candidate as pointed out in [1]. Current direct detection limits are in general inapplicable. Reasons include S scattering on Galactic disk gas, driving the S dark matter towards approximately co-rotating with the solar system, hence yielding a too small relative velocity of the dark matter wind to make the observable energy deposits in direct detection experiments feasible.

As discussed in [1], S dark matter could possibly resolve issues like the star-formation-quenching problem of ΛCDM and problems with primordial nucleosynthesis limits on unseen baryons (S do not form nuclei). Furthermore, the S could satisfy relic abundance, explaining the $\Omega_{DM}/\Omega_B \sim 5$ ratio. S dark matter could alleviate astrophysical problems like baryon asymmetry, core-versus-cusp, too-big-to-fail, exceptional galactic rotation curves, Hubble constant discrepancies, etc. All these points are hypothetical and should be considered as highly speculative at this moment.

Whether or not S could be a good dark matter candidate and which astrophysical problems it would or wouldn't solve is however outside of the scope of this thesis and will not be discussed in further detail. The interested reader is directed to Farrar's main paper [1] and its sources.

1.4 S production in baryon collisions

The production of S in baryon collisions and the stability of nuclei in regards to decaying to S depend on the wavefunction overlap between the S and the baryons.

As G. Farrar explains, how to model S and $\bar{S}$ production in hadronic (in our case proton-proton) interactions depends on the conditions. In low multiplicity interactions at relatively low energy, the overlap $|\mathcal{M}|_{BB'\to S}$ is small, but the suppression of the overlap reduces as the relative momentum between the baryons increases.

In high-multiplicity inclusive reactions, the production rate could be estimated (although this is a very rough assumption) by assuming a cost of 10^{-1} of the pion production rate per quark [1]. Baryons for example get a 10^{-1} suppression factor compared to mesons (pions). Blatantly extrapolating this rule-of-thumb up to six quarks would suggest an S production rate in hadronic interactions of roughly $10^{-4} - 10^{-6}$ relative to pions. Given this estimate for the production rate relative to pions, S should be fairly often produced in high-energy baryon collision experiments, such as at the LHC.

Given the inclusive inelastic cross section in proton-proton collisions at $\sqrt{s} = 13$TeV is 80mb, with an average production of about 6 hadrons (mostly pions) per unit of rapidity. This cor-

responds to an estimated S production cross section[2] between $2.4 \cdot 10^{-1}$ and $2.4 \cdot 10^{-3}$mb [39]. Meaning that even with the 10^{-6} suppression factor, the LHC could still be producing significant amounts of S particles, guesstimated[3] to be up to 26kHz.

This production rate was however not sufficient for the S to have been noticed so far. The production rate of neutrons would be a factor 10^3 to 10^5 larger than that of the S. On top of that neutrons behave in a very similar way as the S: they are electrically neutral, reside in the same mass range and have a relatively low, yet much higher compared to the S interaction probability with material in most detectors.

Interaction with S or $\bar{S}$ would therefore have been easily confused with an occasional, uninteresting hadronic interaction of a neutron or anti-neutron.

Another important phenomenological property for this S particle that results in the search for the S to be difficult it that it has a small spatial extent, of the order of 0.4fm at most. Given $m_S \approx 2$GeV, the S Compton wavelength is of the order of $\lambda = {}^{h}/_{m_S \cdot c} \approx 0.1$fm. Unlike for nucleons however, a pion cloud giving them a spatial extent of 0.9fm is not present in the case of the S.

Finally, another hurdle is the fact that there is no coupling to photons (the S being neutral), nor to pions, and to most other mesons.

[2]This was estimated in the following way: 5 units of rapidity $\cdot$ 6 hadrons = 30 hadrons per pp collision within acceptance ($\eta \in [-2.5; 2.5]$). Then 80mb $\cdot$ 30 hadrons $\cdot 10^{-4 \text{ to } -6}$ results in $2.4 \cdot 10^{-1}$ to $2.4 \cdot 10^{-3}$mb.

[3]Estimated in the following manner: Bunch crossing rate $\cdot$ average pile-up in 2016 $\cdot$ number of hadrons per pp collision within acceptance $\cdot 10^{-6}$ suppression = $32\text{MHz} \cdot 27 \cdot 30 \cdot 10^{-6} \approx 26$kHz

Chapter 2

The LHC and the CMS experiment

2.1 Luminosity, cross section and related concepts

Luminosity ($\mathcal{L}$) is one of the most central parameters of any accelerator experiment.

It is a measurement of the number of collisions that could potentially occur in a detector per unit of area, per unit of time. The larger its value, the larger the number of collisions that could take place. To calculate this number, one needs to consider the interaction cross sections involved.

The luminosity in a proton-proton accelerator experiment can be determined semi-qualitatively using the following variables [32]:

- The number of protons per bunch squared, N^2, because every one of the N particle in one bunch could interact with one of the N particles in the other bunch.
- The elapsed time between consecutive bunches: t
- S_{eff}, the effective section of collision that depends on the cross section of the bunches. This is 'effective' because the beam profile does not have an ideally flat, sharp front. It is determined in the following manner: $S_{eff} = 4\pi\sigma^2$, where $\sigma = 16\mu$m is the transversal size of the bunch at the interaction point.
- $F \leq 1$, the geometric luminosity reduction factor because of the crossing angle at the interaction point. This can be taken to be approximately equal to 1.

Putting these together results in $\mathcal{L} \sim \frac{N^2}{t \cdot S_{eff}}$. Plugging in values of $N^2 \approx \left(1.15 \cdot 10^{11}\right)^2$, $t = 25$ns and $S_{eff} = 4\pi \left(16 \cdot 10^{-4}\right)^2 \text{cm}^2$ gives a luminosity of approximately $\mathcal{L} \sim 10^{34} cm^{-2}\,\text{s}^{-1}$ [32].

The integrated luminosity, $\mathcal{L}_{int}$, is the total luminosity integrated over a period of time Δt.

The cross section (σ) is a measurement of the probability that an event occurs [33]. In the case of an interaction cross section, this event would be the interaction of two particles, such as protons. Cross sections are measured in 'barns', where $1\text{b} = 10^{-24}\text{cm}^2$.

The number of events per unit time ($N_{ev/time}$) for a specific process is determined by $N_{ev/time} = \mathcal{L} \cdot \sigma$. The total number of events that occurred over a period Δt is given by $N_{ev} = \mathcal{L}_{int} \cdot \sigma$.

The total proton-proton interaction cross section can be broken down in contributions from the inelastic cross section, the diffractive cross section and the elastic cross section. The last two will lead to events that are not visible by the detectors. It is only the inelastic scatterings that produce particles at sufficiently large angles with respect to the beamline, and are therefore able to hit the detectors, that are visible.

2.2 The Large Hadron Collider

Constructed at CERN in a 27km long, 50 to 175 meter deep tunnel, the Large Hadron Collider aims to probe the TeV energy scale as the world's largest particle collider. Originally, one of the main scientific goals of the LHC was towards demystifying the electroweak symmetry breaking mechanism by means of searching for the in the Standard Model postulated Higgs boson.

The collider has been constructed to accelerate and collide protons at centre-of-mass energies of approximately 14TeV, and to achieve an instantaneous luminosity of more than $10^{34}\text{cm}^{-2}\text{s}^{-1}$. The counter-rotating proton bunches are separated by a mere 25ns, giving rise to a bunch crossing rate equalling 40MHz.

The LHC began operating as of 2010 at $\sqrt{s} = 7\text{TeV}$. Following this, in 2011 the number of bunches making up the beams was raised to 1380, changing the separation between the bunches to 50ns, and giving rise to a significant increase in the luminosity. The centre-of-mass energy was then increased to 8TeV in 2012, and during that time period the luminosity was also further raised, reaching maximum luminosities of near $7 \cdot 10^{33}\text{cm}^{-2}\text{s}^{-1}$.

In 2011 and during the first months of data taking in 2012, the data accumulated by the CMS experiment, corresponding to slightly more than 5fb^{-1} per year, was analyzed, which resulted in the first observation of the Higgs boson.

Important concepts The CMS experiment, and hence this work, uses a right-handed coordinate system, with the origin at the center of the detector, the x-axis pointing to the center of the LHC ring, the y-axis pointing up (perpendicular to the plane of the LHC ring), and with the z-axis along the anticlockwise-beam direction.

An important experimental variable at CMS or the LHC in general is the pseudorapidity η, defined as $\eta = -\ln(\tan(\theta/2))$, where θ is the polar angle measured from the anticlockwise beam direction. Indicated by ϕ is the azimuthal angle, measured relative to the x-axis in the xy-plane. The component of momentum perpendicular to the beam axis is called the transverse momentum, p_T.

There is also the so-called pileup effect. A detected event often contains signals from multiple proton-proton collision. Due to the high proton beam intensity, multiple proton-proton collisions can take place for each bunch crossing. The mean number of p-p collisions per bunch crossing was approximately 14 in 2015 and was raised to roughly 27 by 2016.

2.3 The CMS experiment

CMS (Compact Muon Solenoid) is one of the two general purpose experiments in operation at the LHC at CERN. Having been designed as a general-purpose detector, CMS can very precisely identify and reconstruct photons, muons, electrons, hadronic jets, and the missing of transverse momentum, carried away by weakly interacting particles. CMS consists of multiple sub-detectors, each making use of different technologies, calibration and reconstruction methods. See figure 2.1a for a schematic illustration of the detector's setup.

The backbone of CMS is a superconducting solenoid, which gives rise to an axial magnetic field of 3.8T. Both the central tracker and the calorimeters are positioned inside the bore of the solenoid. The steel flux return yoke outside the solenoid is filled with gas ionization detectors which are used to detect and reconstruct muons. Trajectories of electrically charged particles are measured by a silicon pixel and strip tracker. This instrument has full coverage within a pseudo-rapidity range of $|\eta| < 2.5$.

A hadronic calorimeter, HCAL, and an electromagnetic calorimeter, ECAL, surround this tracking region and covers a range of $|\eta| < 3$.

Next to that, there is a pre-shower detector covering the area in between $1.65 < |\eta| < 2.6$. The pre-shower detector is capable of recording the x, y position of incoming particles through two planes of silicon sensors, as well as discriminate between single photons and photons resulting from high-energy neutral pions. Finally, the coverage of the calorimeter is enlarged up to $|\eta| < 5.0$ by the Cherenkov forward calorimeter.

The following section describes the layout and workings of the central tracker in more detail. This apparatus, as opposed to the others, is the most important one for this work.

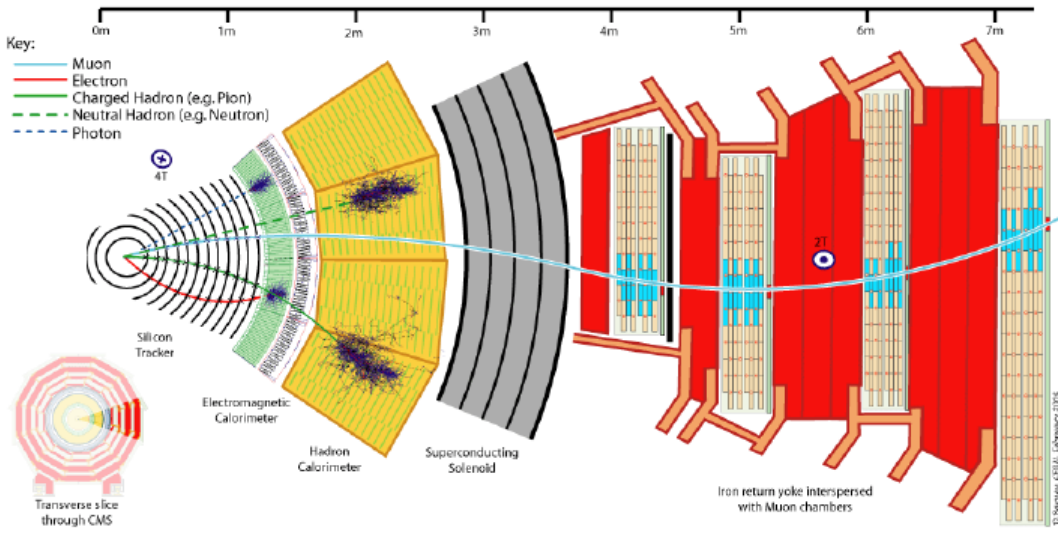

(a) Illustration of the detection of particles at the CMS experiment. Each type of particle leaves its characteristic trace in the various subdetectors of the experiment. This enables identification of different particles as well as the measurement of their energies and trajectories. Source: [34]

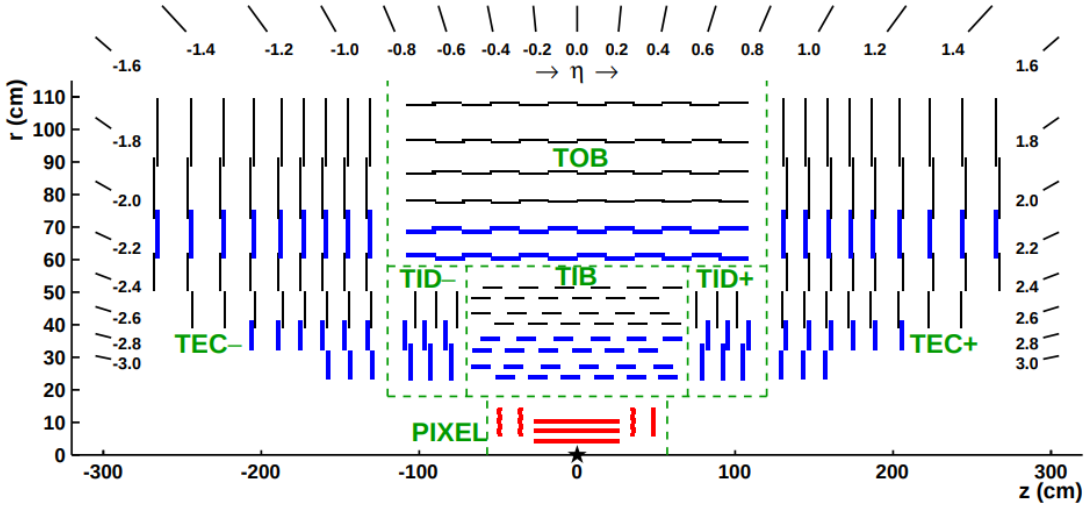

(b) This figure shows a schematic cross section of the CMS tracker in the r-z plane. In this plane, the tracker is symmetric about the $r = 0$ axis. Here only the top half is depicted. The center of the tracker, which approximately lines up with position of the proton-proton interaction point, is indicated by the black star. The green dashed lines separate which modules belong to which named tracker subsystems. The thin, black lines represent the the strip tracker modules that provide 2D hits. Strip tracker modules that allow the reconstruction of 3D hit positions are represented by thicker, blue lines. These last modules actually each consist of two back-to-back positioned sub-modules, where one of the sub-module is rotated by a 'stereo' angle. The red lines indicate the layout of the pixel modules, which support 3D hits positions as well. Within each layer of strip modules, every individual module is shifted slightly in the r or z direction relative to its neighboring modules. This allows the neighboring modules to overlap one another, avoiding any gaps in the tracker acceptance. Source: [25]

Figure 2.1

2.3.1 The CMS tracker

A schematic illustration of the CMS tracker can be found in figure 2.1b.

The CMS tracker [34, 35] encompasses a cylindrically shaped volume with a length of 5.8m and a diameter of 2.5m. The cylinder's axis is approximately aligned with the LHC beamline. The CMS solenoid provides a uniform, co-axial magnetic field of 3.8T which permeates the tracker.

The tracker houses a large silicon strip tracker with inside of it a small silicon pixel tracker. In the mid-pseudorapidity general direction, the pixel tracker consists of three co-axially aligned barrel layers at radial distances ranging from 4.4cm to 10.2cm. The strip tracker on the other hand encompasses ten co-axially aligned barrel layers reaching outwards to a radial distance of 110cm. Both sub-detector systems are extended by endcaps on both sides of the barrel. The endcaps have as goal to extend the tracker acceptance up to a pseudorapidity range of $|\eta| < 2.5$.

The pixel detector enables 3D position measurements of the hits caused by interactions of charged particles with the sensors. It does this with a tremendous resolution of about 10µm in the transverse direction and 20–40µm in the longitudinal direction. The third coordinate is determined through the position of the sensor plane.

In total, the pixel detector's 1440 modules sum up to an area of about 1m^2 and consists of about 66 million pixels, while the strip tracker consists of 15148 silicon modules, covering a total area of approximately 198m^2 and containing up to 9.3 million strips.

The strip tracker is divided into four subsystems. The Tracker Inner Barrel (TIB) and Disks (TID) which are itself composed of four barrel layers and an additional three disks at the ends. The Tracker Outer Barrel (TOB) consists of six barrel layers. Finally there is the Tracker EndCap (TEC), which is composed of nine disks, each containing up to seven concentric rings with silicon strip modules.

The modules of the pixel detector use silicon with a thickness of 285μm, while each pixel cell has a size of $100 \times 150\mu\text{m}^2$ in $r\phi \times z$. Because of this the resolutions in the $r\phi$ plane are roughly the same as the resolution in the z direction. The modules in the TIB, TID, TEC and TOB use silicon that ranges in thickness between 320μm and 500μm.

In the barrel, the silicon strips usually run parallel to the beam axis. Many of the modules in the TIB, TOB, TID and the TEC have a second strip detector module mounted back-to-back to the first. This second module is rotated in the plane of the first module over a so-called 'stereo' angle of 100 milliradians. The hits from these two modules are then matched and combined into a measurement of the second coordinate, which is the z direction in the barrel and the r direction on the disks.

The tracker is expected to be traversed by at least 1000 charged particles at each bunch crossing, assuming pile-up condition of more than twenty proton–proton interactions.

Figure 2.2 shows a simulation estimate for the tracker material 'budget', in units of radiation lengths and nuclear interaction lengths. The latter provides an indication for the distribution of nuclear interactions in the tracker.

2.4 Track and vertex reconstruction

Track and vertex reconstruction make use of the previously described system of silicon pixel and microstrip sensors. Even at the enormously high expected fluxes of charged particles resulting from the proton-proton collisions, the high granularity of the sensors will result in a low occupancy. Due to the good single point resolution a high momentum resolution and accurate extrapolation of charged particle trajectories to the interaction region can be achieved. This enables the accurate reconstruction of primary and secondary vertex positions, as well as the identification of the decays of long-lived particles [36].

As mentioned before, the CMS detector has to deal with large amounts of pile-up of 20 simultaneous proton-proton collisions and more. It is a challenge to do track reconstruction in such high-occupancy environments, to keep up a high track-finding efficiency, at the same time keeping the percentage of fake tracks under control. Fake tracks are faultily reconstructed tracks. These could be formed from a faulty combination of unrelated hits or from genuine particle trajectories that are incorrectly reconstructed by including of false hits. Next to that, the tracking

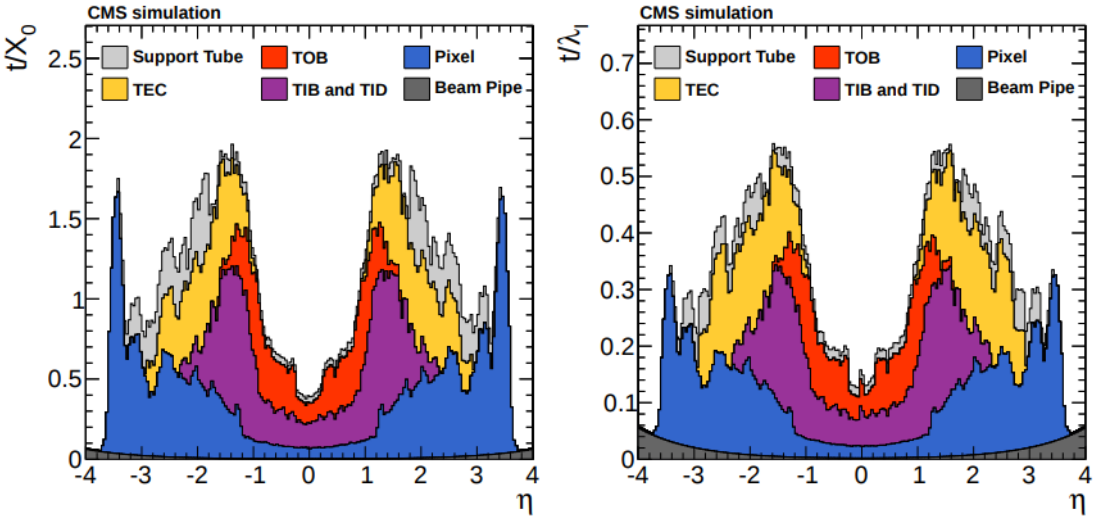

Figure 2.2: Total thickness t of the tracker material traversed by a particle produced at the interaction point, as a function of pseudorapidity, given in units of radiation length X_0 on the left and in units of the nuclear interaction length λ_I on the right. The thickness distribution is broken up into the contributions to the total 'material budget' of each of the subsystems that make up the CMS tracker, as well as the beam pipe and the support tube that surrounds the tracker.[34]

software has to run sufficiently fast to be able to support the offline event reconstruction (which processes several billions of events per year), as well as the CMS High Level Trigger (HLT), which runs at rates of up to 100kHz [25].

High reconstruction efficiencies is a high priority of the CMS experiment, it is essential to any of its scientific goals. For example, good tracks reconstruction efficiency down as low as $p_T \sim 100$MeV is needed for investigating hadron production rates and for obtaining optimal jet energy resolution [25]. The ability to resolve nearby tracks is also essential to the study of many processes. On top of that, high resolutions on impact parameter distances is essential for e.g. an accurate measurement of the primary proton-proton interaction vertex positions.

2.4.1 Track reconstruction

Charged track reconstruction is done in three main stages [36].

Stage 1 is the generation of seeds used for further reconstruction. A seed is based on a pair of hits that passed a certain selection, such as compatibility with the interaction region, and a lower p_T limit, where multiple scattering is taken into consideration. An ideal seed consists of three hits, since three hits are needed to fix a circle's parameters (the transverse part of a helix), although a seed consisting of two hits plus a beamline constraint is used as well. Low occupancy and the 2D position information being unambiguous make the pixel layers the optimal place for seeding.

Stage 2 uses, based on the seed, an initial estimation of the track parameters. This is done using a Kalman filter method: given the current parameters, the trajectory is extrapolated to the next layer and compatible hits are selected based on the χ^2 between the predicted and measured positions. The predicted parameters are updated using each of these hits which results in new set of trajectory candidates. A quality filter is then applied to cut out poor candidates. The best ones are then used for further propagation.

Stage 3 employs a χ^2 Kalman filter fit for the final estimation of the track parameters. This can be done in two different ways. A 'forward' fit proceeding outwards from the interaction region removes the approximations used in the track finding stage and provides an optimal estimate of the track parameters at the outside of the tracker. A 'backwards' fit in the opposite direction yields the estimate of the track parameters in the interaction region. A combination of both methods is used to determine the parameters at the intermediate layers.

2.4.2 Vertex reconstruction

Vertex finding and fitting is also done using the Kalman filter [36].

The process usually consists of two steps: vertex finding followed by vertex fitting. The first step involves grouping together tracks into vertex candidates. The vertex-finding algorithms depends on the specific physics case considered, for example primary or secondary vertex fitting, reconstruction of exclusive decays, etc. Vertex fitting for a given set of tracks involves determining the best estimate of the vertex parameters, such as the position and covariance matrix. In addition to that, certain indicators of the fit quality, such as total χ^2, are to be determined.

Vertex fits have to take into account the possible confusion of the associated tracks of particles originating from other vertices. The standard versions of a vertex fitter are the 'trimmed Kalman vertex fitter' (TKF) and the 'adaptive vertex fitter' (AVF). In this last one a weight is assigned to each track as a function of its χ^2. For complex events the AVF has been shown to yield a slightly better vertex position resolution and to be faster than the TKF [36].

Primary vertex candidates are obtained by clustering a certain set of tracks along the beam line. This set of tracks is selected based on the impact parameter significance and p_T. Vertex candidates are fitted and filtered according to their compatibility with the beamline and their χ^2. The efficiency for reconstructing and correctly tagging the PV of the signal event depends on the number of charged tracks originating at the vertex.

The TKF or AVF methods can then be used for secondary vertex reconstruction. A selection based on the distance to the primary vertex is used to validate them. After a first fit to the complete set of tracks the ones compatible with the vertex candidate are removed. This is done in an iterative fashion with the tracks incompatible with the vertex at previous iterations.

2.4.3 Kinematic fit

Certain kinematic constraints, such as energy and momentum conservation, are central to all kinematic particle physics processes. However, due to the uncertainties in the measured quantities, these constraints are not exactly fulfilled.

Kinematic fitting is a scheme in which one uses the physics constraints governing a particle interaction or decay to improve the measurements of the process [40]. Each constraint that is used reflects some physical condition that the process must satisfy. The constraints are used to slightly change the measured values within their uncertainties, which is usually implemented through a least-squares minimizing procedure.

For example, one can use the fact that the tracks coming from some decay process must originate from a common position. This can then in turn be used to improve the 4-momenta and positions of the daughter particles.

Another example of such a constraint is a mass constraint. In this case one requires that the invariant mass of the mother particle of a decay process equals a known, fixed value.

The kinematic fitting procedure also provides the error information, in the form of a covariance matrix, as well as the correlations of the updated parameters. Usually the constraint will reduce the errors of the original measurement.

The principle of kinematic fitting will be used in section 6.1 of this thesis, where so-called 'S candidates' were fitted using the kinematic fitting package available as a tool in the CMS reconstruction software [37].

Chapter 3

Tools used for simulation of signal, collisions and material interactions

3.1 The Tsallis distribution

In order to cover a wide spectrum of application and use-cases, a rich variety of distributions are in existence. In high energy physics in particular, power law distributions are being applied routinely to describe the distributions of transverse momenta of secondary particles produced during proton-proton collisions. With modern collider energies reaching up to 13TeV, transverse momenta of hundreds of GeV are not uncommon.

The so-called Tsallis distribution is being used extensively in high-energy physics to describe the transverse momentum distributions of such secondary particles during a proton-proton collision [16, 17]. Demanding the distribution to be thermodynamically consistent gives rise to a distribution that can be used as a description of identified particles with the same values of the temperature T and the parameter q. The distribution was originally proposed by C. Tsallis about twenty-five years ago.

A Tsallis-like distribution gives excellent fits to the transverse momentum distributions for the CMS, ALICE, etc... collaborations at the LHC.

The following expression gives the Tsallis transverse momentum spectrum where y is the rapidity ($y = 0$ being mid-rapidity), p_T the transverse momentum and m_T the transverse mass. A more general expression also includes a parameter for the chemical potential μ, which has been set to zero here.

$$\left.\frac{d^2N}{dp_T dy}\right|_{y=0} = gV\frac{p_T m_T}{(2\pi)^2}\left[1+(q-1)\,\frac{m_T}{T}\right]^{-q/(q-1)} \tag{3.1}$$

There are two free parameters, q and T, that characterize the behavior and distribution of a particular type of particle. Typical values for q and T are experimentally obtained through fitting data to eq.3.1. The parameter q is for transverse momentum spectra always close to 1, with typical values of 1.1 or 1.2 [16, 17]. In the limit where the parameter q approaches 1, the distribution approaches the standard Boltzmann distribution. Values for T are typically around 0.04GeV to 0.09GeV. These parameters slightly vary depending on the value for $\sqrt{s}$.

The values that will be used in this work are $q = 1.15$ and $T = 0.08$GeV, which are the values as measured in the CMS experiment at $\sqrt{s} = 7$TeV [17].

Equation 3.1 is commonly used to fit the LHC transverse momenta spectra. The distribution has, among others, been used to fit data for a number of known particles. These include K^0_s, Λ and Ξ for the CMS collaboration in pp collisions at 900GeV. As an illustration the $\pi^{\pm}$, K^+ and p Tsallis distributions measured at ALICE are shown in figure 3.1.

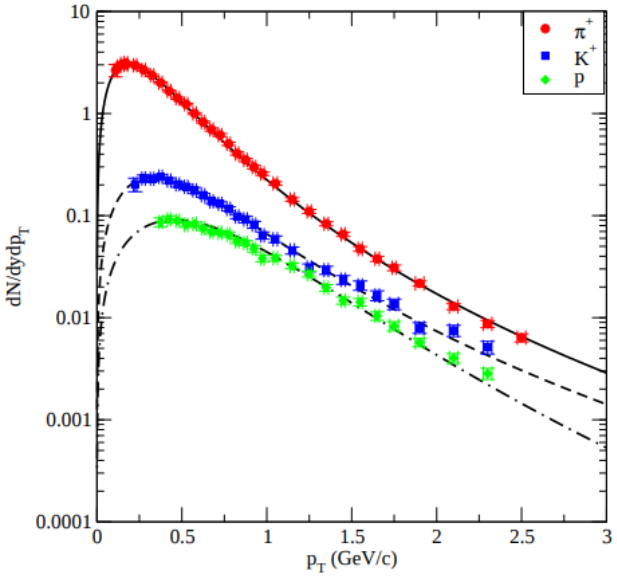

Figure 3.1: This shows a fit to the transverse momentum distributions in a pp collision measured in the ALICE experiment for $\pi^{\pm}$, $K^{+}$and p. Source: [16]

3.2 Monte Carlo methods

Monte Carlo methods or experiments are a range of computational algorithms that are based on repeatedly applying random sampling in order to produce numerical results. The essence of the method is using randomness to solve problems, even though those problems might in principle be deterministic. Monte Carlo methods are often used in physics and mathematics and are exceedingly useful for problems of stochastic nature or in case other approaches fail or are difficult to implement.

In physics-related problems, Monte Carlo methods are widely used for simulating systems comprising of large amounts of coupled degrees of freedom. Other use cases include the evaluation of multidimensional definite integrals with complicated boundary conditions. Any problem with a probabilistic interpretation can, in principle, be solved using Monte Carlo methods.

In the case of many body particle physics systems, such as the simulations of the pp collisions at LHC, techniques referred to as Quantum Monte Carlo methods are used. Pythia is one example of a tool that uses these techniques, and is the tool used for this work.

3.2.1 Pythia

High-energy physics collisions between elementary particles often result in very complex final states, comprised of large multiplicities of hadrons, leptons, photons, neutrinos, etc. The problem is that there is no simple relation between these initial and complex final states and the underlying physics description.

On one hand we do not yet posses a complete understanding of the physics. On the other hand, any attempt at an analytical solution to the whole system is hopeless due the large final state multiplicities and the fact that perturbation theory is not applicable at low energy scales in QCD. Pythia [23, 24] is a tool for the generation of high-energy physics collision events, i.e. for the generation of collisions at high energies between elementary particles such as electrons and protons in multiple combinations. The tool solves these problems through the use of Monte Carlo methods for generating complete events. The complexity is made manageable by means of subdividing the full problem into a set of simpler separate sub routines. Since the underlying physics is not always understood sufficiently to give an exact description the program uses a combination of analytical results and various QCD-based models. Pythia contains theory and models for simulation of hard-process selection, hard and soft interactions, parton distributions, multiparton interactions, initial- and final-state radiation and parton showers, beam remnants,

string fragmentation, particle decays, etc. The emphasis lies on those events where strong interactions play a role, directly or indirectly, and therefore multihadronic final states are produced. The end result of these simulated events can be compared to experimentally observable ones, and used for example for comparisons with existing data, or to study physics at future experiments.

The physics aspects it contains as well as the extensive tuning on data makes it an attractive option especially for LHC physics studies, such as this thesis, in which it was heavily relied upon.

3.2.2 Geant4 toolkit

This thesis partially relies on the use of the Geant4 simulation toolkit.

Geant4 is a toolkit or platform used for the simulation of the passage of particles through matter using Monte Carlo methods. The toolkits' main areas of use are high energy, nuclear and accelerator physics [20, 21, 22]. The software is used by a number of research projects around the world. GEANT was originally developed by CERN and is since then being maintained by the international Geant4 Collaboration.

The toolkit includes routines for handling e.g. geometry, particle transport, detector response and visualization.

The physics processes available for use in simulations include electromagnetic and hadronic processes, a large set of long-lived particles, materials and elements. All of this is possible over a wide energy range starting from the keV range all the way to the TeV range.

The geometry subroutines take care accounting for the physical layout of the experiment, including detectors, material which may cause absorption or scattering, etc. The system simulates how such a material distribution will affect the path of particles in the experiment.

Next, the detector response is taken into account. In this step the passage of a particle through the volume of a detector is recorded and an approximation to how a real detector would respond is simulated. In the case of this thesis, this detector would be the CMS central tracker as discussed in section 2.3.1.

3.3 Samples

Table 3.1 summarizes the four samples that were used to produce all results in this work. Chapter 5 where an investigation into K_s^0 and Λ^0 $\left(\bar{\Lambda}^0\right)$ rates and reconstruction efficiencies is conducted makes use of a minimum bias Monte Carlo sample containing 10 million events. This sample is referred to in this work as the 'Minbias MC' sample. This sample has zero pileup, is not triggered by any hard events (hence minimum bias) and is generated at $\sqrt{s} = 13$TeV. The minbias MC sample was produced using the Pythia8 and Geant4 tools discussed in the previous sections.

This sample contains what in this thesis will be referred to as 'generated' particles (or gen particles), and 'reconstructed' particles (or reco particles), an explanation of which follows in the next section.

Three other samples are used in chapter 6, where an investigation into the backgrounds as well as the definition of cuts is discussed. These samples include two data samples and one Monte Carlo sample. Unless Minbias MC sample, these three samples do contain pile-up.

The Zero Bias data sample contains 30 million events and has no bias towards any hard, triggering event. The Single Muon data sample contains 150 millions events and contains events that were triggered by the presence of at least one hard muon. The W jets Monte Carlo sample contains 24 million events and contains simulated events as if triggered by the presence of at least one W jet. All samples are either generated or collected at $\sqrt{s} = 13$TeV.

Name	Data or MC	PU	hard event trigger	N events
Minbias MC	MC	no	no	10M
Zero bias Data	Data	yes	no	30M
Wjets MC	MC	yes	yes (W+jets)	24M
Single Muon Data	Data	yes	yes (single muon present)	150M

Table 3.1: The four samples that were used in this work.

3.4 Nomenclature

Generated and reconstructed tracks The the rest of this thesis will make use of the following naming conventions, acronym, nomenclature, etc.

Generator level particles, generated particles, or in short 'gen' particles are a data structure containing a particle's pdgid (particle data group identification number), mass, energy, momentum, charge, production vertex location, etc... Generator level particles are produced by the Pythia Monte Carlo tool and are passed through the Geant4 toolkit in order to simulate the material interactions and detector responses of the CMS detector.

A generated track is the trajectory of a generated particle.

Reconstructed particles, or short 'reco' particles, are data structures that contain the energy and momentum of tracks reconstructed by a certain track reconstruction algorithm. This track reconstruction algorithm can either be used to reconstruct a set of generator level particles, or actual data from the CMS trackers. Reconstructed particles do not contain information about their production or decay vertex position.

A simulated track is the trajectory of a simulated particle.

Different kinds of vertices in collider experiments A *primary vertex* (PV) is a position in 3D space where a proton-proton collision has taken place, either in simulation or in real data. One event can contain multiple primary vertices in case of nonzero pile-up conditions. The primary vertex associated with the most energetic collision is referred to as the 'zeroth' primary vertex ($PV\,(0)$), as it is often ordered as the first element in an ordered list of primary vertices.

A *creation vertex* (CV), also known as a production vertex, is a position in 3D space where a generated particles originates. This can be because it's mother particle has decayed to said particle at that location, or because QCD processes formed said particle at that point in space. This is not referred to as production vertex in order to avoid confusion with the primary vertex, which is already referred to as PV.

A *decay vertex* (DV) is the position where a particle decays or interact with material and seizes existing. The decay vertex of a mother particle coincides with the production vertex of its daughter particle.

The primary vertex, creation vertex and decay vertex are all accompanied by their covariance matrices, which contain the uncertainties on their positions.

The *beamspot* (bs or BS) is the luminous region produced by the collisions of proton beams. The beamspot location calculated by a weighted sum The algorithm used to calculated the transverse beam position is the so called $d_0 - \phi$ algorithm. This is a robust and fast χ^2 fit which takes about 1000 good tracks to reach micrometer levels of precision [31]. The beamspot location can, because of this precision, be considered exact for our intents and purposes.

Particle names Because of limitation in the software used to produce plots, in the title of many plots K_s^0 is referred to as 'Ks', Λ^0 is referred to as 'L0', and $\bar{\Lambda}^0$ is referred to as 'antiL0'.

Distances Distances between the primary, creation and production vertex, as well as the beamspot location are in titles of plots written in the following manner: d_{xyz} (Position1_Position2). For example, the distance in the xy-plane between the beamspot and the particle's decay vertex is written as: d_{xy} (CV_bs).

Chapter 4

Strategies for discovering a stable S

4.1 Conservation laws and calorimeters

Now that we know that the S, if it exists, would be stable at collider time-scales (and even much longer than that), this opens up the possibility for probing it at the LHC.

The basic, particle-accelerator-based strategy to find a stable S would be to look for the unique baryon number $B = \pm 2$ and strangeness $S = \mp 2$ quantum numbers of the S and $\bar{S}$. Those quantum numbers being conserved, means that looking for the S could be done by looking for a deficiency in these two quantum numbers. In practice using conservation laws associated with quantum numbers is not possible in colliders such as the LHC because of the loss of too many particles in the process.

Prompt production of an S would mean production through nucleon-nucleon interactions (protons), which as discussed before can be guesstimated to have a production rate of 10^{-4} to 10^{-6} relative to the pion (or more general just hadron) production rate.

We expect the S to be produced during soft proton-proton interactions and hence have a relatively low momentum, lying in the GeV range. This energy range is below what is traditionally studied at the LHC. The spectrum of transverse momenta of the S can be described using the Tsallis p_T distribution, the details of which are discussed in section 3.1.

Since the S is assumed to be essentially stable, and definitely stable on collider timescales, one can not rely on decay products originating from decay of the S itself. The S is electrically neutral, so tracking is not an option, and neither is using electromagnetic calorimeters. Since S is baryonic a hadronic calorimeter might be an option. However, as discussed before, the signature of the S in a hadronic calorimeter would be too similar to the one of a soft neutron, making it impossible to distinguish the two. On top of that, the S could be mistaken for one of the many soft hadrons present in an average interaction, whose energies barely surpass the noise levels of the order of hundreds of MeVs. In conclusion, hadronic calorimeters do not provide a viable strategy.

4.2 Material interactions

The approach used in this work is to look for the signs of an $\bar{S}$, promptly produced during the proton-proton collision at LHC, interacting with the material layers of the CMS detector. Instead of being able to rely on direct detection of the S or its (non-existent) decay products, we rely on the nuclear interaction in the tracking layers, and the reconstruction of the reaction products.

The interaction rate would in this case be proportional to the material density profile everywhere in the detector. This will later be discussed in more detail, using Monte Carlo simulation to investigate these material interactions and relating that to the CMS detector material density profile.

Simple interaction processes being more likely, this work considers the following interaction with their associated reaction products:

$$\bar{S}(\bar{u}\bar{u}\bar{d}\bar{d}\bar{s}\bar{s}) + neutron(udd) \rightarrow K^0(d\bar{s}) + \bar{\Lambda}^0(\bar{u}\bar{d}\bar{s}) \tag{4.1}$$

Alternatively, the following process could also be considered, but will not be the focus of this thesis:

$$\bar{S}(\bar{u}\bar{u}\bar{d}\bar{d}\bar{s}\bar{s}) + neutron(udd) \rightarrow \pi^- (\bar{u}d) + \bar{\Xi}^- \left(\bar{d}\bar{s}\bar{s}\right) \tag{4.2}$$

These processes are schematically laid out in respectively figure 4.1b and 4.1a.

The $\bar{S}$ is produced promptly at the proton-proton interaction primary vertex, flies off and is then intercepted by a neutron in the material layers of the detector.

The first material layer which the $\bar{S}$ passes is the beampipe, which lies at a distance of approximately 2cm from the center of the detector. The $\bar{S}$ is assumed to interact with one of the nucleons (in this case a neutron is considered) in the detector material. This interaction gives rise to, among other less experimentally favorable possibilities, the two interaction processes described in equations 4.1 and 4.2. The focus in this thesis will lie on the process described in the first one.

We only concern ourselves with the $\bar{S}$ and not with the S for the reason that the anti-quarks in the $\bar{S}$ will give rise to the annihilation with the quarks in the neutrons. Since the detector material does not contain anti-neutrons, the S will not give rise to these kinematics.

The $K^0(d\bar{s})$ mixes and can manifest itself as a $K_s^0 \left(\frac{d\bar{s}+s\bar{d}}{\sqrt{2}}\right)$ or a $K_L^0 \left(\frac{d\bar{s}-s\bar{d}}{\sqrt{2}}\right)$, however only the use of K_s^0 is experimentally viable, as the average K_L^0 decay distance lies well outside of the range of the detector (see table 4.1) while the K_s^0 decay length, being 2.7cm, is inside of the central tracker's range.

The main process of interest to this thesis is therefore the following one:

$$\boxed{\bar{S}(\bar{u}\bar{u}\bar{d}\bar{d}\bar{s}\bar{s}) + neutron(udd) \rightarrow K_s^0(d\bar{s}) + \bar{\Lambda}^0(\bar{u}\bar{d}\bar{s})} \tag{4.3}$$

After an average distance of 2.7cm the K_s^0 commonly decays according to the following channels [15]:

- $K_s^0 \rightarrow \pi^+ + \pi^-$ with branching ratio $(69.20 \pm 0.05)\%$
- $K_s^0 \rightarrow \pi^0 + \pi^0$ with branching ratio $(30.69 \pm 0.05)\%$

Since our purpose is detection of these final decay products by means of the CMS experiment, which strongly favors charged particles over electrically neutral particles, our focus lies on the first decay channel.

The second channel results in π^0 particles which then promptly decay to $\gamma\gamma$ at an approximately 100% branching ratio. These could in principle be detected in the ECAL, which has a moderate resolution, but the presence of large backgrounds and the fact that one cannot associate a vertex in this case makes this approach unfeasible.

After on average a distance of 7.9cm the $\bar{\Lambda}^0$ goes on to decay to $p^-\pi^+$ with a branching ratio of $(63.9 \pm 0.5)\%$

particle	mass (MeV)	decay length $c \cdot \tau$ (cm)
$\Xi^{\pm}$	1321.71 ± 0.07	≈ 4.9
Λ^0	1115.683 ± 0.006	≈ 7.9
K_s^0	497.611 ± 0.013	≈ 2.7
K_L^0	497.611 ± 0.013	≈ 153
$\pi^{\pm}$	139.57061 ± 0.00024	≈ 780.5
$p^{\pm}$	938.272081 ± 0.000006	/
n	939.565413 ± 0.000006	~ 1.5 Earth-sun distances

Table 4.1: The particles of interest to us and their relevant properties. The mass of the K_L^0 and K_s^0 are given as that of the K^0. However, it is known that a difference between the masses of the K_L^0 and K_s^0 on the order of $3.5 \cdot 10^{-12}$MeV exists [14]. Source: [15]

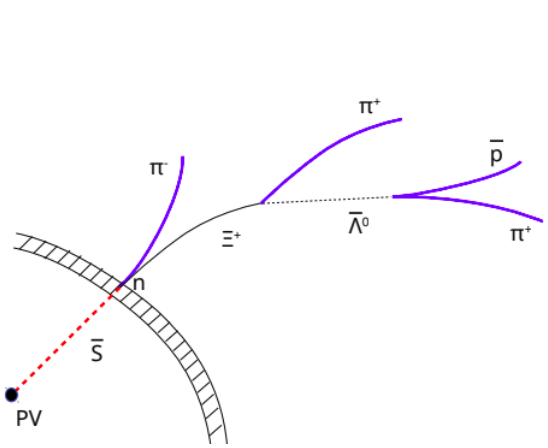

(a) This figure depicts the following process: $\bar{S}(\bar{u}\bar{u}\bar{d}\bar{d}\bar{s}\bar{s}) + neutron(udd) \rightarrow \pi^- (\bar{u}d) + \Xi^- (\bar{d}\bar{s}\bar{s})$. After an average distance of 4.9cm the Ξ^+ then goes on to decay to $\pi^+\bar{\Lambda}^0$ with a branching ratio of (99.887±0.035)%, after which the $\bar{\Lambda}^0$ decays after an average distance of 7.9cm further to $p^-\pi^+$ with a branching ratio of (63.9 ± 0.5)%.

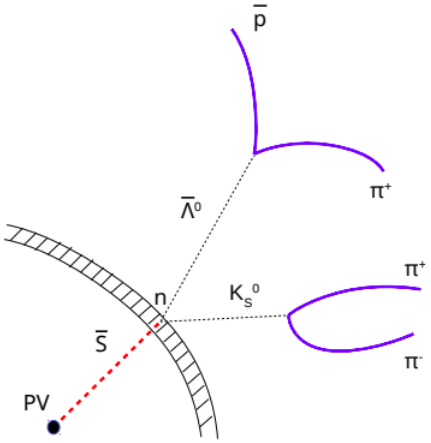

(b) This figure depicts the following process: $\bar{S}(\bar{u}\bar{u}\bar{d}\bar{d}\bar{s}\bar{s}) + neutron(udd) \rightarrow K_s^0(d\bar{s}) + \bar{\Lambda}^0(\bar{u}\bar{d}\bar{s})$. After on average a distance of 7.9cm the $\bar{\Lambda}^0$ then goes on to decay to $p^-\pi^+$ with a branching ratio of (63.9 ± 0.5)%, while after an average distance of 2.7cm the K_s^0 decays into a $\pi^+\pi^-$ pair with a branching ratio of (69.20 ± 0.05)%.

Figure 4.1: These are experimentally the best detection signatures. An $\bar{S}$ is produced promptly during the pp collision and traverses through approximately 2cm of vacuum before hitting the first layer of detector material, namely the beampipe. The $\bar{S}$ is assumed to interact with one of the nucleons (in this case a neutron) in the detector material, giving rise to (among other, less experimentally favorable possibilities) the two interaction processes described in eq. 4.2 and eq. 4.3. [2]

Chapter 5

Generator study of Λ^0 and K_s^0 background

The basic goal of this work is to study the prospects at the LHC of standard modal dark matter in the form of Sexaquarks with CMS data. More precisely, this involves acquiring a better understanding of the Λ^0, $\bar{\Lambda}^0$ and K_s^0 involved in the process described in equation 4.1. This thesis will discuss the estimation of their rates in function of displacement, as well as their transverse momentum and pseudorapidity distributions in simulation and in data. All rate estimates will be split up into three categories, corresponding with K_s^0 and $\Lambda^0\left(\bar{\Lambda}^0\right)$ being produced either promptly at the pp collision, through the decay of a baryon or meson, or through interactions with detector material. The intent is to garner some insight into the Standard Model backgrounds in simulation and in CMS data. No individual background processes in particular are discussed, instead all backgrounds are estimated in one go.

Reconstruction efficiencies of the K_s^0 and $\Lambda^0\left(\bar{\Lambda}^0\right)$ will be presented as a function of displacement, transverse momentum and pseudorapidity.

In the chapter following this one some first crude background-discriminating cuts will be defined and discussed, after which, for the first time with real data, the cuts will be applied to the $\bar{S}$ mass distribution. A demonstration will be given of the feasibility of a search of a low-mass signal in CMS pileup collisions.

The reconstruction efficiencies will, in the last part of this work, serve a purpose in determining a limit on the production cross section of the $\bar{S}$ during the pp collisions.

In the following two sections the set-up of the Monte Carlo investigation into the Λ^0 and K_s^0 particles will be laid out.

5.1 Sample and sample reducing cuts

In order to study the backgrounds of the $S+n \rightarrow \Lambda^0 + K_s^0$ process, it is very informative to make use of one or more Monte Carlo simulation samples. As mentioned in section 3.3, a minimum bias Monte Carlo sample containing 10 million events is used. This sample is free from pile-up and was simulated at $\sqrt{s} = 13\text{TeV}$.

Most of these 10 million events do not contain a K_s^0 and Λ^0 pair, which are precisely the events of interest to this study. In order to reduce the 10 million events to a more manageable amount a skimmer module was run over this sample, applying the following set of cuts.

The cuts applied by the skimmer were chosen to obtain tracks with $p_T > 500\text{MeV}$ within the tracker acceptance. Only events with the following cuts were kept: the presence of at least one Λ^0 or $\bar{\Lambda}^0$ with $p_T > 1.5\text{GeV}$ and at least one gen K_s^0 with $p_T > 0.9\text{GeV}$, with on top of that the requirement for the presence of at least one Λ^0 or $\bar{\Lambda}^0$ with $|\eta| < 2.5$ and at least one K_s^0 with $|\eta| < 2.5$. Those cuts result in there being only 17124 events left post-skimmer.

The pseudo-rapidity cuts are justified because tracking efficiencies greatly drop of outside of the cut-off range for real data tracks, meaning that it is not useful to consider MC generated $\Lambda^0\left(\bar{\Lambda}^0\right)$ or K_s^0 outside of said range. Lastly, only $\Lambda^0\left(\bar{\Lambda}^0\right)$ that decay to $p^{\pm}\pi^{\mp}$ pairs and K_s^0 that decay to $\pi^{\pm}\pi^{\mp}$ pairs are considered.

5.2 Categories

In order to get a better understanding of the K_s^0 and $\Lambda^0\left(\bar{\Lambda}^0\right)$ backgrounds, all K_s^0 and $\Lambda^0\left(\bar{\Lambda}^0\right)$ were subdivided into three different categories. The goal is to separate K_s^0 and $\Lambda^0\left(\bar{\Lambda}^0\right)$ produced either promptly produced during the pp collision (category 1), produced during material interaction (category 2), or produced through the displaced decay of a baryon or meson (category 3).

The splitting up into the three categories is based on the lifetime and type of mother particle of the K_s^0 and $\Lambda^0\left(\bar{\Lambda}^0\right)$.

Table 5.1 summarizes the mother particles by which the three categories are defined. The first column indicates the category, the second column indicates the names of the mother particles of the generator level K_s^0 and $\Lambda^0\left(\bar{\Lambda}^0\right)$. In the case that the mother particle is the K_s^0 or $\Lambda^0\left(\bar{\Lambda}^0\right)$ itself once again, the grandmother is considered instead.

The third column gives the Particle Data Group ID (pdgid) for these mother particles [15]. The pdgid is negative for antiparticles and positive for particles. Here particles and antiparticles are not distinguished between, and therefore only the absolute value of the pdgid is given.

The fourth column shows the percentage of the total number of all K_s^0 or $\Lambda^0\left(\bar{\Lambda}^0\right)$ mother particles (of which there are 284016 considered in this MC sample) that those particular mother particles represent. In addition to having a mother particle that belongs to the ones given under category 1 (c1), the distance between the PV and the decay vertex of this mother particle (motherDV) has to be less than 10cm in order for this K_s^0 or $\Lambda^0\left(\bar{\Lambda}^0\right)$ daughter to be considered of category 1. Using the nomenclature defined in section 3.4, this can be expressed as: $d_{xyz}\left(PV\_motherDV\right) < 10\text{cm}$. If this is not the case (the mother particle is one given in row 2 to 13 of table 5.1 and $d_{xyz}\left(PV\_motherDV\right) > 10\text{cm}$) then the daughter K_s^0 or $\Lambda^0\left(\bar{\Lambda}^0\right)$ gets classified as being produced in material interactions (category 2) instead.

For example, 0.23% of all possible mother particles of K_s^0 and $\Lambda^0\left(\bar{\Lambda}^0\right)$ are Σ^0 baryons. Given that those Σ^0 baryons decay (either spontaneously or because it interacts with material) within a distance of 10cm to either K_s^0 or $\Lambda^0\left(\bar{\Lambda}^0\right)$, those decay products (the K_s^0 or $\Lambda^0\left(\bar{\Lambda}^0\right)$) will be assigned to category 1 and considered to have been produced promptly during the pp collision. If this happens outside of the 10cm range from the PV, then those K_s^0 or $\Lambda^0\left(\bar{\Lambda}^0\right)$ are classified as category 2 and considered to have been produced during material interactions.

Table 5.2 gives a summary of what the fractions of the $\Lambda^0\left(\bar{\Lambda}^0\right)$ and K_s^0 are for each category. This is for a total of 17124 events in the Minimum Bias MC sample, post-skimmer. The table provides average numbers per events. Absolute quantities can be obtained by multiplying the provided averages by the total number of events, namely 17124.

Furthermore, the average number of reconstructed Λ^0or $\bar{\Lambda}^0$ per event is 0.086 and the average number of reconstructed K_s^0 per event is 0.3.

To summarize again:

- c1: K_s^0 or Λ^0 promptly produced during the pp collision
- c2: K_s^0 or Λ^0 produced during material interaction
- c3: K_s^0 or Λ^0 produced through displaced decay of baryon or meson
- c123: all three put together (no cut on category)

Category	mother particle (particle and/or anti particle)	pdgid	% of total	approx. mean lifetime (s)	family
c1	Σ^0	3212	0.23	10^{-21}	Strange baryon
	K^0	311	68.7		Strange meson
	$\Phi\,(1020)$	333	2.06	10^{-22}	Light I=0 meson
	$f_0\,(1710)$, $f_0\,(980)$	10331, 9010221	≈ 0	10^{-23}	Light I=0 meson
(given that $dxyz<$ 10cm, else classified as c2)	u,d,s,c,b quarks and gluons	1, 2, 3, 4, 5, 21	10.8	0	Quarks and gluons
	$J/\Psi\,(1S)$, $\chi_{c2}\,(1P)$, $\chi_{c1}\,(1P)$, $\eta_c\,(2S)$	443, 445, 20443, 100441	≈ 0	10^{-21}	$c\bar{c}$ mesons
	$(dd)_1, (ud)_0, (ud)_1$, $(uu)_1, (sd)_0, (sd)_1$, $(su)_0, (su)_1, (ss)_1$, $(cd)_1$	1103, 2101, 2103, 2203, 3101, 3103, 3102, 3203, 3303, 4103	0.09	0	Diquark string states
	$\Sigma^{\star -}$	3114	2.09	10^{-10}	Strange baryon
	Σ^0	2312	10.2	10^{-20}	Strange baryon
	$\Sigma^{\star 0}$	3214	2.21	10^{-20}	Strange baryon
	$\Sigma^{\star +}$	3224	2.24	10^{-10}	Strange baryon
	Λ_c^+	4122	0.05	10^{-13}	Charmed baryon
	Ξ_c^0, Ξ_c^+	4132, 4232	0.01	10^{-13}	Charmed baryon
c2	K_L^0	130	0.01	10^{-8}	Strange meson
	K_s^0	310	≈ 0	10^{-10}	Strange meson
	K^+	321	0.01	10^{-8}	Strange meson
	π^+	211	0.54	10^{-8}	Light I=1 meson
	n^0	2112	≈ 0		Light baryon
	p^+	2212	0.24		Light baryon
c3	Σ^-, Σ^+, Ξ^-, Ξ^0	3112, 3222, 3312, 3322	≈ 0	10^{-10}	Strange baryon
	D^0	421	0.16	10^{-13}	Charmed meson
	B^0, B^+, B_S^0	511, 521, 531	≈ 0	10^{-12}	Bottom meson
	Λ_b^0, Ξ_b^0	5122, 5232	≈ 0	10^{-12}	Bottom baryon

Table 5.1: A summary of all the particles by which the three categories (c1, c2 and c3) are defined. The first column indicates the category, the second column indicates the names of the (grand)mother particles of the generator level K_s^0 and $\Lambda^0\,(\bar{\Lambda}^0)$. In the case that the mother particle is the K_s^0 or $\Lambda^0\,(\bar{\Lambda}^0)$ itself once again, the grandmother is considered instead. The third column gives (the absolute value of) the Particle Data Group ID (pdgid) for these mother particles [15]. The fourth column shows the percentage of the total number of all K_s^0 or $\Lambda^0\,(\bar{\Lambda}^0)$ mother particles (of which there are 284016 considered in this MC sample) that those particular mother particles represent. In addition to having a mother particle that belongs to the ones given under category 1 (c1), the distance between the PV and the decay vertex of this other particle (or equivalently the creation vertex of the daughter K_s^0 or $\Lambda^0\,(\bar{\Lambda}^0)$) has to be less than 10cm in order for this K_s^0 or $\Lambda^0\,(\bar{\Lambda}^0)$ daughter to be considered of category 1. Otherwise the daughter K_s^0 or $\Lambda^0\,(\bar{\Lambda}^0)$ gets classified under category 2 (produced in material interactions) instead.

Average number of ...		gen Λ^0 or Λ^0	gen K_s^0
in total		4.70	11.9
that decay to the proper daughters		2.44	7.10
that are of category	c1	4.59	11.7
	c2	0.111	0.123
	c3	0.00164	0.0273
that decay to the proper daughters and are of category	c1	2.42	7.05
	c2	0.0160	0.0365
	c3	0.000642	0.0175

Table 5.2: This table shows the average number of gen Λ^0 or $\bar{\Lambda}^0$ and gen K_s^0 that either: decay to the proper daughters but don't necessarily belong to any of the categories; belong to one of the given categories but don't necessarily decay to the proper daughters; and then both at the same time. Here 'proper daughters' mean a $p^{\pm}\pi^{\mp}$ pair in the case of the Λ^0 or $\bar{\Lambda}^0$ and a $\pi^{\pm}\pi^{\mp}$ in the case of a K_s^0. This is for 17124 events. Absolute quantities can be obtained by multiplying the provided averages by this number of events.

5.3 Transverse momentum and pseudorapidity distributions

Figure 5.1 shows the pseudorapidity (η) and transversal momentum (p_T) distributions of the generator level K_s^0. The distributions are, as discussed in the previous section, split up into categories 1, 2 and 3, indicating the way in which the K_s^0 was produced. Respectively these represent: prompt production at the primary vertex (c1), production through material interactions of its mother particle (c2), or through decay of a baryonic or mesonic mother (c3). The promptly produced K_s^0 outweigh the other two categories by two orders of magnitude.

Figure 5.1a shows a smooth η distribution for the promptly produced K_s^0, peaking at 0, gradually dropping off towards higher $|\eta|$.

The K_s^0 produced by material interactions have an η distribution that peaks at around $|\eta| = 2$, then drops off steeply with increasing $|\eta|$ and cuts of around $|\eta| = 5$. Towards $\eta = 0$, the contribution of material interactions in producing K_s^0 is very small. This is because the presence of mechanical structures such as cables and cooling are all minimized there, to make space for the tracker.

The η distribution for the decay-produced K_s^0 peaks at $\eta = 0$, where it dominates over the material interaction produced K_s^0.

Figure 5.1b shows the transversal momentum of promptly (c1) produced K_s^0 peaking at $p_T \approx 0.25$GeV, then gradually falling for increasing p_T and forming a long tail reaching up until a p_T of multiple GeV. The small 'hiccup' at 0.9GeV is the result of the $\exists K_s^0 : p_T > 0.9$GeV cut in the Skimmer as discussed in section 5.1, causing there to be less K_s^0 in the bins below 0.9GeV.

The K_s^0 produced in material interactions (c2) show a p_T distribution which dominates over the K_s^0 produced in baryon/meson decay (c3) up until the 1GeV level. Whereas the material interaction category cuts off around $1.5-2$GeV, the decays category shows a longer tail reaching up to 4.5GeV.

Decays have harder p_T distribution because they came from heavier hadrons where interactions may be induced by low-mass, low-p_T particles. On top of that they can produce several particles which the available energy needs to be distributed over.

In the case of generator level Λ^0 $(\bar{\Lambda}^0)$ we see a very similar picture for both the p_T and η distributions, but with much less statistics present in the third category due to the probability of Λ^0 $(\bar{\Lambda}^0)$ originating form meson or baryon decay being considerably smaller than the same thing being the case for a K_s^0.

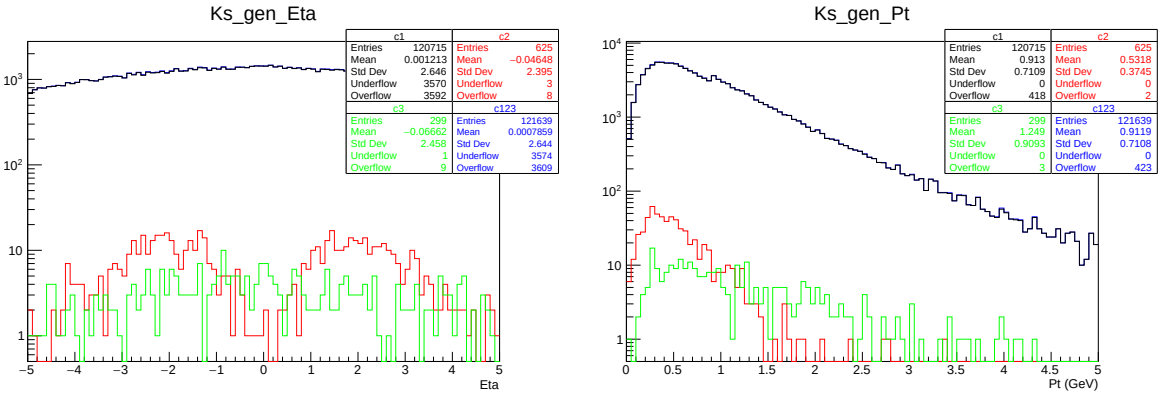

(a) (b)

Figure 5.1: The η and p_T distributions of the K_s^0. These histograms are split up into the three categories. These represent the ways in which the K_s^0 was produced, namely through prompt production at the pp collision (c1), through material interactions of its mother particle (c2), or through decay of a baryon or meson mother (c3).

5.4 Creation vertex scatter plots

In order to get a better understanding of the creation vertex positional distribution and its relation to the geometry of the detector's material, 2D position scatter plots are discussed next. Figures 5.2a and 5.2b respectively show the $\left(dz, dr = \sqrt{dx^2 + dy^2}\right)$ and the (dx, dy) scatter plots of the K_s^0 for all three categories (c1, c2 and c3) combined. Here dx, dy and dz means the x, y and z distance (as in the CMS coordinate system) between the K_s^0 creation vertex (also called production vertex) and the event's primary vertex (of which there is only one present, as this is a sample without pile-up).

Figure 5.2a has two main distinctive features: the concentrated 'blob' near the origin and the rest of the entries, which tend to be grouped together into horizontal lines. The blob, which has width of about 0.7cm (3 standard deviations) and has a thickness of about 3mm (3 standard deviations), indicates the creation vertex positions of the K_s^0 produced promptly (category 1) and produced due to fast baryon or meson decays (category 3), respectively being responsible for 99.2% and 0.25% out of the 121639 entries. The remaining 0.5% of the entries end up spread out over the scatter plot, forming the horizontal bands, and originate from particles which are produced at the origin and interact with the detector material.

The position of these interactions correlate to the presence of material, which is dominated by mechanical structures and services such as cooling, power and readout electronics, rather than actual detection layers.

The material distribution and structure of the CMS inner tracker has been studied using nuclear interactions caused by hadrons striking the material. For this, data from proton-proton collisions at $\sqrt{s} = 13$TeV was used to reconstruct large amounts of secondary vertices from hadronic interactions with the detector material. The positions of the inner tracking system elements, such as the beam pipe, the barrel pixel detector inner shield, pixel detector support tube, and barrel pixel detector support rails become clearly visible by using sufficient amounts of these vertices.

Precise mapping of material within the tracker is important since the material affects the reconstruction and analysis of events through multiple scattering, energy loss, electron bremsstrahlung, photon conversions, and nuclear interactions.

The resulting scatter plot is visible in figure 5.3. Comparing to figure 5.2b allows one to identify the effects of the beampipe, as well as the pixel support tube and the BPIX detector support rails on the K_s^0 production vertex distribution. More detailed structures are difficult to make out due to a lack of statistics.

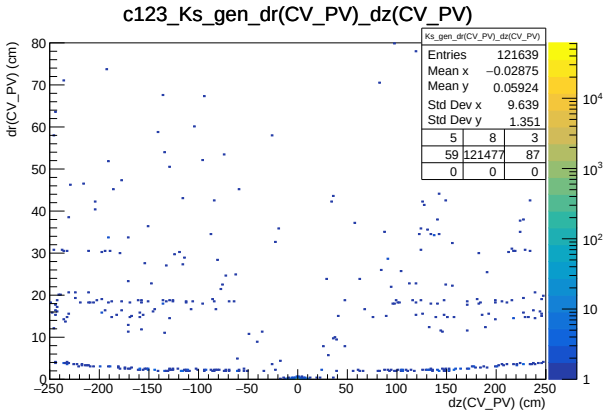

(a) The $\left(dz, dr = \sqrt{dx^2 + dy^2}\right)$ scatter plot of the K_s^0 for all three categories combined. Here dx, dy and dz indicates the x, y and z distance between the K_s^0 creation vertex and the event's primary vertex. The color indicates the density of points. The 'blob' at the origin is caused by K_s^0 produced promptly (c1) and through baryon or meson decay (c3). The Λ^0 scatter plots show a very similar picture as the ones discussed here for the K_s^0, although with less statistics.

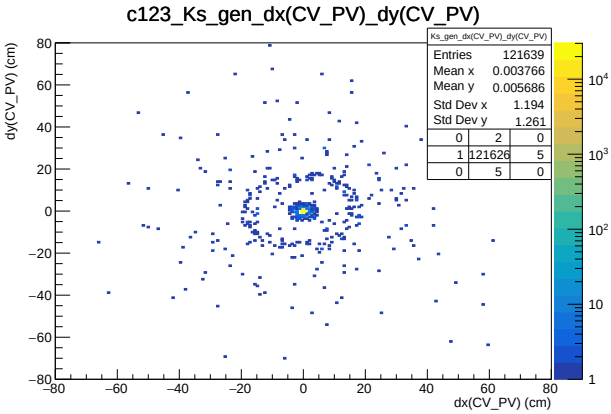

(b) The(dx, dy) scatter plot of the K_s^0 for all three categories combined. Here dx and dy indicate the x and y distance between the K_s^0 creation vertex and the event's primary vertex. The color indicates the density of points. The yellow, central pixel inside of the blue 'blob' at the origin is caused by K_s^0 produced promptly (c1) and through baryon or meson decay (c3). The Λ^0 scatter plots show a very similar picture as the ones discussed here for the K_s^0, although with less statistics.

Figure 5.2

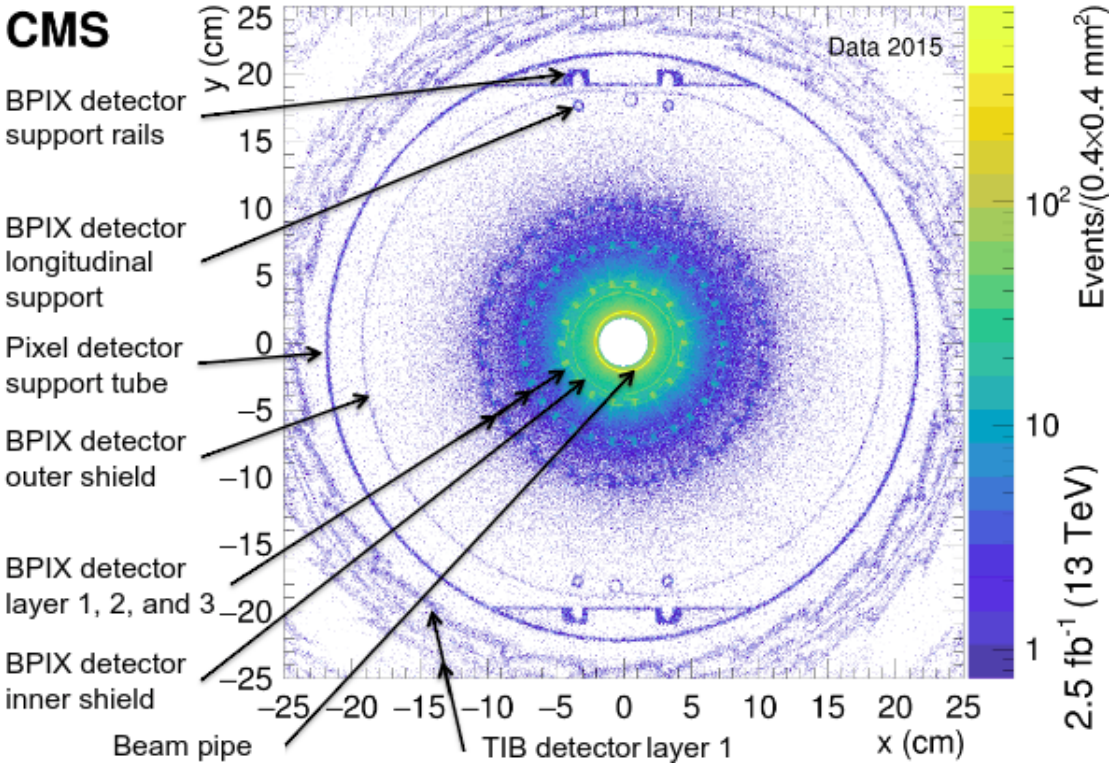

Figure 5.3: The density of nuclear interaction vertices in the barrel region of the tracker detector, shown in the xy-plane. The signatures of the beam pipe, the BPIX detector with its support rails, and the first layer of the TIB detector are clearly visible above the background of misreconstructed nuclear interaction vertices. [29]

5.5 Vertex position distances

Figures 5.5a and 5.5b show the 3D distance and the distance in the xy plane between the primary vertex (PV) of the event and this time the decay vertex (DV) of the generator level K_s^0.

The K_s^0 produced promptly at the PV (category 1) shows, as expected, a smoothly falling distribution. This distribution might be shaped by the selection cuts.

It was verified that the K_s^0 that are produced through the fast decay of mesons or baryons (c3) are produced as good as promptly. Figure 5.5a shows that the bulk of these K_s^0 then decay within 50cm (or 20cm in the xy-plane in fig. 5.5b) from the PV. The category 3 K_s^0 distribution shows the exponentially falling profile, starting at the PV as expected. The distribution does have a long tail continuing to distances of several meters. The same is true in the case of Λ^0 or $\bar{\Lambda}^0$.

The K_s^0 produced in material interactions (c2 in fig.5.5a) shows a smeared out, not exponentially falling distribution. This is due to these K_s^0 of category 2 being produced over a longer distance, namely wherever there is detector material, as opposed to solely at the PV in the case of the K_s^0 of category 1 and 3.

We notice, as in figures 5.2a and 5.2b, the forward production of this category of K_s^0, as well as hints of the enhancement of K_s^0 production through interactions at certain radii.

Figures 5.4a and 5.4b show the 3D distance and the distance in the xy plane between the creation or production vertex (CV) and the decay vertex (DV), both taken from the generator level K_s^0.

All three categories show an exponentially falling distribution as measured in the xy-plane, as is to be expected.

Figure 5.5c shows the distance in the z direction between the primary vertex (PV) of the event and the decay vertex (DV) of the generator level K_s^0. Once again, category 1 (prompt production) shows nothing remarkable. Category 2 (material interactions) shows a smeared out profile of the K_s^0 for the same reason as discussed before. Category 3 (decays) shows an exponentially falling distribution since these K_s^0 are produced near the PV.

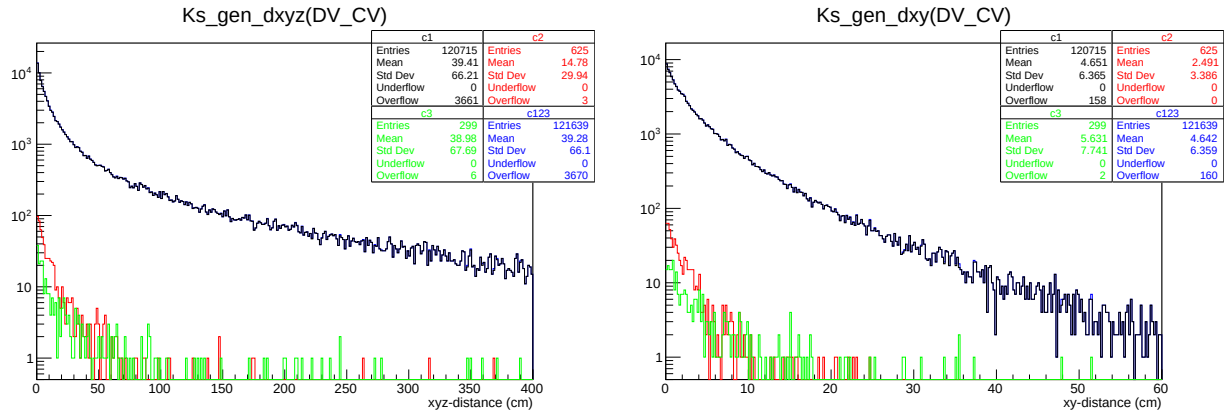

(a) (b)

Figure 5.4: The 3D (xyz) and the 2D (xy-plane) distances between the creation (or production) vertex (CV) position of the K_s^0 and the decay vertex (DV) position of the K_s^0. Category 1 indicates promptly produced K_s^0, category 2 indicates K_s^0 produced through material interactions and category 3 indicates K_s^0 produced through baryon or meson decay. All three categories put together is indicated by 'c123'.

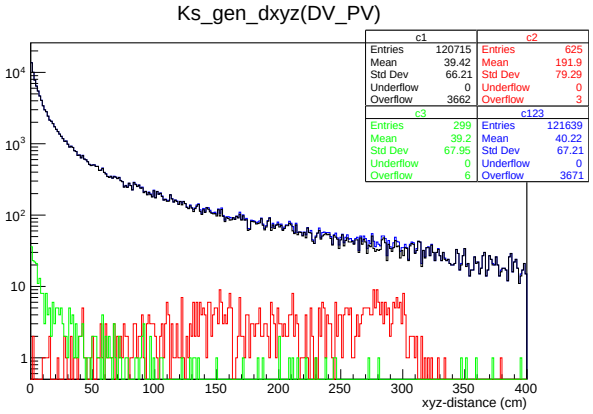

(a)

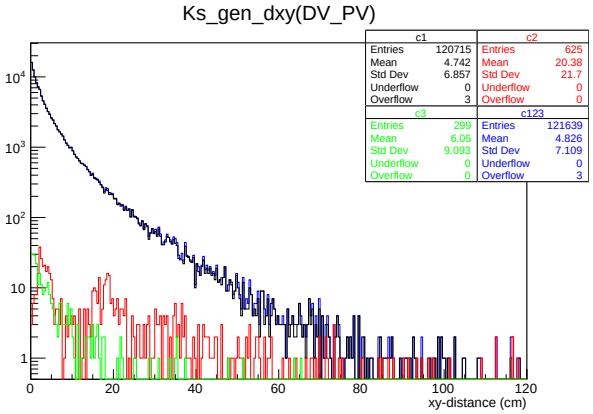

(b)

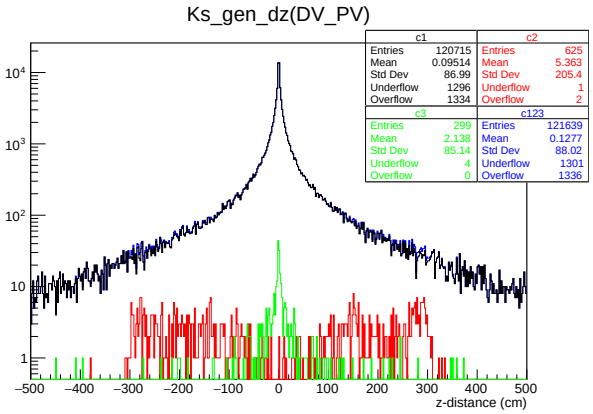

(c)

The 3D (xyz), 2D (xy-plane) and z-coordinate (along the beamline) distances between the primary vertex (PV) of the event and the decay vertex (DV) position of the K_s^0. Category 1 indicates promptly produced K_s^0, category 2 indicates K_s^0 produced through material interactions and category 3 indicates K_s^0 produced through baryon or meson decay. All three categories put together is indicated by 'c123'.

Figure 5.5

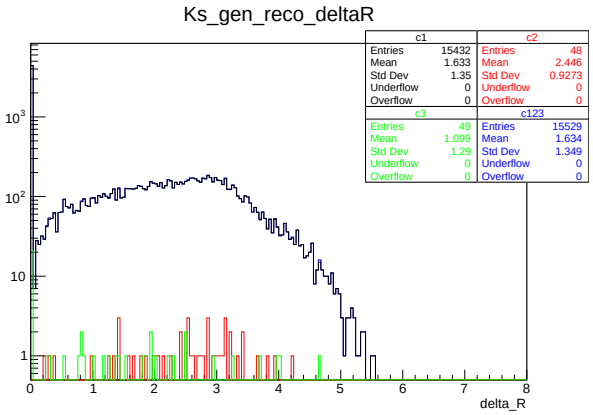

(a)

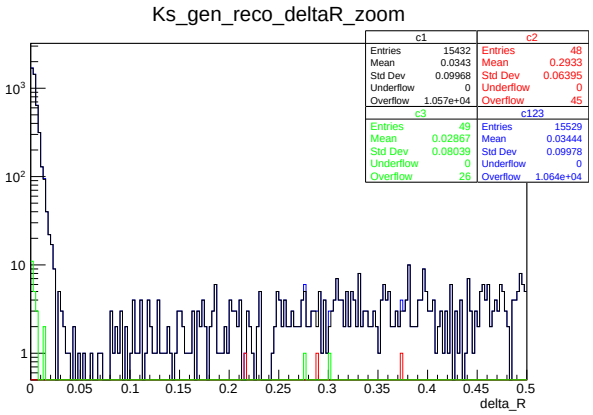

(b)

Figure 5.6: The $\Delta R = \sqrt{(\Delta\phi)^2 + (\Delta\eta)^2}$ distribution between all the generator level K_s^0 and their reconstructed counterparts. This for the usual three categories. The first figure gives a global oversight of the distribution, while the second figure provides a more detailed zoom into the sharp spike near $\Delta R \approx 0$.

5.6 Reconstruction efficiencies

The following chapter of the Monte Carlo studies focuses on reconstruction efficiencies of the K_s^0 and Λ^0 particles, as the understanding of these efficiencies will be essential towards setting limits on the production cross sections of our S candidates, the details of which are discussed in section 7.1. Next to that, the study of the reconstruction efficiencies serves as a sanity check for the K_s^0 and Λ^0 reconstruction algorithms. This can be done by comparing the reconstruction efficiencies of the K_s^0 and Λ^0 to the track reconstruction efficiencies provided by the CMS collaboration. These are provided in [18].

The K_s^0 and Λ^0 4-momenta are reconstructed through a vertex fit of the reconstruction of their decay products. In the case of K_s^0 these decay products are a $\pi^+\pi^-$ pair and in the case of the $\Lambda^0(\bar{\Lambda}^0)$ these are a $p(\bar{p})$ and a $\pi^-(\pi^+)$. Since two tracks (the tracks of both decay products) have to be reconstructed, the reconstruction efficiencies per decay product will have to essentially be squared in order to arrive at the reconstruction efficiencies of the mother particle, namely the K_s^0 or $\Lambda^0/\bar{\Lambda}^0$ and one can not directly compare the K_s^0 and $\Lambda^0\left(\bar{\Lambda}^0\right)$ reconstruction efficiencies with the ones provided by CMS shown in fig.5.7. As an estimate, one can 'square' the value of the reconstruction efficiencies in these plots and compare this result to the efficiencies that will be provided in the following sections.

We consider the generator level K_s^0 and $\Lambda^0\left(\bar{\Lambda}^0\right)$ that comply to the cuts discussed in section 5.1 and their reconstructed counterparts. An additional cut to the generated K_s^0 and $\Lambda^0\left(\bar{\Lambda}^0\right)$ is then applied on top of the already existing cuts. More precisely if a generated K_s^0 or $\Lambda^0\left(\bar{\Lambda}^0\right)$ or one of its daughter pions or protons has $|\eta| > 2.5$, that K_s^0 or $\Lambda^0\left(\bar{\Lambda}^0\right)$ is cut.

For every combination between all these generator level and reconstructed K_s^0 and Λ^0 in a given event, one can calculate $\Delta R = \sqrt{(\Delta\phi)^2 + (\Delta\eta)^2}$. Here $\Delta\phi$ is the azimuthal angle difference between the generated and reconstructed particle directions and $\Delta\eta$ is the difference between their pseudorapidity. The resulting ΔR is a measure for the size of a cone that precisely encapsulates both the reco and gen level tracks. A small value of ΔR indicates a close matching or a good overlap between the spatial direction of both tracks' momenta.

Figure 5.6a shows the ΔR distribution between the generator level K_s^0 and Λ^0 and their reconstructed counterparts. Figure 5.6b, which zooms in on the $\Delta R \in [0; 0.5]$ range, provides a more detailed look into the sharp spike near the origin.

We defined $\Delta R = 0.02$ to be the cut-off for deciding whether or not generator level K_s^0 or Λ^0 lie within a small enough cone from a reconstructed K_s^0 or Λ^0 to be considered a match. In other words, if $\Delta R < 0.02$ then the reconstructed K_s^0 or Λ^0 is assumed to be the reconstructed version of the generator level counterpart.

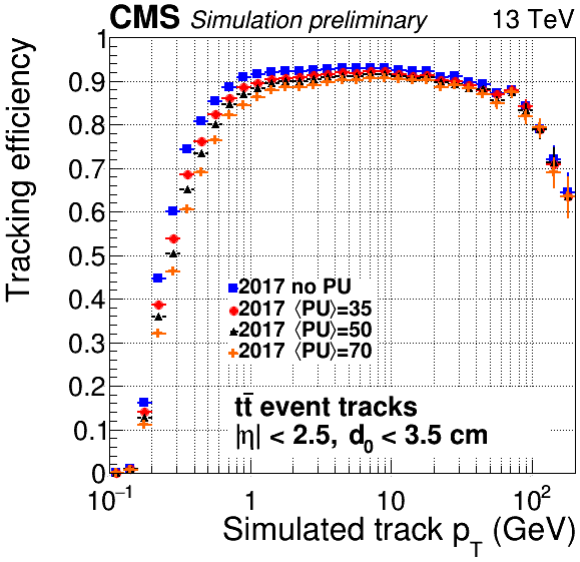

(a) Track reconstruction efficiency as a function of simulated track p_T .

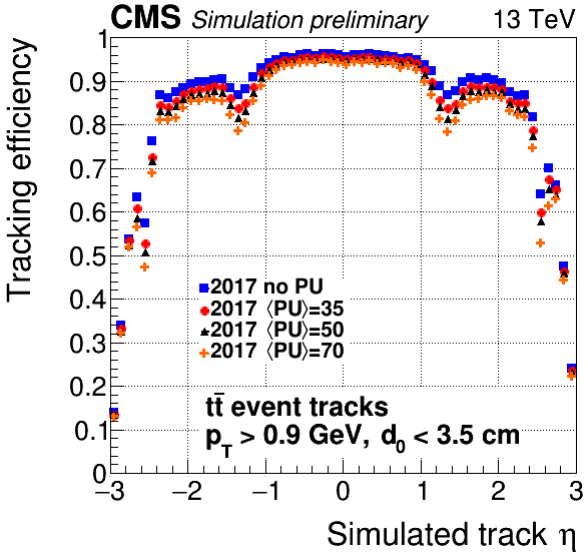

(b) Track reconstruction efficiency as a function of simulated track pseudorapidity.

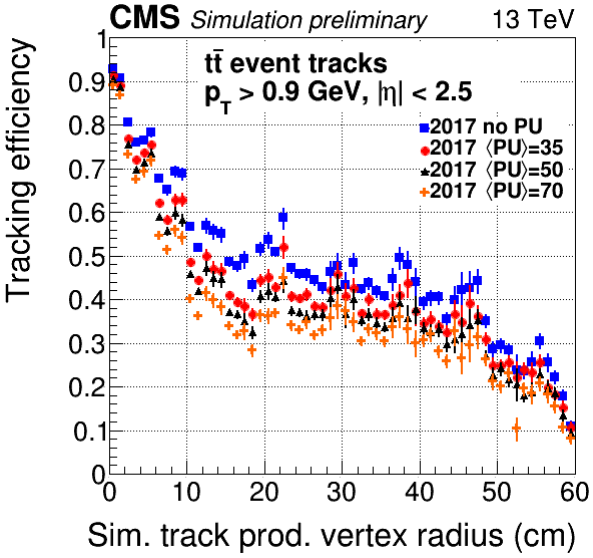

(c) Track reconstruction efficiency as a function of simulated track production vertex radius.

Figure 5.7: The CMS published tracking reconstruction efficiencies relevant to this work. These are the results of 2017. The tracking performance at different PU conditions is shown, namely: $\langle PU \rangle$ =0, 35, 50 and 70. Since the minimum bias Monte Carlo sample used in this work has no pile up, the relevant information is the no PU distributions indicated by the blue squares. The used samples are $t\bar{t}$ events simulated at $\sqrt{s} = 13$TeV. A simulated track is the track of a particle from the Geant4 detector simulation. A reconstructed track is the result of the track reconstruction run on the simulated data. The efficiency is defined as the number of matched reconstructed tracks divided by number of simulated tracks. The requirement for there being a match between a reconstructed track and a simulated is that the simulated track has at least 75% of its hits in common with the simulated track. Source: [18]

5.6.1 Reco efficiencies in function of transverse momentum

First we discuss the comparison between the official CMS reconstruction efficiencies in function of transverse momentum p_T, given in figure 5.7a, and the MC simulation reconstruction efficiencies for the reconstruction of a K_s^0 and a Λ^0 out of the generator level K_s^0 and Λ^0. This is for the Minimum Bias MC sample. Our focus lies on the low-p_T region. Figure 5.10 shows the p_T distributions of the reconstructed K_s^0 and Λ^0.

Figures 5.8a and 5.8b show the reconstruction efficiencies for K_s^0 and Λ^0 in function of the p_T of the generator level K_s^0 and Λ^0. Comparing to fig.5.7a (and keeping in mind that the efficiencies in fig.5.7a are to be squared in order to make them comparable to the ones in figures 5.8a and 5.8b) one can see similar behavior, albeit with some small shift along the p_T axis. Figures 5.8a and 5.8b show that the reconstruction efficiency (ϵ) is practically zero below values of $p_T = 1$GeV and starts increasing in value towards approximately $\epsilon \approx 0.5$ near $p_T = 2$GeV. Figure 5.7a however shows ϵ, while also starting at zero for $p_T \approx 0$GeV, picking up faster in value, and flattening out around $\epsilon \approx 0.9$ near $p_T \approx 1$GeV. The p_T behavior of Λ^0 $\left(\bar{\Lambda}^0\right)$ and K_s^0 is slightly different because the $\Lambda^0 \to p\pi^-$ decay involves a much more massive proton which takes on average a larger part of the Λ^0 momentum, leaving the one pion with a lower p_T [41]. This is not the case for the $K_s^0 \to \pi^\pm\pi^\mp$ where both pions take on average an equal portion of the p_T. For this reason, the Λ^0 needs a higher p_T to reach the same level of reconstruction efficiency as the K_s^0, as this efficiency is dominated by the lowest p_T of the daughter particles.

The CMS reconstruction efficiency plots were produced using $t\bar{t}$ events with displacements of below $d_0 < 3.5$cm, while the decay vertex of the K_s^0 and Λ^0 (i.e. the production vertices of the child $\pi^\pm$ or $p^\pm$ which are the ones that are actually reconstructed) tend to have a higher displacement of up to 80cm (see figure 5.5b), explaining the reduction in reconstruction efficiency compared to the official CMS ones. We come back to this in section 5.6.3.

Figures 5.9a and 5.9b show the reconstruction efficiencies for K_s^0 and Λ^0 in function of the minimum p_T of either one of the two daughters of the generator level K_s^0 and Λ^0. These daughters are the $\pi^\pm\pi^\mp$ pairs in the case of K_s^0 and the $\pi^\pm p^\mp$ in case of a Λ^0 or $\bar{\Lambda}^0$. Since it is these daughter particles that are actually being reconstructed and their 4-momenta being summed to arrive at the K_s^0 or Λ^0, the daughter particle with the minimum p_T will be the main inefficiency driver in the reconstruction of the K_s^0 or Λ^0. Therefore this is an interesting distribution to consider. Figures 5.9a and 5.9b show that, up until $p_T \approx 1$GeV, more closely mimics the one of figure 5.7a.

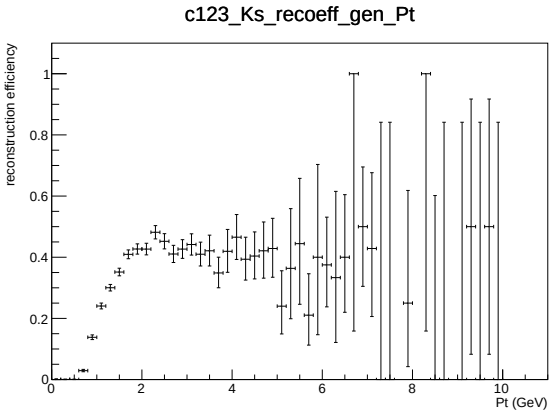

(a) The reconstruction efficiency of the K_s^0 in function of transversal momentum.

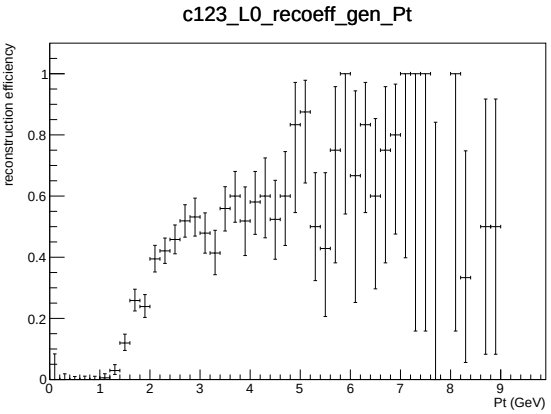

(b) The reconstruction efficiency of the Λ^0 and $\bar{\Lambda}^0$ in function of transversal momentum.

Figure 5.8: The reconstruction efficiencies for K_s^0 and Λ^0 in function of the p_T of the generator level K_s^0 and Λ^0. As obtained from the Minimum bias MC sample.

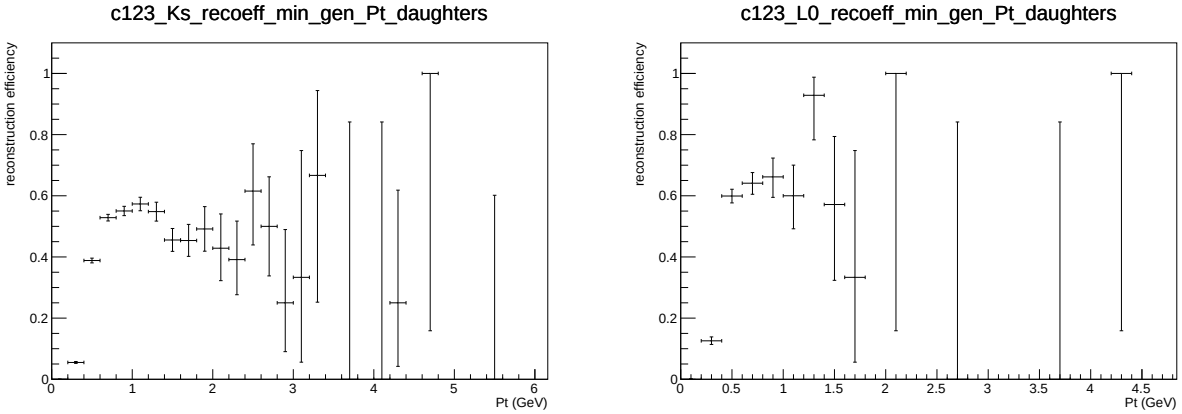

(a) (b)

Figure 5.9: The reconstruction efficiencies for K_s^0 and Λ^0 in function of the minimum p_T of either one of the two daughters of the generator level K_s^0 and Λ^0. These daughters are the $\pi^{\pm}$ pairs in the case of K_s^0 and the $\pi^{\pm}p^{\mp}$ in case of a Λ^0 or $\bar{\Lambda}^0$. This is for the Minimum bias MC sample.

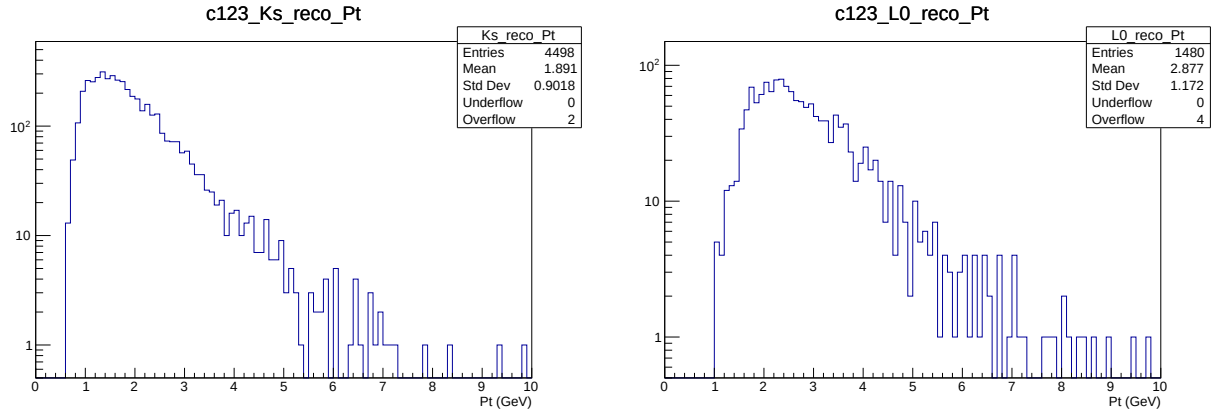

(a) (b)

Figure 5.10: The p_T distribution of reconstructed K_s^0 and Λ^0 (respectively the first and second sub-figure) in the Minimum Bias MC sample.

5.6.2 Reco efficiencies in function of pseudorapidity

Here a comparison is made between the official CMS reconstruction efficiencies in function of pseudorapidity η, given in figure 5.7b, and the MC simulation reconstruction efficiencies for the reconstruction of a K_s^0 and a Λ^0 out of the generator level K_s^0 and a Λ^0. Figure 5.12 shows the η distributions of the reconstructed K_s^0 and Λ^0. This is for the Minimum bias MC sample and does not discriminate between any of the three previously discussed categories.

Figure 5.11a shows an efficiency distribution which is flat inside the $|\eta| < 1$ range, which then experiences a dip around $|\eta| \approx 1.4$, recovers near $|\eta| \approx 2$ and then cuts off approaching $|\eta| \approx 2.5$. This is very comparable to the distribution shown in figure 5.7b, which indicates that reconstruction of the K_s^0 and Λ^0(or more precisely their daughters) is well behaved. The distribution for Λ^0 in figure 5.11b gives a less clear distribution due to the lack of statistics compared to the K_s^0 case.

The dips near $|\eta| \approx 1.4$ seem to coincide with the increase in the production of Λ^0 and K_s^0 due to material interaction (category 2) in figure 5.1a. As the K_s^0 decays to $\pi^{\pm}\pi^{\mp}$ or the Λ^0 $\left(\bar{\Lambda}^0\right)$ decays to $p^{\pm}\pi^{\mp}$ in a region where the material is dense (and where therefore the chance for a K_s^0

or Λ^0 to be produced during a material interaction increases), one of these decay products might get lost due to a material interaction, making reconstruction of this decay product, and therefore the original K_s^0 or Λ^0 $\left(\bar{\Lambda}^0\right)$ impossible, consequently suppressing the reconstruction efficiency. The correlation between the increase in material interaction produced K_s^0 or Λ^0 $\left(\bar{\Lambda}^0\right)$ and the dips in reconstruction efficiency isn't perfect, but it is nevertheless interesting to indicate the existence of this link.

The value of the efficiency at $\eta = 0$ for the K_s^0 case is $\epsilon \approx 0.3$. The discrepancy with the CMS tracking results in figure 5.7 can be explained by the fact that most of the to-be-reconstructed $\pi^{\pm}$ and $p^{\pm}$ lie at much larger displacement (see figure 5.5b) than the $d_0 < 3.5$cm which is the case in figure 5.7b.

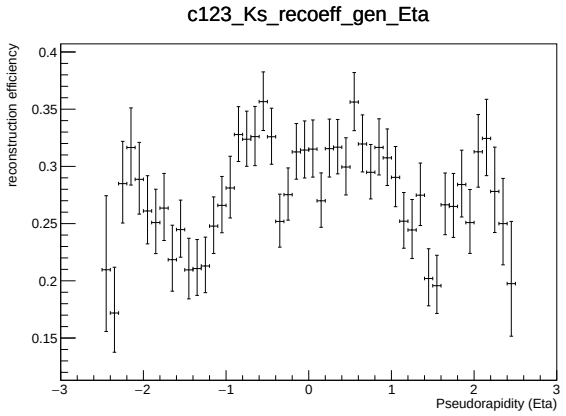

(a) The reconstruction efficiency of the K_s^0 in the minimum bias MC sample.

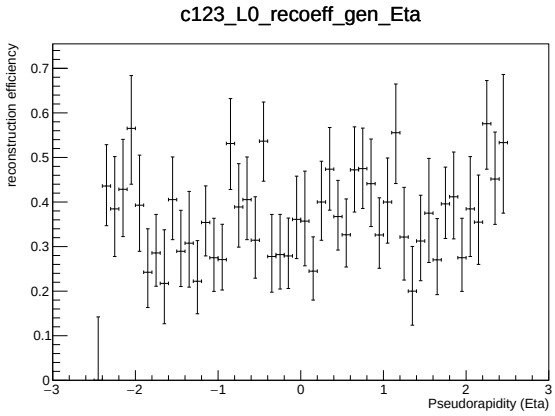

(b) The reconstruction efficiency of the Λ^0 and $\bar{\Lambda}^0$ in the minimum bias MC sample.

Figure 5.11

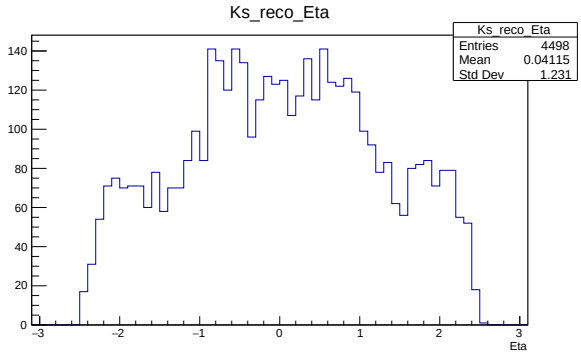

(a)

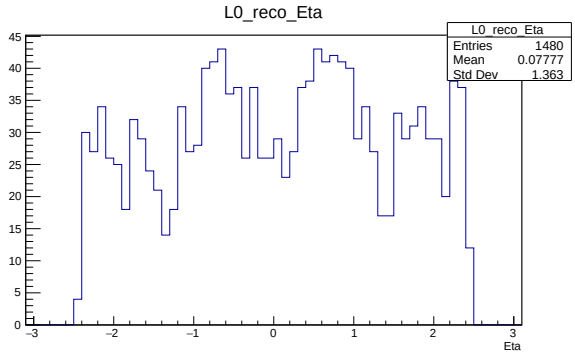

(b)

Figure 5.12: The η distribution of reconstructed K_s^0 and Λ^0 (respectively the first and second sub-figure) in the Minimum Bias MC sample.

5.6.3 Reco efficiencies in function of displacement

It is useful to compare between the CMS reconstruction efficiencies in function of the displacement in the xy-plane between the primary vertex and the reconstructed particle's production vertex and the reconstruction efficiencies of the K_s^0 and Λ^0 in the minimum bias MC sample. This distance is referred to as the production vertex radius in figure 5.7c. More precisely, what ought to be compared with the production vertex radius from figure 5.7c is the production vertex radius from the K_s^0 and Λ^0 children, namely the $\pi^{\pm}$ and $p^{\pm}$, since these particles that are actually being reconstructed by the reconstruction algorithm. Equivalently a comparison can be made between the production vertex radius of figure 5.7c and the decay vertex radius of the K_s^0 and Λ^0. This last distance is indicated by $dxy\,(DV - PV)$ in figure 5.13. Here DV stands for the decay vertex position of the K_s^0 or Λ^0, and PV stands for the primary vertex position. dxy indicates that the distance considered lies in the xy-plane.

Figure 5.7c shows that the efficiency, starting near $\epsilon = 1$ for production vertices that lie near the primary vertex, decreases slowly and substantially with production vertex displacement. A similar picture holds true for reconstruction efficiency distributions of the K_s^0 and Λ^0 respectively shown in figure 5.13a and 5.13b, although these efficiencies start off at a value of $\epsilon \approx 0.3$, which results in a 1-track equivalent efficiency of $\sqrt{0.3} \approx 0.54$, still half of the $\epsilon \approx 1$ in figure 5.7c. This discrepancy can be explained partially due to the fact that lower p_T tracks with small efficiency are still included for the Λ^0 and K_s^0 cases.

All in all, the efficiencies are fairly 'flat' in function of the displacement up to 20cm and even beyond. This is because displacement is displacement. It does not really matter how large it is. As soon a there is any displacement to speak of, the reconstruction efficiency suffers.

Appendix A.1.3 contains the reconstruction efficiencies for the K_s^0 and Λ^0 in the minimum bias MC sample in function of dz, the displacement along the direction of the beamline between the primary vertex and the K_s^0 or Λ^0 $\left(\bar{\Lambda}^0\right)$ decay vertex (and equivalently the production vertex of the decay products).

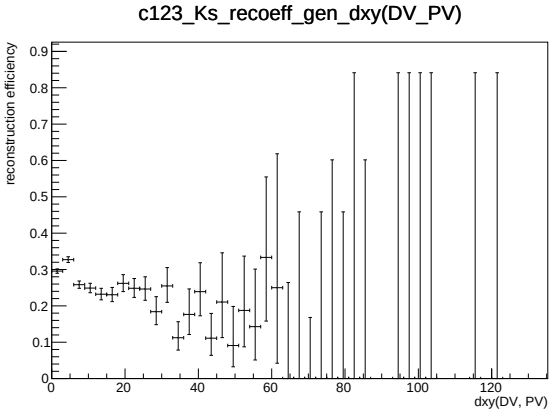

(a) The reconstruction efficiency of K_s^0 in function of the displacement in the xy-plane between the primary vertex (PV) and the decay vertex (DV) of the K_s^0 (or equivalently the production vertex of the $\pi^{\pm}\pi^{\mp}$ pair). The minimum bias MC sample was used to produce these results.

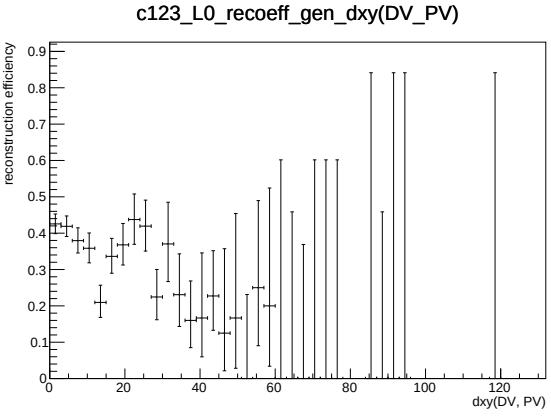

(b) The reconstruction efficiency of Λ^0 $\left(\bar{\Lambda}^0\right)$ in function of the displacement in the xy-plane between the primary vertex (PV) and the decay vertex (DV) of the Λ^0 $\left(\bar{\Lambda}^0\right)$ (or equivalently the production vertex of the $p^{\pm}\pi^{\mp}$ pair). The minimum bias MC sample was used to produce these results

Figure 5.13

Chapter 6

Searching Sexaquarks

In this chapter some first crude background-discriminating cuts will be defined and discussed, after which, for the first time with real data, the cuts will be applied to the $\bar{S}$ mass distribution. A demonstration will be given of the feasibility of a search of a low-mass signal in CMS pileup collisions.

The reconstruction efficiencies will, in the last part of this work, serve a purpose in determining a limit on the production cross section of the $\bar{S}$ during the pp collisions.

In this section the focus will lie on a comparison between the Single Muon data sample, the Zero Bias data sample and the W+jets Monte Carlo sample, the details of which are discussed in section 3.3.

At first we only focus on results containing only Λ^0 and no $\bar{\Lambda}^0$. This is to ensure we stay blind during this part of the analysis, since the $\bar{\Lambda}^0$ are associated with signal while the Λ^0 will only play a role in the background processes. No differences in distribution shapes have been observed between Λ^0 and $\bar{\Lambda}^0$ for all distributions in the next sections. In section 6.6 a small portion of the data is unblinded by considering processes involving $\bar{\Lambda}^0$ and the results of this are discussed. The unblinded data, being 150 million events or about $0.06\text{pb}^{-1}$of integrated luminosity for the Single Muon data sample, represents a mere estimated 4% of the total integrated luminosity of data available for just 2016, which is 1.4pb^{-1}. This percentage drops even lower if data from other years is considered as well, although this number is difficult to estimate due to overlapping of data samples.

The distribution of the number of primary vertices is given in figure A.4 in appendix A.2. The average number of primary vertices is per event is approximately 20 for all three samples.

6.1 The S candidate

Given the pre-reconstructed K_s^0 and $\Lambda^0\left(\bar{\Lambda}^0\right)$, we can now proceed to build S candidates.

The goal of a vertex fit is to obtain the fitted vertex position and its associated covariance matrix, given a set of track estimates and their associated covariance matrices.

The K_s^0 and $\Lambda^0\left(\bar{\Lambda}^0\right)$ were fit together to a single point (vertex) of origin. In the case that this fit is successful, the resulted fitted vertex is labeled as the S candidate, S_{cand} or sCand vertex. These K_s^0 and $\Lambda^0\left(\bar{\Lambda}^0\right)$ were subjected to the same p_T cuts as previously discussed in the Monte Carlo studies part of this work, namely requiring the presence of at least one $p_T < 0.9\text{GeV}$ (for K_s^0) and $p_T < 1.5\text{GeV}$ (for $\Lambda^0\left(\bar{\Lambda}^0\right)$).

Since these K_s^0 and $\Lambda^0\left(\bar{\Lambda}^0\right)$ are neutral particles there are no tracks associated to them, making many popular fitting tools that make use of said tracks unavailable for our purpose. It is their daughter pions and protons that are charged and were used for their pre-reconstruction.

The S candidates were fitted using the kinematic fitting package available as a tool in the CMS reconstruction software [37], the details of which are discussed in section 2.4.3. The $\Lambda^0\left(\bar{\Lambda}^0\right)$ and K_s^0 vertices are refitted applying the respective mass constraints. Next $\Lambda^0\left(\bar{\Lambda}^0\right)$ and K_s^0 are fitted together, propagating their respective covariance matrices.

To be fully correct, the vertex fit of a reconstructed K_s^0 and $\bar{\Lambda}^0$ (and subtracting the 4-momentum of a neutron in rest) should be referred to as an $\bar{S}$ candidate instead of an S candidate.

The distinction will however be dropped in the rest of this work.

The S candidate vertex 4-mometum and mass is obtained in the following manner:

$$S^{\mu}_{cand}\left(E_S, \vec{p}_S\right) + n^{\mu}\left(m_n, \vec{0}\right) = \Lambda^{0,\mu}\left(E_{\Lambda^0}, \vec{p}_{\Lambda^0}\right) + K^{0,\mu}_{s}\left(E_{K^0_s}, \vec{p}_{K^0_s}\right) \tag{6.1}$$

$$\iff S^{\mu}_{cand}\left(E_S, \vec{p}_S\right) = \left(E_{\Lambda^0} + E_{K^0_s} - m_n, \vec{p}_{\Lambda^0} + \vec{p}_{K^0_s} - \vec{0}\right) \tag{6.2}$$

$$\iff m^2_{S_{cand}} = S^{\mu}_{cand} S_{cand,\mu} = \left(E_{\Lambda^0} + E_{K^0_s} - m_n\right)^2 - \left(\vec{p}_{\Lambda^0} + \vec{p}_{K^0_s}\right)^2 \tag{6.3}$$

Here the S candidate interacts with a neutron at rest[1], as described in section 4.2, resulting in the K^0_s and Λ^0 (or $\bar{\Lambda}^0$ is the case of an $\bar{S}$) end products, which then go on to decay as described into the pion and proton final state particles.

The S mass can thus be fully reconstructed.

6.2 Point of Closest Approach distance

Figure 6.1 shows a diagram that visualizes the 2D Point of Closest Approach (PCA) between the S candidates' extrapolated momentum vector ($\vec{p}_{Scand}$) and the beamspot (BS). The S candidate is, as explained previously, the vertex fit between the reconstructed K^0_s and $\Lambda^0\left(\bar{\Lambda}^0\right)$. This diagram lies parallel to the xy-plane and the PCA is calculated in this plane. Although the detector has sufficient precision to also calculate the PCA in the longitudinal z coordinate, this information is not useful in the analysis, because we cannot easily deduce which primary vertex the S candidate originated from.

The distance between the PCA and the beamspot (BS) is indicated by $d_{xy}\left(PCA\_BS\right)$. The distance between the S candidate vertex position and the beamspot is indicated by V_{xy}.

The circle with a radius of approximately 2cm indicates the start of the first material layer, namely the beampipe, and therefore the range of locations where potential S (or more precisely $\bar{S}$) candidates might encounter a nucleon (neutron) with which it could go on to interact, resulting in the K^0_s and $\Lambda^0\left(\bar{\Lambda}^0\right)$. S candidate vertices lying inside the 2cm radius from the beamspot are not the result of such an interaction and are therefore not associated with the possible presence of an $\bar{S}$. Such S candidates are to be disregarded as background to the signal. This fact will be used to motivate the background cuts discussed in section 6.5.

Figure 6.2 shows the distributions for the point of closest approach distances between the beamspot and the S candidate vertex position, calculated in the xy-plane, for a V_{xy} distance larger than 18mm. Only the S candidates (the ones where the K^0_s are fitted together with a Λ^0, not an $\bar{\Lambda}^0$) are taken into account.

Figure 6.3 shows the distribution of V_{xy} for the Single Muon data sample. The distribution for the other two samples look nearly identical. The vast majority of S candidates have a V_{xy} of less than 18mm.

The three sub-figures of figure 6.2 contain the results obtained from three different samples: the Single Muon Data sample, the W-jets MC sample, and the Zero Bias Data sample. The sign of the PCA distance is given by the sign of the scalar product between the vector pointing from the S candidate to the beamspot ($\vec{BS} - \vec{S}_{cand}$) and the S candidate momentum vector ($\vec{p}_{S_{cand}}$), both considered in the xy-plane.

$$sign = sgn(\left(\vec{BS} - \vec{S}_{cand}\right) \cdot \vec{p}_{S_{cand}}) \tag{6.4}$$

This sign is negative in case the angle θ in figure 6.2 is smaller than 90° and the S candidate was produced 'before' the PCA with the beamspot. The sign is positive in case θ is above 90° and the S candidate was produced 'after' the PCA with the beamspot.

All three sub-plots in figure 6.2 show very similarly distributions, sharply spiking at a PCA distance of zero and quickly decaying at distances of a few millimeters, well below the radius of the first detector material layer at approximately 2cm. Most PCAs lie within 1 to 2 millimeters

[1] This is ignoring possible Fermi motion of the nucleons (neutron) inside the material nucleons. This Fermi motion could potentially affect the energy-momentum and thus the mass distribution of the S candidates. Fermi motion has associated momenta up to 250MeV [19]. A proper inclusion of this effect would induce an additional smearing of the S candidate mass distribution.

from the beamspot. All three distributions show symmetry between the positive and negative sign.

A more or less flat, or predictably shaped PCA distance distribution would have been convenient because it could have been used for predicting the behavior of background signals from the beamline, by extrapolating the behavior at some PCA distance away from the beamline. Such a flat distribution could have been caused due to the potential presence of backgrounds caused by random overlaps, since in this case the $\vec{p}_{Scand}$ vector would not correlate with or originate from the beamline. Next to that, nuclear interactions in detector material need not to point back to the beamline, in case one of the produced particles is not reconstructed.

This turns out not to be the case, and motivating background cuts based on this approach is thus not possible.

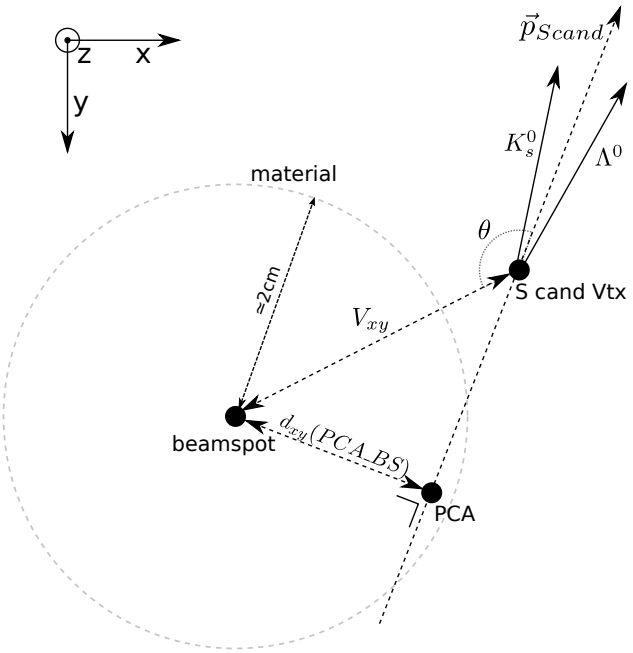

Figure 6.1: Diagram that visualizes the Point of Closest Approach (PCA) between the S candidates' extrapolated momentum vector ($\vec{p}_{Scand}$) and the beamspot (BS). This diagram lies in the xy-plane and the PCA is also calculated in this plane. The distance between the PCA and the BS is indicated by $dxy\,(PCA\_BS)$. The distance between the S candidate vertex position and the BS is indicated by V_{xy}. The circle with radius of approximately 2cm indicates the start of first detector material layer.

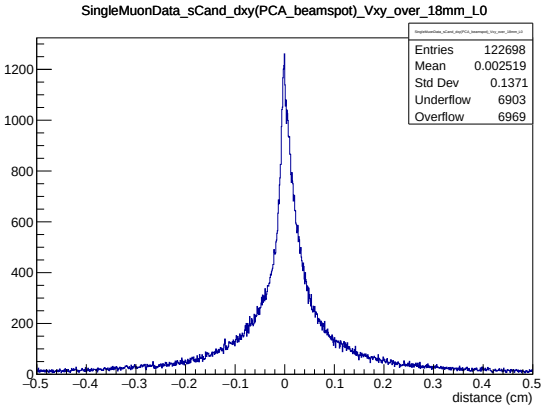

(a) The PCA distribution for the Single Muon Data sample.

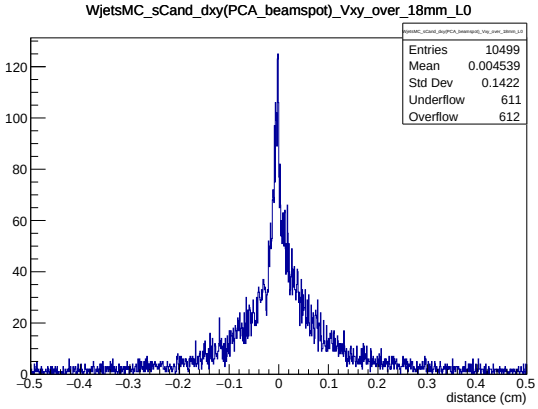

(b) The PCA distribution for the W jets MC sample.

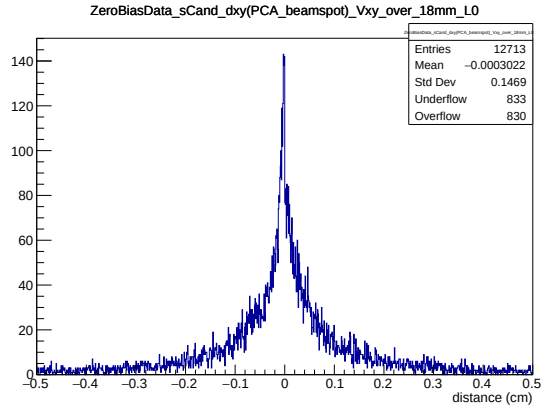

(c) The PCA distribution for the Zero Bias Data sample.

The distributions for the point of closest approach between the beamspot and the S candidate (not $\bar{S}$) vertex position, calculated in the xy-plane, for $V_{xy} > 18$mm. Only the S candidates (the ones where the K_s^0 are fitted together with a Λ^0, not an $\bar{\Lambda}^0$) are taken into account. The three sub-figures contain the results three different samples: the Single Muon Data sample, the W-jets MC sample, and the Zero Bias Data sample. The sign of the PCA distance is given by the sign of the inproduct between the vector pointing from the S candidate to the beamspot (in the xy-plane) and the S candidate momentum vector (in the xy-plane).

Figure 6.2

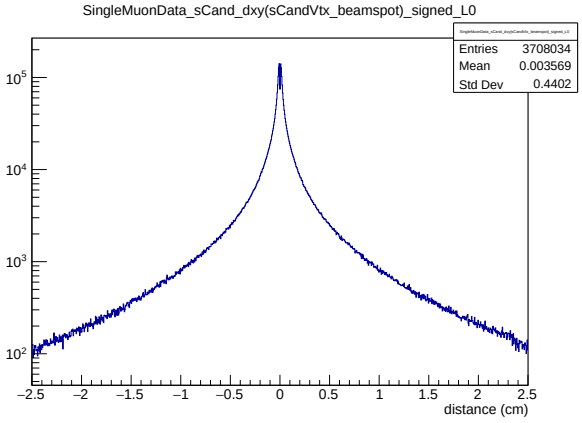

Figure 6.3: The distance between the S candidate vertex and the beamspot, also referred to in this work as V_{xy}. The sign is given by the sign of the scalar product between the vector pointing from the S candidate to the beamspot (in the xy-plane) and the S candidate momentum vector (in the xy-plane). This is the distribution for the Single Muon data sample, the results for the other two samples look very similar.

6.3 Delta Phi - possible jets?

Figure 6.5 shows the distributions of $\Delta\phi$ between the S candidate's K_s^0 and Λ^0 daughters for the Single Muon data sample, the W jets Monte Carlo sample, and the Zero Bias data sample. This is clarified in figure 6.4.

In the case that both $\phi_{K_s^0}$ and ϕ_{Λ^0} are uncorrelated and are uniformly distributed between 0 and 2π, their difference, $\Delta\phi$, would also follow a uniform distribution. The distributions shown in figure 6.5 however clearly differ and indicate that the K_s^0 and Λ^0 of a given S candidate tend to be near to one another in the sense of their azimuthal angles, both in the forward ($\Delta\phi \approx 0$) and backwards direction ($\Delta\phi \approx \pi$). This indicates correlated emission of K_s^0 and Λ^0 particles.

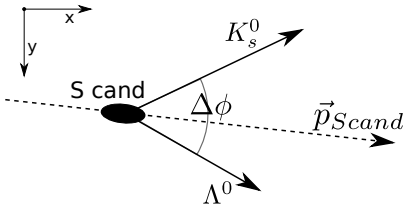

Figure 6.4: Clarification of the way the S candidate $\Delta\phi$ is defined.

One hypothesis is that these K_s^0 and Λ^0 $\left(\bar{\Lambda}^0\right)$ are part of jets, because the correlated emission seems to be present both in the same direction, as well as 'back-to-back'. Such jets are hypothesized to be present due to the fact that the events in the samples are triggered by a hard event, such as the presence of accompanying jets in the Single Muon data sample, or in the W+jets MC sample. The same effect is however also visible in the Zero Bias data sample, in which hard event triggers are expected to be very rare, and hence few hard jets are expected to be present.

The zeroth primary vertex ($PV\,(0)$) is the primary vertex with the highest energy originating from it. A hard, triggering event will tend to originate from this zeroth primary vertex. If the $\Delta\phi$ correlation is linked to the presence of jets in a hard event, we should see a difference between $\Lambda^0 - K_s^0$ pairs coming from the $PV\,(0)$ to pairs not coming from it. It thus is informative to cut out S candidates that originated or that point back towards the $PV\,(0)$. This is done in figure 6.6, which shows the same $\Delta\phi$ distribution, but with an additional cut on the distance in the z direction (the direction along the beamline) between the in 3 dimensions calculated PCA of the extrapolated S candidate momentum to the $PV\,(0)$, and the $PV\,(0)$ itself. Figure 6.6a shows the $\Delta\phi$ distribution between the S candidates' K_s^0 and Λ^0 daughters, given that this distance in the z direction is larger than 1mm, effectively cutting out the $PV\,(0)$. Figure 6.6b does the exact opposite, only plotting the $\Delta\phi$ distribution for S candidates with an extrapolated momentum which lies within 1mm distance in the z-direction of the $PV\,(0)$ at the PCA. This has the effect of exclusively considering the $\Delta\phi$ distribution of S candidates originating from this vertex, and ignoring all others.

Figure 6.6a shows a slight reduction in the back-to-back correlation of emission of K_s^0 and Λ^0 $\left(\bar{\Lambda}^0\right)$ compared to the forwardly emitted ones. In figure 6.6b the reverse happens.

All in all, both figures still show strong correlated emission of K_s^0 and Λ^0 $\left(\bar{\Lambda}^0\right)$, meaning that the jets in a hard, triggering event are part of the explanation, but further more in-depth studies beyond the scope of this thesis are warranted to understand the mechanisms behind this correlated emission of $\Lambda^0 - K_s^0$ pairs.

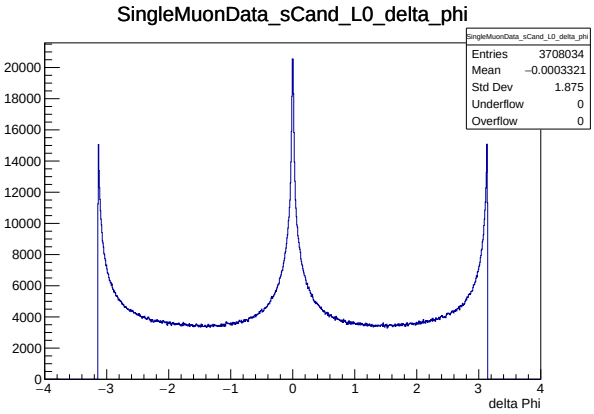

(a)

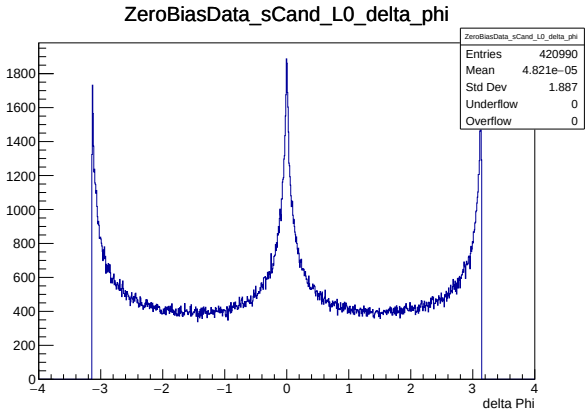

(b)

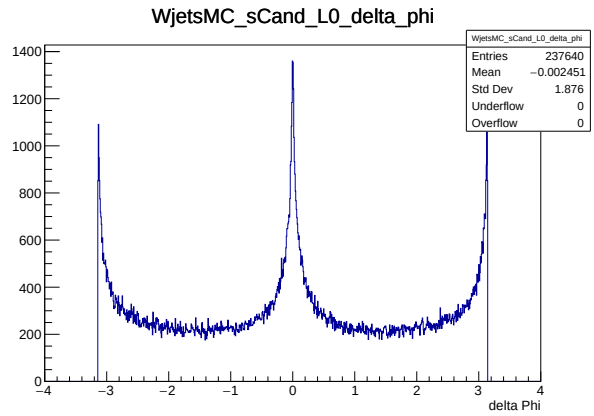

(c)

These figures show the distributions of $\Delta\phi$ between the S candidates daughter K_s^0 and $\Lambda^0\left(\bar{\Lambda}^0\right)$. This is done for the Single Muon data sample, the W jets Monte Carlo sample, and the Zero Bias data sample. The left side of the plots are identified with the right side of the plots.

Figure 6.5

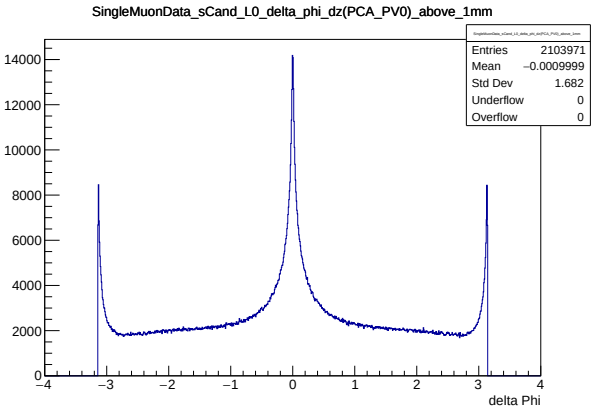

(a)

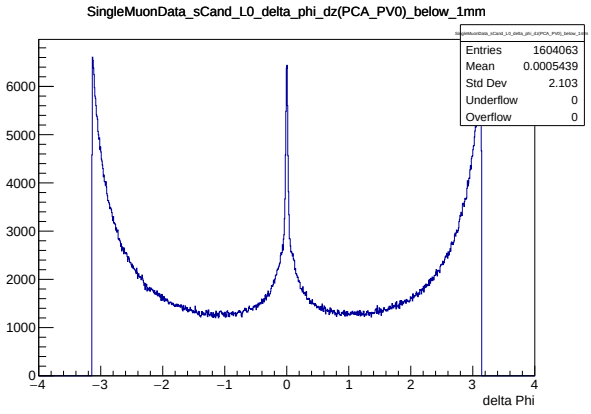

(b)

Figure 6.6: The $\Delta\phi$ distribution between the S candidates' K_s^0 and $\Lambda^0\left(\bar{\Lambda}^0\right)$ daughters given that the extrapolated S candidate momentum lies either within or outside of 1mm,or outside of distance (in the z-direction) of the $PV\left(0\right)$ at the PCA to this $PV\left(0\right)$. This effectively cuts out the $PV\left(0\right)$ or exclusively includes it. This is for the Single Muon data sample. The results for the other two samples look very similar.

Figure 6.8 shows a two dimensional scatter plot with on the x-axis $\Delta\phi$, the azimuthal angle between the S candidates' K_s^0 and Λ^0 daughters, and on the y-axis the distance in the xy-plane between the S candidate vertex and the beamspot location, also referred to as the S candidate's displacement.

Comparing the $\Delta\phi$ distribution to the S candidate's displacement shows long, drawn out 'spikes' at $|\Delta\phi| \approx 0$ and $|\Delta\phi| \approx \pi$. At these $\Delta\phi$, which correspond to the values for the hypothesized jet-like formations, the distributions of possible displacements seems to be extremely spread out, ranging from distances of 0cm up to distances of well above 30cm.

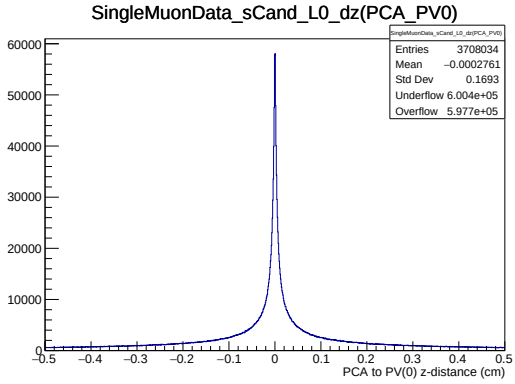

Figure 6.7: The distribution of distances in the z-direction between the $PV\,(0)$ and the PCA of the extrapolated S candidate's momentum to the $PV\,(0)$.

These spikes form due to the presence of very large uncertainties at these values of $\Delta\phi$. This is because the fitting together of two tracks into a vertex gives rise to large uncertainties in the vertex position if those tracks are near-parallel to each other. One has very little information about where the fitted vertex is supposed to lie in this parallel direction. Figure 6.9 illustrates this concept. Small angular separations between the K_s^0 and Λ^0 tracks give rise to a large uncertainty on the position of the S candidate vertex, which in turn translates into a large spread in the distribution of distances to the beamspot.

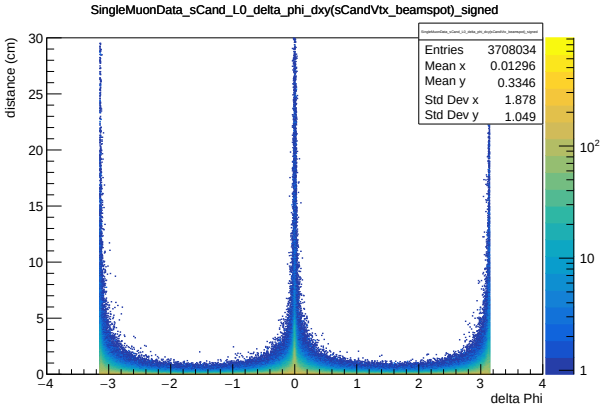

(a)

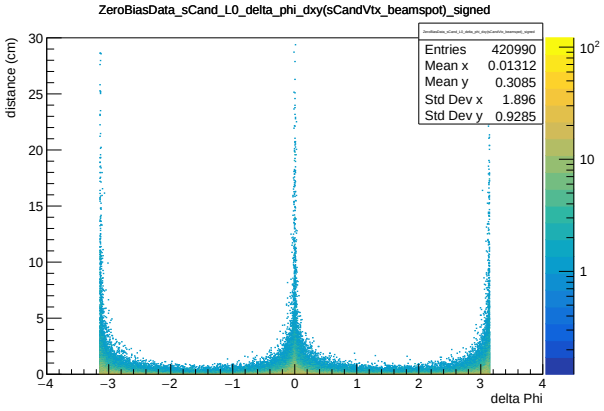

(b)

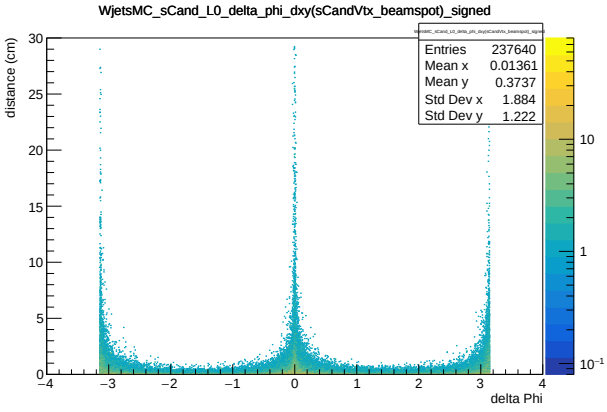

(c)

Two dimensional scatter plots with on the x-axis $\Delta\phi$, the azimuthal angle between the S candidates' K_s^0 and Λ^0 daughters (and not $\bar{\Lambda}^0$, in order to stay blind), and on the y-axis the distance in the xy-plane between the S candidate vertex and the beamspot location. This is shown for all three the data samples.

Figure 6.8

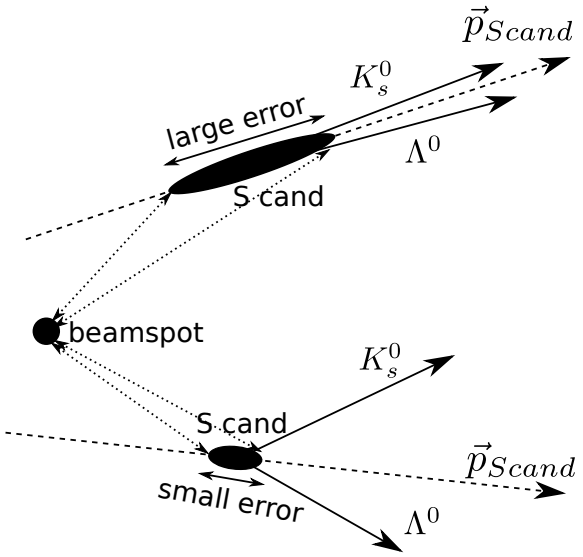

Figure 6.9: This diagram illustrates the effect of near-parallel tracks being fit into a vertex on the positional uncertainty of that vertex, especially in this near-parallel direction to the tracks. More precisely, these uncertainties are characterized by the covariance matrix of the vertex position, depicted by the ellipses in the diagram. Small angular separations between the K_s^0 and Λ^0 tracks give rise to a large uncertainty on the position of the S candidate vertex, which in turn translates into a large spread in the distribution of distances to the beamspot.

6.4 Summary

In summary of the previous sections:

- Due to the absence of a plateau or flattening of the PCA distance distribution, making use of it to predict background $\Lambda^0 - K_s^0$ pairs coming from the beamline by extrapolating from the behavior of the sidebands is not possible. The backgrounds point straight towards the beamspot, the same direction where the signal is expected to point back towards.

- The $\Delta\phi$ distributions show the presence of correlated emission between K_s^0 and Λ^0 $\left(\bar{\Lambda}^0\right)$ in jets. This correlated emission remains present even if the primary vertex associated with a hard event (such as the single muon) is cut out, as well as in the Zero Bias data sample where the events are softer in nature.

- The correlated emission is probably a real QCD/hadronization-related effect. Furthermore, this physics seems to be well described between data and the Monte Carlo hadronization simulations, although finding out precisely the hadronization processes behind it will need additional investigating.

- From comparing $\Delta\phi$ to the displacement of the S candidate to the beamspot, we see that high-displacement background is out of the box dominated by collinear $\Lambda^0 - K_s^0$ emission. This is because near-parallel $\Lambda^0 - K_s^0$ emission makes vertexing exhibit large uncertainty in the flight direction of the S candidate.

Jet-like emission as we've seen is only expected for or associated with highly relativistic, low mass particles, not for the GeV-range $\bar{S} + n \to K_s^0 + \bar{\Lambda}^0$ process considered here.

In the following section a comparison will be made of the results obtained so far to a simulation of what we expect actual signal to look like. The distributions resulting from this simulation will make it possible to define clear background-signal discriminating cuts for which we expect as good as no background for the data samples used.

6.5 Signal-background discrimination

6.5.1 Kinematic signal simulation

A small kinematics simulation was set up in order to produce p_T, $\Delta\phi$, $\Delta\eta$ and ΔR distributions that mimic what our signal of interest should look like [3]. The results of this kinematic simulation will be compared to the equivalent plots produced using the three previously used and discussed data and MC background samples.

The starting conditions and assumptions of the kinematic simulation are as follows:

- For the S particle
  - An S particle mass of 2GeV is assumed. This is the highest mass consistent with the S being effectively stable, as discussed in section 1.2.
  - A p_T distribution for the S particles is generated using the Tsallis distribution, which was introduced in section 3.1. The free parameter q in the Tsallis distribution was set to $q = 1.15$. The temperature variable T to 0.08GeV. These are the values as measured in the CMS experiment at $\sqrt{s} = 7$TeV [17].
  - A uniform pseudorapidity distribution was implemented with $\eta \in [-2.5; 2.5]$. This is because hadron production at the LHC exhibits rather flat η distributions [39].
  - A uniform azimuthal angular distribution was assumed with $\phi \in [0, 2\pi[$
- Given that the S is a spin-0 scalar, the following assumptions for the K_s^0 and Λ^0 correspond to the required spherical symmetry in the rest fame of the $S + n$ material interaction.
  - A uniform azimuthal angular distribution as assumed with $\phi \in [0, 2\pi[$
  - A θ distribution according to $\arccos(2 \cdot u - 1)$, where u is uniformly distributed in the $[0, 1]$ range.
  - Since this is done in the rest fame of the $S + n$ material interaction, the K_s^0 and Λ^0 resulting from the material interaction are sent out back-to-back

In the simulation, the S particle hits the neutron, which leads to the creation of the Λ^0 and K_s^0. This is essentially modeled as a simple 2-body decay in the $S + n$ rest frame, conserving total energy and keeping momentum balanced. Following this, a boost from the $S + n$ rest frame to the lab frame is applied to the K_s^0 and Λ^0 products, using the $S + n$ momentum.

Finally, events with a Λ^0 of $p_T < 1.5$GeV or a K_s^0 of $p_T < 0.9$GeV are cut and excluded from the resulting distributions. These cuts are the same as the ones discussed in section 5.1 and that were used in the Monte Carlo studies part of this work. It was checked that these cuts hardly affect the signal distribution.

6.5.2 Comparing signal with data/Monte Carlo

Figure 6.10 shows a comparison between the p_T distribution of the simulated S, which follows the Tsallis distribution, and the p_T distribution of the S candidates. The latter shows a clear 'kink' at $p_T = 2.4$GeV which corresponds to the combination of the $p_T < 0.9$GeV and the $p_T < 1.5$GeV cuts for respectively the K_s^0 and Λ^0 daughters of the S candidate. Since the first sub-figure is signal simulation and the second one comprises post-reconstruction background (as it only considers S candidates with a Λ^0, not an $\bar{\Lambda}^0$), a direct comparison between the two requires non-trivial unfolding of detector response and reconstruction effects, which is beyond the scope of this thesis.

Figure 6.11 shows the $\Delta\phi = \phi_{K_s^0} - \phi_{\Lambda^0}$, $\Delta\eta = \eta_{K_s^0} - \eta_{\Lambda^0}$ and $\Delta R = \sqrt{\Delta\phi^2_{K_s^0,\Lambda^0} + \Delta\eta^2_{K_s^0,\Lambda^0}}$ distributions between the simulated signal $S + n$ material interaction products. These are respectively shown in sub-figures 6.11a, 6.11b, and 6.11c.

Comparing the $\Delta\phi$ distribution between data/Monte Carlo (fig.6.5) and the $\Delta\phi$ distribution resulting from the kinematic simulation (fig.6.11a) shows two very different results. The $\Delta\phi$ distribution of the kinematic simulation shows a maximum around $|\Delta\phi| \approx 2.5\text{rad} \approx 140°$, which is simply the result of the boost to the lab-frame, while showing no sign of the jet-like correlated

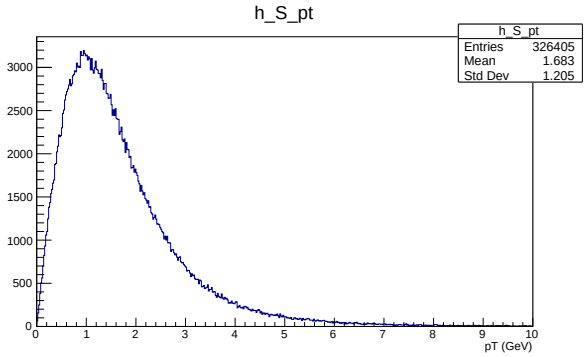

(a) The p_T distribution of the simulated S follows the Tsallis distribution with parameters $q = 1.15$ and $T = 0.08$GeV.

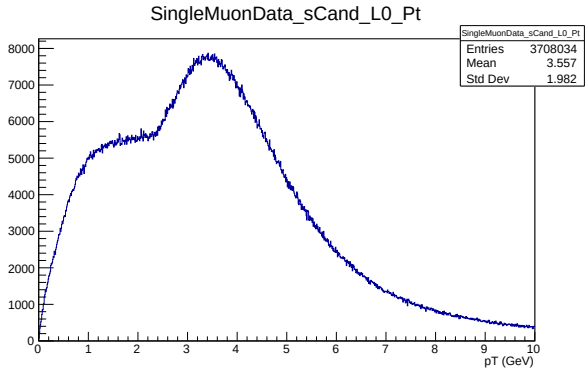

(b) The p_T distribution of the S candidates. The kink at 2.4GeV corresponds to the combination of the $p_T < 0.9$GeV and the $p_T < 1.5$GeV cuts for respectively the K_s^0 and Λ^0 daughters of the S candidate. Figure A.13 in the appendix shows the p_T distributions for the K_s^0 and Λ^0 daughters.

Figure 6.10

emission at $|\Delta\phi| \approx 0$ and $|\Delta\phi| \approx \pi$ that was observed for the data/Monte Carlo results shown in figure 6.5.

Comparing the $\Delta\eta$ distributions of the kinematic simulation (fig.6.11b) with the ones resulting from the three data/MC samples (fig.6.12), the difference induced by the jet-like correlated emission is clear. The kinematic simulation shows a smooth, bell-like-shaped distribution $\Delta\eta$, which is to be expected for a two body 'decay' that is back-to-back in the $S + n$ rest frame, while the $\Delta\eta$ distribution for the three data/MC samples shows a much more centrally spiked distribution with longer tails. While this effect is strongest in the Single Muon data sample (where the presence of a hard event might stimulate the presence of this correlated emission), it is present in all three of the samples.

The 'wobbles' that seem to be visible on top of the otherwise expected smooth, bell-shaped curve are present in both data and MC and can probably be traced back to differences in tracking inefficiencies for different η between the K_s^0 and Λ^0, although further investigation is required.

Combining the $\Delta\phi$ and $\Delta\eta$ distributions into a $\Delta R = \sqrt{\Delta\phi^2 + \Delta\eta^2}$ distribution results in figure 6.11c for the kinematic simulation and figure 6.13 for the three data/MC samples. Since the $\Delta\phi$ and $\Delta\eta$ distribution for the kinematic simulation peak at $|\Delta\phi| \approx 2.5$ and $|\Delta\eta| \approx 0$, the ΔR distribution peaks around $\Delta R \approx 2.5$ as well. In the absence of a spike in the $\Delta\phi$ distribution near $|\Delta\phi| \approx 0$, no spike is present in the ΔR distribution around $\Delta R \approx 0$. The ΔR distributions for the data/MC samples (fig.6.13) however tell a different story, especially in the case of the Single Muon data sample (fig.6.13a). Here the ΔR distribution shows a spike near the origin, indicating once again the jet-like correlated emission. Furthermore, the ΔR distributions in figure 6.13 peak at $\Delta R \approx \pi$ due to the peak in the $\Delta\phi$ distributions at $|\Delta\phi| \approx \pi$ for the three data/MC samples.

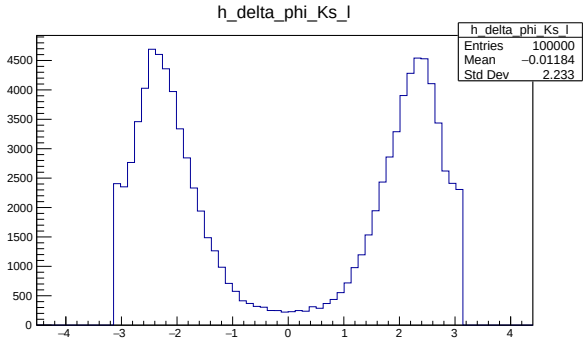

(a)

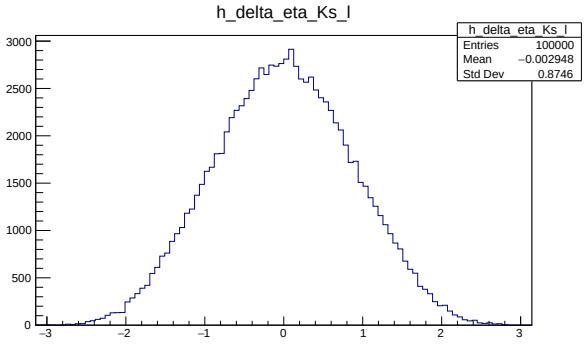

(b)

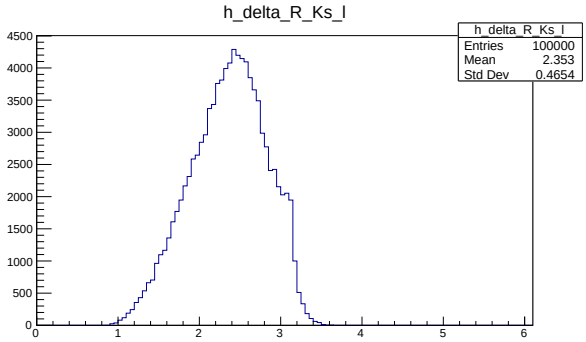

(c)

The $\Delta\phi = \phi_{K_s^0} - \phi_{\Lambda^0}$, $\Delta\eta = \eta_{K_s^0} - \eta_{\Lambda^0}$ and $\Delta R = \sqrt{\Delta\phi^2_{K_s^0,\Lambda^0} + \Delta\eta^2_{K_s^0,\Lambda^0}}$ distributions between the simulated signal $S + n$ material interaction results: K_s^0 and $\Lambda^0\left(\bar{\Lambda}^0\right)$. These are respectively shown in sub-figures 6.11a, 6.11b, and 6.11c. [3]

Figure 6.11

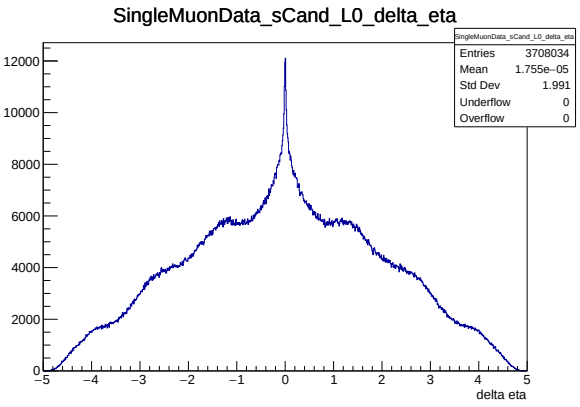

(a)

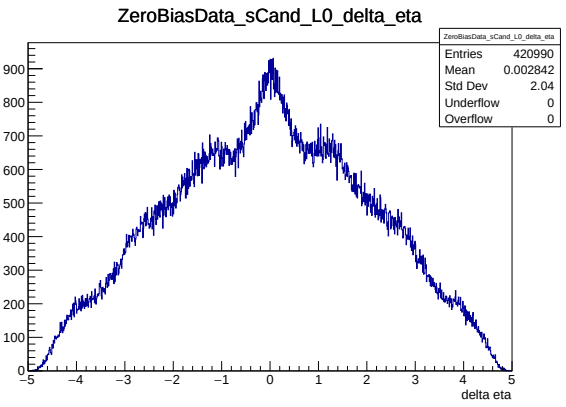

(b)

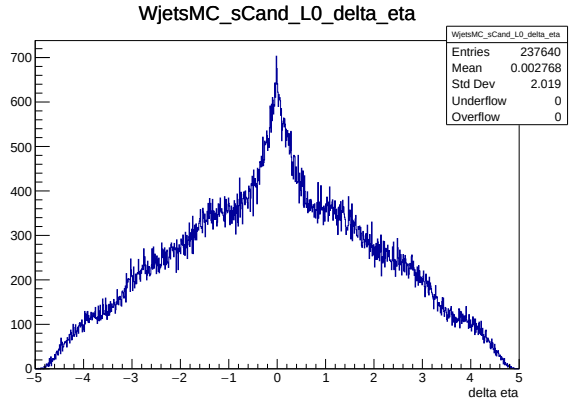

(c)

These figures show the distributions of $\Delta\eta = \eta_{K_s^0} - \eta_{\Lambda^0}$ between the S candidate's daughter K_s^0 and Λ^0. This is done for the Single Muon data sample, the W+jets Monte Carlo sample, and the Zero Bias data sample.

Figure 6.12

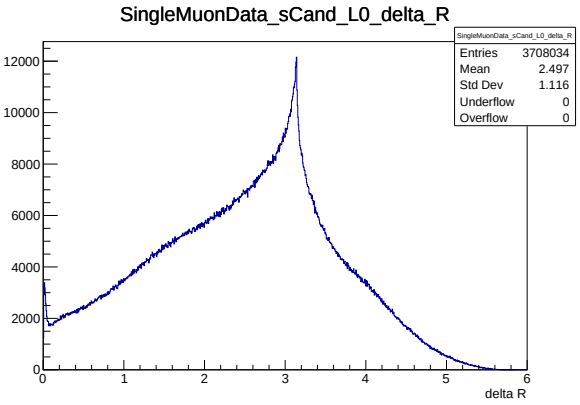

(a)

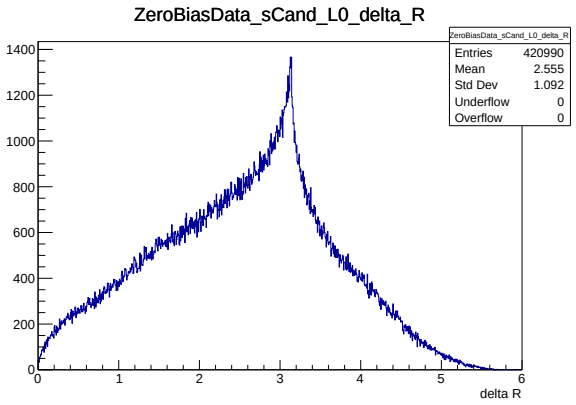

(b)

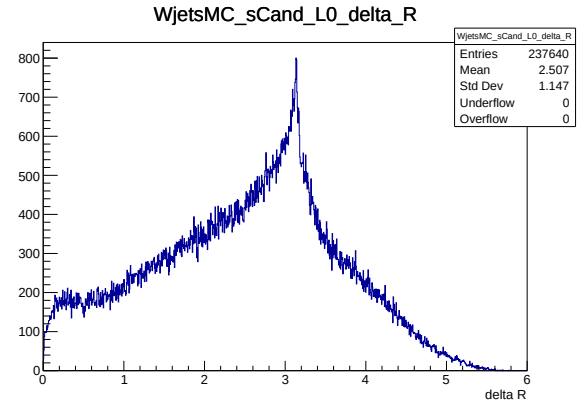

(c)

These figures show the distributions of $\Delta R = \sqrt{\Delta\phi^2_{K^0_s,\Lambda^0} + \Delta\eta^2_{K^0_s,\Lambda^0}}$ between the S candidate's daughter K^0_s and Λ^0. This is done for the Single Muon data sample, the W jets Monte Carlo sample, and the Zero Bias data sample.

Figure 6.13

6.5.3 Interesting correlations between $\Delta\phi$ and $\Delta\eta$

Figure 6.14a shows a 2D scatter plot between $\Delta\phi$ and $\Delta\eta$ for the Single Muon data sample. The results for the other two samples are similar and can be found in Appendix A.6. Scatter plots where $\Delta\phi$ is compared to $\Delta\theta$ can be found there as well.

Figure 6.14a shows an interesting correlation between $\Delta\phi$ and $\Delta\eta$. First of all, a clear spike is visible at $\Delta\phi = \Delta\eta = 0$, corresponding to the previously discussed spike in the ΔR distribution at $\Delta R = 0$ (Fig.6.13a). Next to that, the increase in $\Delta\phi$ is visible at the left and right side of the scatter plot. This corresponds to the spikes in the $\Delta\phi$ distributions (which are essentially a projection of this scatter plot on the x-axis). Finally, we notice the two vertical 'beams' coming out of the top and bottom of the origin, indicating some interesting interplay between the two variables.

These correlations remind of the results discussed in a paper on the "Observation of Long-Range, Near-Side Angular Correlations in Proton-Proton Collisions at the LHC" [38]. The relevant result is shown in figure 6.14b where a 2D two-particle correlation functions for 7TeV proton-proton high multiplicity events with $1 < p_T < 3$GeV is shown. Comparing figures 6.14a and 6.14b shows clear similarities in the correlation of $\Delta\phi$ and $\Delta\eta$. However, the effect measured in this paper is only present for very high multiplicities, in other words in a very specific part of the phase-space. The effects in figure 6.14a, on the other hand, shows these correlation effects without any dedicated selection, as well as in the Monte Carlo W+jets sample. The correlations we observed are not yet fully understood. This is still an open question which requires further research beyond the scope of this thesis.

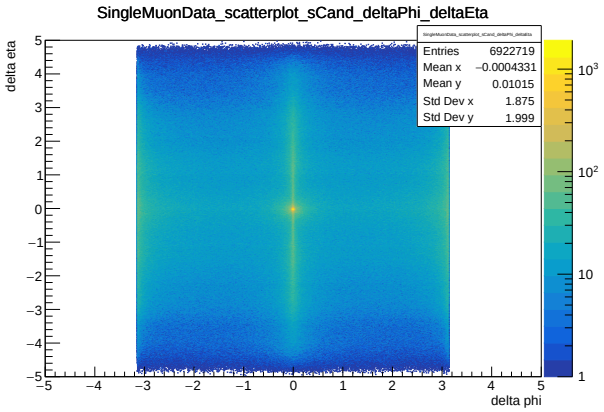

(a) A 2D scatter plot between $\Delta\phi$ and $\Delta\eta$ for the Single Muon data sample. The results for the other two samples can be found in Appendix A.6.

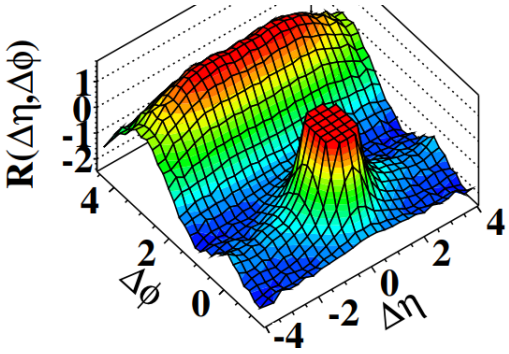

(b) This figure shows a 2D two-particle-track correlation functions for 7TeV proton-proton high multiplicity (Number of offline tracks greater than 110) minimum bias events with $1 < p_T < 3$GeV. The sharp near-side peak from jet correlations is cut off in order to better illustrate the structure outside that region. The details of the correlation function can be found in [38].

Figure 6.14

6.5.4 Defining cuts

The difference between kinematic simulation and data/MC samples for the $\Delta\eta$ distributions is not very clear-cut, which is the case for the $\Delta\phi$ distributions previously discussed. For that reason, no cuts will be devised based on the $\Delta\eta$ distributions. For the same reason, it is not easy to distinguish the ΔR distributions between signal and data/MC in a simple manner, and therefore the ΔR distributions are not used for basing cuts on either.

The clearest difference between simulated signal and data/MC is obtained through the $\Delta\phi$ plots. For this reason, and because it will be shown to be sufficient for our purposes, this is what the signal-background discriminating cuts are based on.

Since the signal simulation is a very simple, artificially put in place, back-of-the-envelop generated kinematic process involving only the $\bar{S}+n \to K_s^0+\bar{\Lambda}^0$ process, it does not provide any information about the displacement of the $S+n$ interaction vertex to the beamspot. Because of this no 2D scatter plots comparable to figure 6.8 for the data/MC samples are available for the simulated signal. What can be known for sure is that the $S+n$ material interaction can only happen in material, so even without any sort of detailed simulations, we know that within the displacement of about 2cm distance from the beamspot, which is where the beampipe material is located, no signal will be present. Given the very good vertex position resolution for non-quasiparallel tracks, anything within a displacement of 1.9cm can be considered background to the expected signal.

Based on the previous it is clear that an effective background-signal discriminating cut can be defined in the following manner:

- Cut away Λ^0 of $p_T < 1.5$GeV or a K_s^0 of $p_T < 0.9$GeV
- Cut away the jet-like correlated emission between K_s^0 and Λ^0 by cutting away $\left|\Delta\phi_{K_s^0,\Lambda^0}\right| < 1$ and $\left|\Delta\phi_{K_s^0,\Lambda^0}\right| > 2.5$, leaving the range $1 < \left|\Delta\phi_{K_s^0,\Lambda^0}\right| < 2.5$ intact.
- Cut away everything with an S candidate's vertex position within a distance in the xy-plane of 1.9cm from the beamspot.
  - Additionally a cut on the standard deviation of this distance for $\sigma_{d_{xy}} < 0.1$cm is applied.

These cuts (apart from the $\sigma_{d_{xy}}$ cut) are visually represented on figure 6.15. A visual representation that includes the $\sigma_{d_{xy}}$ cut is shown in figure 6.17.

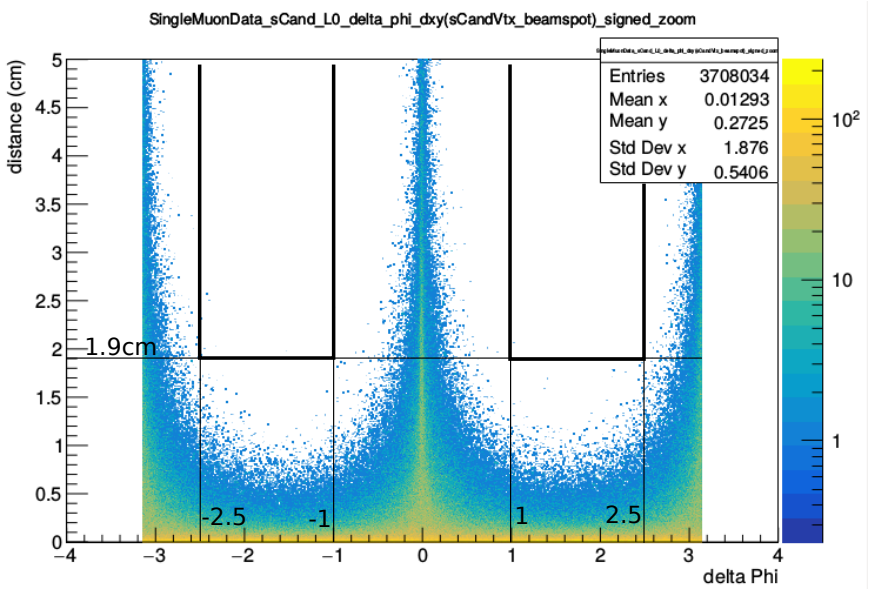

Figure 6.15: Graphical clarification of the defined cuts. The area outside the two bold rectangles is cut away.

6.5.5 S candidate vertex position accuracy

For the displacement cut at 1.9cm to be well-defined, it is important that the uncertainty on the S candidate vertex positioning, for S candidates that pass the $\Delta\phi$ cut, is sufficiently small. The beamspot location can be assumed to be essentially exact, as it is calculated as an average using many tracks over many events. This means that the S candidate vertex position is the only source of error on the displacement measure, which the 1.9cm cut is defined on. Figure 6.16 shows the distribution of the standard deviation on the distance in the xy-plane between the S candidate vertex position and the beamspot location. This is for S candidates that pass the $1 < |\Delta\phi| < 2.5$ cut. The vast majority of the standard deviations lie below 1mm, meaning that the S candidate vertex position is sufficiently well defined. S candidates that lie outside this $\Delta\phi$ range are associated with the jet-like correlated emission of K_s^0 and Λ^0, giving rise to large uncertainties in these S candidate's positioning and a long tail in the distribution of standard deviations.

Figure 6.17 shows a two dimensional scatter plot with on the x-axis the distance in the xy-plane between the S candidate vertex position and the beamspot location, and on the y-axis the standard deviation of this distance. In the second sub-figure the previously discussed $1 < |\Delta\phi| < 2.5$ cut is applied, where $\Delta\phi$ is the azimuthal angle between the K_s^0 and the Λ^0 daughters of the S candidate. These plots are the results of the Single Muon data sample. The other two samples give analogues results. This figure shows that the effect of applying the $\Delta\phi$ cut, or in other words cutting out the jet-like correlated emission, is that the majority of S candidates with distance (in the xy-plane) to the beamspot of larger than 2cm (the distance of the first material layer) and with large uncertainty on this distance are cut away. In other words, most of the S candidates that lie within material are associated with the jet-like correlated emission.

The area inside of the bold rectangle in this sub-figure illustrates the signal-background discriminating cuts which are to be applied to the S candidates.

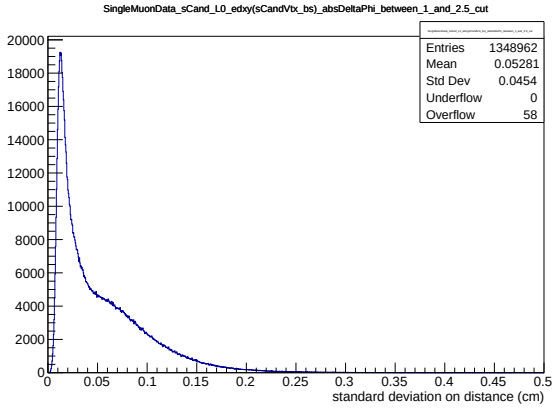

Figure 6.16: The distribution of standard deviation on the distance in the xy-plane between the S candidate's vertex position and the beamspot. A $1 < \Delta\phi < 2.5$ cut is applied. The majority of the standard deviations are sub-millimeter. This is for the Single Muon data sample. The results for the other two samples look near identical.

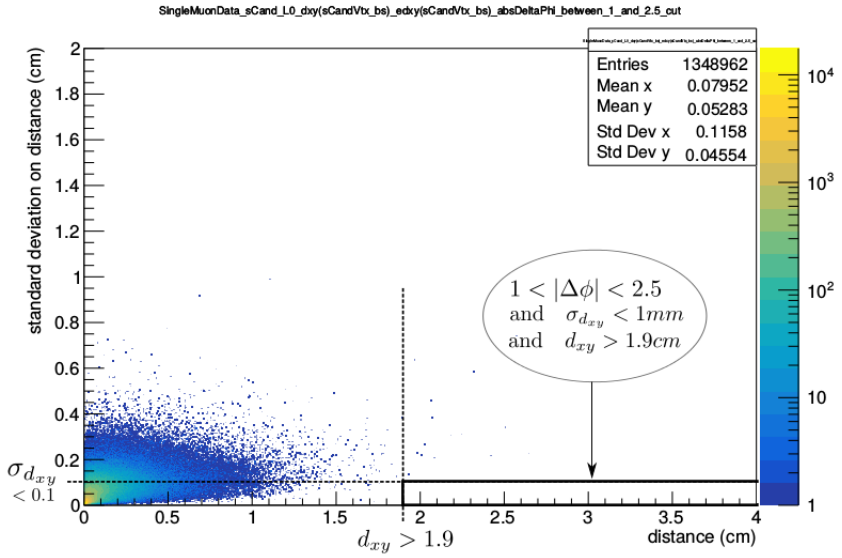

Figure 6.17: A 2D scatter plot with on the x-axis the distance in the xy-plane between the S candidate vertex position and the beamspot location, and on the y-axis the standard deviation of this distance. A $1 < |\Delta\phi| < 2.5$ cut is applied, where $\Delta\phi$ is the azimuthal angle between the K_s^0 and the Λ^0. This is for the Single Muon data sample. The other two samples look very similar to this. The area inside of the bold rectangle illustrates the cuts which S candidates have to pass in order to be considered as signal as opposed to background.

A quick summary of the background-signal discriminating cuts described so far:

- Λ^0 of $p_T < 1.5$GeV and K_s^0 of $p_T < 0.9$GeV are cut.
- We cut away $\left|\Delta\phi_{K_s^0,\Lambda^0}\right| < 1$ and $\left|\Delta\phi_{K_s^0,\Lambda^0}\right| > 2.5$, leaving the range $1 < \left|\Delta\phi_{K_s^0,\Lambda^0}\right| < 2.5$ intact. This gets rid of the jet-like correlated emission between K_s^0 and Λ^0.
- We cut away everything with an S candidate's vertex position within a distance in the xy-plane of 1.9cm from the beamspot.
  - An additional requirement is that the standard deviation of this distance, $\sigma_{d_{xy}}$, has to be below 0.1cm.

6.6 Mass distributions and partial unblinding

In this section the previously established background-signal discriminating cuts will be put to practice on the mass distribution plots for the S (and $\bar{S}$). This will be done for the three samples: the Single Muon triggered data sample, the Zero Bias data sample, and the W jets triggered MC sample. This mass is calculated using equation 6.3, which for the convenience of the reader is repeated here:

$$m^2_{S_{cand}} = \left(E_{\Lambda^0} + E_{K^0_s} - m_n\right)^2 - \left(\vec{p}_{\Lambda^0} + \vec{p}_{K^0_s}\right)^2 \tag{6.5}$$

Here the subscripts S_{cand} should be replaced by $\bar{S}_{cand}$ and the subscript Λ^0 if replaced by $\bar{\Lambda}^0$ when the mass of the actual signal $\bar{S}$ is calculated.

Looking at the resulting distributions for the $\bar{S}$ and the associated $\bar{\Lambda}^0$ leads to the partial unblinding to the signal. This is only partial in the sense that the Single Muon and Zero Bias data samples constitutes but a fraction of the total data available. These cuts and unblinding was done as a proof of concept for the sake of this Master thesis and further unblinding and cut-defining should of course be carried out with much greater care than was achievable in the few months time available for this work.

Figure 6.18a, 6.18b and 6.18c show for all three samples the distributions of S (blue) and $\bar{S}$ (red) candidate masses, the first one of which consists entirely of background and the second one of which contains the actual signal that is being investigated. These distributions have none of the cuts applied to them, they are fully inclusive.

Figures 6.18d, 6.18e and 6.18f show the distributions of S (blue) and $\bar{S}$ (red) candidate masses. Once again, S candidates constitute background and $\bar{S}$ signal. These distributions have solely the $1 < |\Delta\phi| < 2.5$ cut applied to them, where $\Delta\phi$ is the azimuthal angle between the K^0_s and the Λ^0 ($\bar{\Lambda}^0$).

The mass distributions for only the $\Delta\phi$ cut being applied (the last three sub-figures) shows at first sight the same shape as the distributions without any cuts applied to them (the first three sub-figures), not indicating anything significant.

Lastly, the distributions of S and $\bar{S}$ candidate masses with the $1 < |\Delta\phi| < 2.5$ cut, as well as the $d_{xy} > 1.9$cm and the $\sigma_{d_{xy}} < 0.1$cm cuts were investigated. Here d_{xy} is the displacement (in the xy-plane) between the S or $\bar{S}$ candidate fitted vertex position and the beamspot location, and $\sigma_{d_{xy}}$ is the standard deviation of this distance. No events passed this selection.

Solely applying the distance cut without the cut on $\Delta\phi$ would not make sense, since then only background is shown.

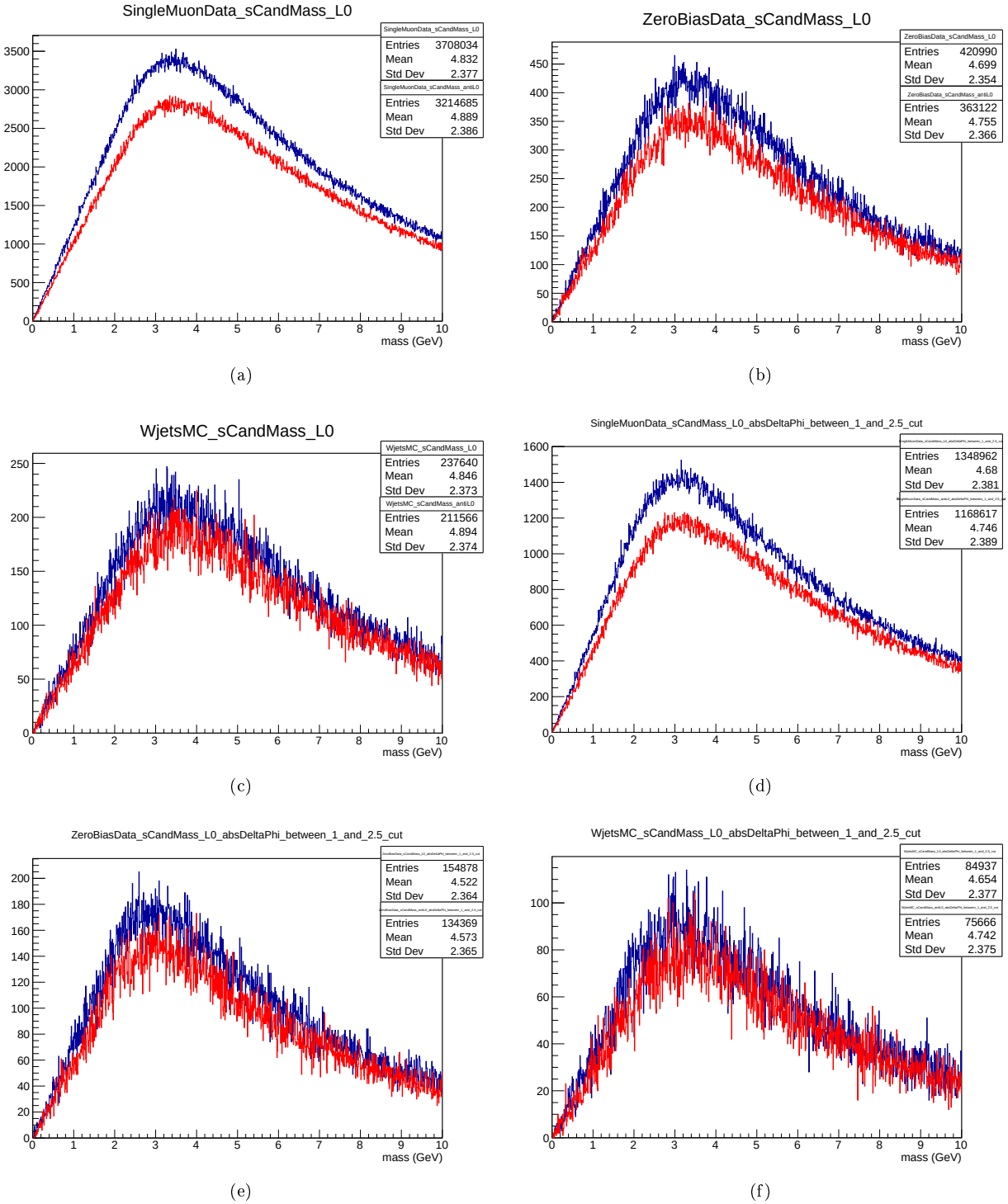

Figure 6.18: The blue colored plots are for the S candidates (the fit of a K_s^0 and a Λ^0), while the red colored plots are for the $\bar{S}$ candidates (the fit of a K_s^0 and a $\bar{\Lambda}^0$). The first three sub-figures (a, b and c) have no cuts applied to them, while the last three sub-figures (d, e and f) have the $1 < |\Delta\phi| < 2.5$ cut applied.

Chapter 7

Conclusion

The S and $\bar{S}$ mass distributions for with and without the $\Delta\phi$ cut closely mimic one another (apart from statistical fluctuations and the fact that there are less $\bar{S}$ candidates than S candidates present).

The final S and $\bar{S}$ mass distributions with all the cuts applied resulted in empty histograms (and are hence not shown), meaning that no S nor $\bar{S}$ candidates survived the combinations of all previously mentioned cuts and no signal was seen.

7.1 Setting limits on the $\bar{S}$ production cross section

Now that no signal has been discovered, the next point is to trace back our steps and attempt to set a limit on the production cross section of the hypothetical $\bar{S}$ in the pp collisions at $\sqrt{s} =$ 13TeV. This is done through a back-of-the-envelope calculation of unfolding the reconstruction efficiencies (which were discussed in section 5.6) in combination with the p_T distributions resulting from the signal simulation. To accomplish this, a few approximations and assumptions need to be made on the relevant quantities for this calculation. The resulting limit on the $\bar{S}$ production cross section will be compared to the initial, very rough, order-of-magnitude estimate discussed in section 1.4. This estimation yielded an S production cross section, $\sigma_{guess}\left(pp \to \bar{S}\right)$, between $2.4 \cdot 10^{-1}$ and $2.4 \cdot 10^{-3}$mb. Ideally the resulting upper limit on the cross section will be smaller than this guesstimate in order to exclude S production under the given hypothesis.

7.1.1 Reconstruction efficiencies

In this section, the results from the Monte Carlo studies are used to find out the average, overall reconstruction efficiency ϵ_S to reconstruct an S candidate. This efficiency is determined by three factors: the K_s^0 and Λ^0 reconstruction efficiencies, the efficiencies due to the application of pre-selection cuts, and the selection efficiency due to background rejection, which rejects also part of the signal.

Figures 5.8, 5.11 and 5.13 from section 5.6 show the K_s^0 and Λ^0 reconstruction efficiencies in function of respectively p_T, η and displacement between decay vertex and the PV. Since the reconstruction efficiencies in function of η and displacement (taking into account the error bars) are reasonable 'flat', they will not be considered in the following calculation. The reconstruction efficiencies do however show a strong p_T dependence, providing us with the big picture, and hence only these will be considered.

The plateau in the p_T dependence of the K_s^0 reconstruction efficiency (fig. 5.8) at about 40% efficiency is dominated by the inefficiency due to displacement, which (as can be seen in fig. 5.13) follows a fairly flat distribution. On the scale of a few millimeters of displacement this would not be correct, since at those displacement scales the tracker is very efficient. However, the majority of the K_s^0 and Λ^0 decay several centimeters away from the PV.

From $p_T = 3$GeV onward, the K_s^0 reconstruction efficiency was taken to be a constant value of 40% for the following calculation. Similarly, from $p_T = 4$GeV onward, the Λ^0 reconstruction efficiency was taken to be equal to a constant value of 55%. Approximating these values in these

p_T ranges is valid since the total fraction of K_s^0 and Λ^0 from $\bar{S}+n$ interactions in these p_T ranges is negligible.

The p_T distributions for the K_s^0 and $\bar{\Lambda}^0$ daughters from the signal simulation were used in combination with the K_s^0 and Λ^0 reconstruction efficiency distributions to obtain the overall K_s^0 and Λ^0 reconstruction efficiency distributions. These overall efficiencies then include the effect of the following cuts which were applied to these K_s^0 and Λ^0 :

- A $p_T > 0.9$GeV cut for K_s^0 and a $p_T > 1.5$GeV cut for Λ^0
- Both K_s^0 and Λ^0 lie within tracker acceptance of $|\eta| < 2.5$

Figure 7.1 shows the resulting reconstruction+cut efficiency distributions of the K_s^0 and Λ^0 as a function of the p_T of their mother Sexaquark.

Convoluting the simulated signal S p_T distribution (fig. 6.10a) with these overall K_s^0 and Λ^0 reconstruction+cut efficiency distributions results in an overall efficiency for reconstructing an S particle of $\epsilon_{reco+cuts} = 4.4\%$. Keeping in mind the fact that applying the $1 < |\Delta\phi| < 2.5$ cut rejects approximately 34% of the signal[1], an additional selection efficiency of $\epsilon_{select} = 100\% - 34\% = 66\%$ needs to be taken into account. The overall efficiency to reconstruct an S particle then becomes $\epsilon_S = \epsilon_{select} \cdot \epsilon_{reco+cuts} = 2.9\%$.

A value of this magnitude could be expected for the reconstruction of 4 displaced tracks (the three pions and proton from which the K_s^0 and Λ^0 were originally reconstructed) with low values of p_T, which is a p_T region with low track reconstruction efficiency.

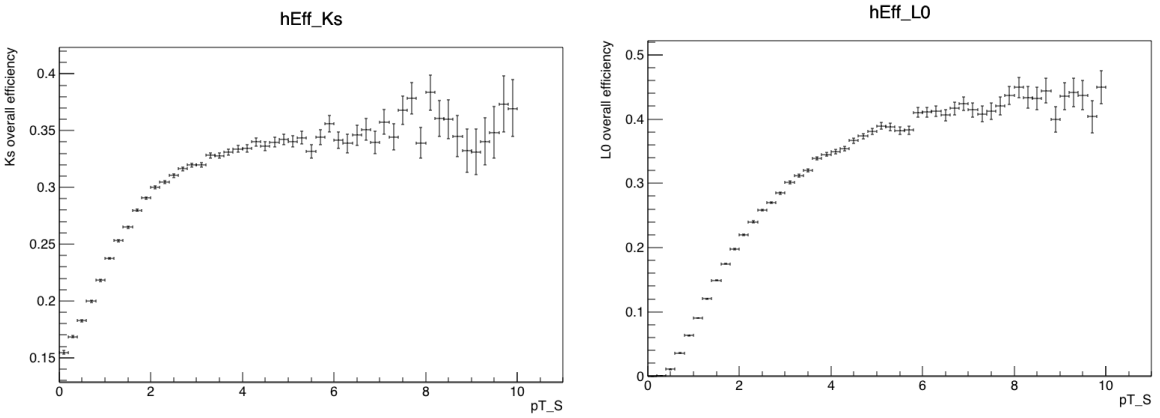

(a) (b)

Figure 7.1: The overall K_s^0 and Λ^0 (in that order) reconstruction+cut efficiencies in function of the S transversal momentum (in GeV). The K_s^0 and Λ^0 have a $|\eta| < 2.5$ cut applied to them, as well as a $p_T < 0.9$GeV cut for K_s^0 and a $p_T < 1.5$GeV cut for Λ^0. [3]

7.1.2 Calculating the limit

The Single Muon data sample we considered contains about 150 million events. At an average pile-up (measured for the considered LHC run period) of $\langle PU \rangle = 27$ and subtracting one from this amount to account for the fact that the cuts effectively cut out one of the primary vertices (the one with the hard muon) this results in the following total number of proton-proton collisions:

$$N_{pp-collions} \approx N_{events} \cdot (\langle PU \rangle - 1) \approx 150 \cdot 10^6 \cdot (27 - 1) = 3.9 \cdot 10^9 \tag{7.1}$$

Given a proton-proton inelastic cross section of $\sigma_{pp} \approx 70$mb [28], this results in a total integrated luminosity for the Single Muon data sample of: $\mathcal{L}_{pp} = \frac{N_{pp}}{\sigma_{pp}} \approx \frac{3.9 \cdot 10^9}{70\text{mb}} = 5.6 \cdot 10^7 \text{mb}^{-1} = 0.056\text{pb}^{-1}$.

The number of observed $\bar{S}$ is then given by

[1] The $d_{xy} > 1.9$cm displacement background cut is not expected to cut away any signal, since no matter is present and hence no material interactions can take place below this displacement.

$$N_{obs} = \mathcal{L}_{pp} \cdot \sigma\left(pp \to \bar{S}\right) \cdot P\left(\bar{S}+n\right) \cdot \epsilon_S \tag{7.2}$$

where $\sigma\left(pp \to \bar{S}\right)$ is the unknown $\bar{S}$ production cross section, $P\left(\bar{S}+n\right)$ is the probability for material interactions to occur between $\bar{S}$ and a neutron, and ϵ_S is the overall reconstruction efficiency for reconstruction of an $\bar{S}$ candidate.

Now, let μ be the expectation value for the number of events one would observe in any experiment. When an experiment is performed, N_{obs} events are observed, the value of which follows a Poisson distribution:

$$P\left(N\right) = e^{-\mu} \cdot \frac{\mu^N}{N!} \tag{7.3}$$

No signal was observed in the search described before, meaning that $N_{obs} = 0$.

The value of μ for which, given that $N_{obs} = 0$, we can exclude with a 95% confidence level that the number of expected events was larger or equal to μ, is given by the following equation:

$$100\% - 95\% = 5\% = P\left(0\right) = e^{-\mu_{95CL}} \tag{7.4}$$

$$\iff \mu_{95CL} = -\ln\left(0.05\right) \approx 3 \tag{7.5}$$

From this follows that the upper limit on the amount of observed events, at a 95% confidence level and given that $N_{obs} = 0$, is given by $N_{obs}^{UL} = \mu_{95CL} = 3$.

The $\bar{S}+n$ material interaction probability, $P\left(\bar{S}+n\right)$, is then left to be guesstimated. A full estimation for the $\bar{S}+n$ material interaction probability would require an integration over all material layers, including a convolution with the probability of reconstructing the tracks at a certain distance and in a given material layer. This track reconstruction probability diminishes at larger displacements. This is a highly complex calculation and lies beyond the scope of this thesis.

The CMS detector material budget distributions (fig. 2.2) show that the pixel detector, the support tube, the TIB, TOB, TID and the TEC material layers are all expected to induce much more material interactions than the beampipe. The estimation in this thesis uses the vastly simplified assumption that nearly all of the $\bar{S}+n$ material interactions occur in the beampipe. At a later stage, the calculation will be extended to include the pixel detector. Given that in reality the opposite is true, the in this work estimated material interaction probability will be lower than the result of a more involved calculation. A lower value for $P\left(\bar{S}+n\right)$ will result in a higher, more conservative value for the upper bound on the S production cross section. On the other hand, given that the track reconstruction probability diminishes at larger displacements and therefore is still fairly high near the beampipe, this approximation might not be too far-fetched.

An alternative approach might be to approximate the $\bar{S}+n$ material interaction probability with the probability for a promptly produced neutron to interact with material, although here too the displacement-dependent track reconstruction efficiencies of the nuclear interaction products would have to be taken into account.

The beampipe, being made of beryllium [35], has a mass density of $\rho_{Be} = 1.85\text{g/cm}^3$. The majority of the material interactions occur over a distance of approximately $dr = 0.1\text{cm}$ inside of the beryllium beampipe, as can be deduced from figure 7.2. The column mass density of beryllium, integrated over this depth of $dr = 0.1\text{cm}$, is given by $\rho_{Be}^{column} = \rho_{Be} \cdot dr = 1.85\text{g/cm}^3 \cdot 0.1\text{cm} \approx 0.19\text{g/cm}^2$. Given that the mass of a beryllium nucleus is $m_{Be} = 1.5 \cdot 10^{-23} g$, the column beryllium-nuclei number density is $n_{Be}^{column} = \rho_{Be}^{column}/m_{Be} \approx 1.3 \cdot 10^{22}\text{nuclei/cm}^2$.

As ${}^{9}_{4}Be$ is the only naturally occurring isotope, the beryllium nucleus consists of 5 neutrons and 4 protons, making the column neutron number density equal to $n_{neutron}^{column} = 5 \cdot n_{Be}^{column} \approx 6.5 \cdot 10^{22}\text{neutrons/cm}^2$.

The $\bar{S}+n$ material interaction probability, $P\left(\bar{S}+n\right)$, is now given by the product of the $\bar{S}+n$ inelastic cross section, $\sigma\left(\bar{S}+n\right)$, and the column number density of the neutrons in beryllium over this 0.1cm distance, $n_{neutron}^{column}$.

Here $\sigma\left(\bar{S}+n\right)$ can be approximated to be the inelastic neutron-neutron cross section, σ_{nn}^{inel}, suppressed by a factor of 10^{-6} [1]. Furthermore, σ_{nn}^{inel} is taken to be equal to the proton-proton inelastic cross section at $\sqrt{s} = 13\text{TeV}$, namely $\sigma_{pp}^{inel} \approx 80\text{mb}$. This results in a total $\bar{S}+n$ interaction probability estimate of

$$P\left(\bar{S}+n\right) = n_{neutron}^{column} \cdot \sigma\left(\bar{S}+n\right) \approx 6.5 \cdot 10^{22}{}^{\text{neutrons}}/_{\text{cm}^2} \cdot 80\text{mb} \cdot 10^{-6} = 5.2 \cdot 10^{-9} \tag{7.6}$$

In addition to that, beryllium has a nuclear interaction length of 42cm [15], meaning that the beampipe thickness of 0.1cm is equivalent to 0.0024 of such interaction lengths. In figure 2.2, which shows the tracker material budget, it can be seen that the pixels and the beampipe in the central region contribute to about 0.02 interaction lengths. If we consider interactions in the central pixel material to still be well trackable, which is a reasonable assumption to make, then an additional factor of ${}^{0.02}/_{0.0024} = 8.3$ can be added to $P\left(\bar{S}+n\right)$. This results in:

$$P\left(\bar{S}+n\right) \approx 8.3 \cdot 5.2 \cdot 10^{-9} \approx 4.3 \cdot 10^{-8}$$

The upper limit on the $pp \to \bar{S}$ production cross section, at a 95% confidence level, is then given by:

$$\sigma_{95CL}^{UL}\left(pp \to \bar{S}\right) = \frac{N_{obs}^{UL}}{\epsilon_S \cdot \mathcal{L}_{pp} \cdot P\left(\bar{S}+n\right)} \tag{7.7}$$

$$\approx \frac{3}{0.029 \cdot 0.056\text{pb}^{-1} \cdot 4.3 \cdot 10^{-8}} \tag{7.8}$$

$$\approx 4.3 \cdot 10^{10}\text{pb} = 43\text{mb} \tag{7.9}$$

This upper level production cross section can then be compared to the previously discussed order of magnitude estimation of $\sigma_{guess}\left(pp \to \bar{S}\right) = 2.4 \cdot 10^{-3}$ to $2.4 \cdot 10^{-1}$mb. This estimate is still about two to four orders of magnitude below the $4.3 \cdot 10^{1}$mb value of $\sigma_{95CL}^{UL}\left(pp \to \bar{S}\right)$.

Ideally $\sigma_{95CL}^{UL}\left(pp \to \bar{S}\right)$ would have been smaller than $\sigma_{guess}\left(pp \to \bar{S}\right)$, since this would allow to exclude S production under the given hypothesis.

One way to achieve this would be to increase the size of the used data samples with a factor $\sim 10^2$ to $\sim 10^4$ from about 150 million events to about 15 billion or in the conservative case even 1.5 trillion events. Given an average pile-up of $\langle PU \rangle = 27$, this corresponds to about 5.6pb^{-1} to $560\text{pb}^{-1}$of integrated luminosity. Given that these 150 million events represent about 4% of the integrated luminosity of data taken in 2016, an increase of just a factor 10^2 would already correspond to using data of at least 4 years.

Given that this highly simplified calculation likely overestimates the result of $\sigma_{95CL}^{UL}\left(pp \to \bar{S}\right)$, a more careful and involved calculation might result in a more favorable outcome.

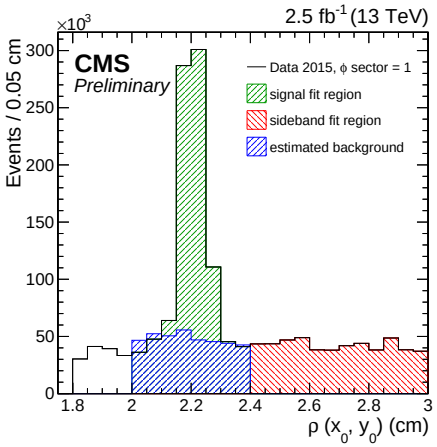

Figure 7.2: This figure was used for the subtraction of the combinatorial background near the beam pipe reconstructed with nuclear interactions using 2015 Data. Nuclear interactions are here defined as interactions of hadrons with material. The peak corresponds with the the beam pipe. The beam pipe radius is parametrized by $\rho = \sqrt{(x-x_0)^2 + (y-y_0)^2}$, where x_0 and y_0 are the coordinates of the center of the beam pipe. The individual bins have a width of 0.05cm. Given that the peak is roughly 2 bins wide, it can be said that the majority of nuclear interactions take place over a width of about 0.1cm or less. [29]

Chapter 8

Outlook

It looks like the Standard Model will have to, at least for now, admit defeat. But fear not, there is still new hope on the horizon. The following points give a brief summary of the future outlook of this investigation adventure. Who knows, the Sexaquark dark matter candidate might yet show itself.

One major next step is the further unblinding, scaling up and expansion of the analysis to all primary datasets, making the total number of events investigated orders of magnitude larger in size than what was used in this thesis. The unblinded data, being 150 million events (0.06pb^{-1}) for the Single Muon data sample, represents only 4% of the total integrated luminosity of pp collision without trigger selection applied available for just 2016, which is 1.4pb^{-1}. There are vast amounts of data yet to be explored. Expanding to more datasets includes checking for differences between those different data and MC sets. So far, the samples investigated in this thesis behaved very similar in the signal region. It will become important to do proper accounting of the differences in pile-up conditions between events recorded by different triggers in different data samples.

Another future step would be the creation of a proper, more accurate signal simulation. The one used in this work was made in a simplified, 'back-of-the-envelope' fashion, and did for example not contain any information about impact parameters or other distances of the S to the beamline. A proper simulation would include the actual interactions between the $\bar{S}$ and all of the detector material, taking into account the material properties and density distributions.

Next to that, acquiring a better understanding of the models for hadron forming in Pythia is needed to understand the processes responsible for the observed correlated emission of K_s^0 and Λ^0 pairs, as well as the $(\Delta\eta, \Delta\phi)$ correlations discussed in section 6.5.3.

Based on future, new insights into what signal should look like, as well as into the models for hadron forming in Pythia, the signal-background differentiating cuts defined in this work will likely undergo tweaking and refining. As a result of this, the prediction of the background mass distribution will continue to improve.

Fermi motion of the nucleons (neutron) inside the materials could potentially affect the energy-momentum and thus the mass distribution of the S candidates. Fermi motion has associated momenta of up to 250MeV [19]. This effect could be simulated by assigning the neutron, which was in this thesis assumed to be fully at rest, a properly distributed momentum. A proper inclusion of this effect could induce an additional smearing of the S candidate mass distribution.

If further unblinding and expansion to more datasets results in the final, post-cut $\bar{S}$ mass distribution having sufficient statistics, then a proper bump-hunt could take place. One could fit a straight line through the background mass distribution and then look for non-Gaussian-distributed deviations from that line in the $\bar{S}$ mass distribution.

A more precise calculation of the upper limit on the S production cross section is another working point. The very rough estimation presented in this work makes the assumption that most $\bar{S}+n$ material interactions take place in the beampipe and pixel material, and also that the neutrons in the beryllium beampipe are evenly distributed throughout the material. The result in this work can be considered as a rough order-of-magnitude estimation, but a more detailed calculations will have to be performed.

Finally, next to the $\bar{S} + n \rightarrow \bar{\Lambda}^0 + K_s^0$ process focused of this work, additional interaction processes, such as the $\bar{S} + n \rightarrow \pi^- + \bar{\Xi}^+$ process mentioned in section 4.2, could be investigated in more detail. This channel will for sure be needed to confirm a possible observation in the discussed $\Lambda^0 - K_s^0$ channel, since it will allow to confirm double strangeness of the interacting S particle, which is not possible in the $\Lambda^0 - K_s^0$ case because of $K^0 - \bar{K}^0$ oscillations.

As you can see, this story isn't over yet. A lot of work still has to be done. Prof. Lowette, Jarne, Prof. Vanlaer, as well as all future researchers involving themselves in this endeavor still have quite a journey ahead of them. I wish them success and all the luck they need to bring that journey to a good end.

Bibliography

[1] Glennys R. Farrar, *Stable Sexaquark*, arXiv:1708.08951v1[hep-ph]

[2] S. Lowette Internal communications

[3] J. De Clercq Internal communications

[4] Sang-HoKim et al., *Heavy pentaquark states $P_c(4380)$ and $P_c(4450)$ in the J/Ψ production induced by pion beams off the nucleon*, Phys-Lett-B.2016.10.061

[5] R. L. Jaffe, *Perhaps a Stable Dihyperon*, Phys. Rev. Lett. 38, 195 (1977); Erratum Phys. Rev. Lett. 38, 617 (1977)

[6] J. K. Ahn et al., *Production of $\Lambda\Lambda 4H$ Hypernuclei*, Phys. Rev. Lett. 87, 132504 (2001).

[7] H. Takahashi et al., *Observation of a ${}^{6}_{\Lambda\Lambda}He$ Double Hypernucleus*, Phys. Rev. Lett. 87, 212502 (2001).

[8] B. H. Kim et al. (Belle), *Search for an H-dibaryon with mass near 2m_Lambda in Y(1S) and Y(2S) decays*, Phys. Rev. Lett. 110, 222002 (2013), arXiv:1302.4028[hep-ex].

[9] J. Badier et al., *Mass and lifetime limits on new long-lived particles in 300 GeV/c $\pi-$ interactions,* (NA3), Z. Phys. C31, 21 (1986).

[10] R. H. Bernstein et al., *Search for new, long-lived, neutral particles,* Phys. Rev. D37, 3103 (1988).

[11] J. Belz et al. , *Search for the Weak Decay of an H Dibaryon,* (BNL-E888) Phys. Rev. Lett. 76, 3277 (1996), [Phys. Rev.C56,1164(1997)], arXiv:hep-ex/9603002[hep-ex].

[12] A. Alavi-Harati et al. (KTeV), *Search for the Weak Decay of a Lightly Bound H Dibaryon,* Phys. Rev. Lett. 84, 2593 (2000), arXiv:hep-ex/9910030[hep-ex].

[13] G. R. Farrar and G. Zaharijas, *Nuclear and nucleon transitions of the H di-baryon,* Phys. Rev. D70, 014008 (2004), arXiv:hep-ph/0308137[hep-ph]

[14] J. Beringer et al. (2012): *Particle listings* – K0 L, Available at: http://pdg.lbl.gov/2012/listings/rpp2012-list-K-zero-L.pdf

[15] C. Patrignani et al. (*Particle Data Group*), Chin. Phys. C, 40, 100001 (2016) and 2017 update. Available at: http://pdg.lbl.gov/

[16] J. Cleymans, *The Tsallis Distribution at the LHC,* arXiv:1210.7464v1[hep-ph]

[17] M.D. Azmi and J. Cleymans, *Transverse Momentum Distributions in proton - proton Collisions at LHC Energies and Tsallis Thermodynamics, arXiv: 1401. 4835[hep-ph]*

[18] *CMS Tracking POG Performance Plots For 2017 with PhaseI pixel detector,* Available at: https://twiki.cern.ch/twiki/bin/view/CMSPublic/TrackingPOGPerformance2017MC

[19] S. Vogel, *Introduction to Nuclear and Particle Physics. Nuclear models: Fermi-Gas Model Shell Model.* Available at: https://fias.uni-frankfurt.de/~svogel/lecture_ws_2011_12/slides_bratkovskaya_2.pdf

[20] S. Agostinelli et al., *GEANT4: A simulation Toolkit,* Nucl.Instrum.Meth A506 (2003) 250-303

[21] J. Allison et al., *Geant4 developments and applications,* IEEE Transactions on Nuclear Science 53 No. 1 (2006) 270-278

[22] J. Allison et al., *Recent developments in GEANT4,* Research Nucl.Instrum.Meth A 835 (2016) 186-225

[23] Torbjorn Sjostrand et al., *A Brief Introduction to PYTHIA 8.1,* Comput.Phys.Commun. 178 (2008) 852-867, arXiv:0710.3820

[24] Torbjorn Sjostrand et al., *PYTHIA 6.4 Physics and Manual*, JHEP 0605 (2006) 026, arXiv:hep-ph/0603175v2

[25] CMS Collaboration, *Description and performance of track and primary-vertex reconstruction with the CMS tracker,* JINT 9 (2014) P10009, arXiv:1405.6569[physics.ins-det]

[26] Karl Jakobs and Chris Seez, 2015, *The Higgs Boson discovery*, Available at: http://www.scholarpedia.org/article/The_Higgs_Boson_discovery

[27] S. Gorbunov, *Primary vertex fit based on the Kalman filter,* Available at: https://web-docs.gsi.de/~ikisel/reco/CBM/DOC-2006-Jan-19-1.pdf

[28] The CMS Collaboration, *Measurement of the inelastic proton-proton cross section at* $\sqrt{s} =$ 13TeV, Available at https://cds.cern.ch/record/2145896/files/FSQ-15-005-pas.pdf

[29] *Measurement of the structure of the inner tracking detector of the CMS experiment using nuclear interactions with data collected in 2015*, Available at: https://twiki.cern.ch/twiki/bin/view/CMSPublic/TrackerMaterialPosition2015

[30] C.P. Burgess, *Goldstone and Pseudo-Goldstone Bosons in Nuclear, Particle and Condensed-Matter Physics,* Phys.Rept.330:193-261,2000 arXiv:hep-th/9808176

[31] *Reconstruction of the Beam Spot*, Available at: https://twiki.cern.ch/twiki/bin/view/CMSPublic/SWGuideFindingBeamSpot

[32] Xabier Cid Vidal, *Luminosity - Taking a closer look at LHC,* Available at: https://www.lhc-closer.es/taking_a_closer_look_at_lhc/0.luminosity

[33] Xabier Cid Vidal, *Cross section - Taking a closer look at LHC*, Available at: https://www.lhc-closer.es/taking_a_closer_look_at_lhc/0.cross_section

[34] Dave Barney, 2004, *Illustration of CMS detector*, Available at: https://www.researchgate.net/figure/Illustration-of-the-detection-of-particles-at-the-CMS-experiment-Barney-2004-Each_fig1_260003686?_sg=L4EhPvs0iw-7ijfF7PCimHmnP_WLsZDn1k0rGKs2p7Zf08A0pZmFekmejJox59ZhuO86cpD5RKrgfb_dcal6gQ

[35] CMS Collaboration, *The CMS experiment at the CERN LHC*, JINST3(2008)S08004,doi:10.1088/1748-0221/3/08/S08004.

[36] Wolfgang Adam, *Track and vertex reconstruction in CMS,* Dated: 1 August 2007, Available at: http://www.hephy.at/project/cms/trigger/globalTrigger/trans/MEDIEN/Publications/CMSBooklet/Info_for_CMSBooklet/adam_trackvertexreco.pdf

[37] *A Kinematic fit and a decay chain reconstruction library*, Available at: https://twiki.cern.ch/twiki/pub/CMSPublic/SWGuideKinematicVertexFit/CMS_IN_2004_20.pdf

[38] CMS collaboration, *Observation of Long-Range Near-Side Angular Correlations in Proton-Proton Collisions at the LHC, JHEP 1009 (2010) 091, arXiv: 1009. 4122[hep-ex]*

[39] CMS Collaboration, *Pseudorapidity distribution of charged hadrons in proton-proton collisions at* $\sqrt{s} = 13$TeV, arXiv:1507.05915[hep-ex], Phys.Lett. B751 (2015) 143-163

[40] Paul Avery, *Vertexing and Kinematic Fitting, Part I: Basic Theory*, Available at: `https://www.phys.ufl.edu/~avery/fitting/kinfit_talk1.pdf`

[41] R. Armenteros and J. Podolanski, *Armenteros-Podolanski Plot*, Available at: `http://www.star.bnl.gov/~gorbunov/main/node48.html`

[42] TOTEM Collaboration, *First measurement of elastic, inelastic and total cross-section at* $\sqrt{s}$*=13 TeV by TOTEM and overview of cross-section data at LHC energies, arXiv: 1712.06153[hep-ex]* , Submitted to Phys.Rev.D

Appendix A

Additional histograms

A.1 Passed and total histograms for the reconstruction efficiencies

A.1.1 Transversal momentum

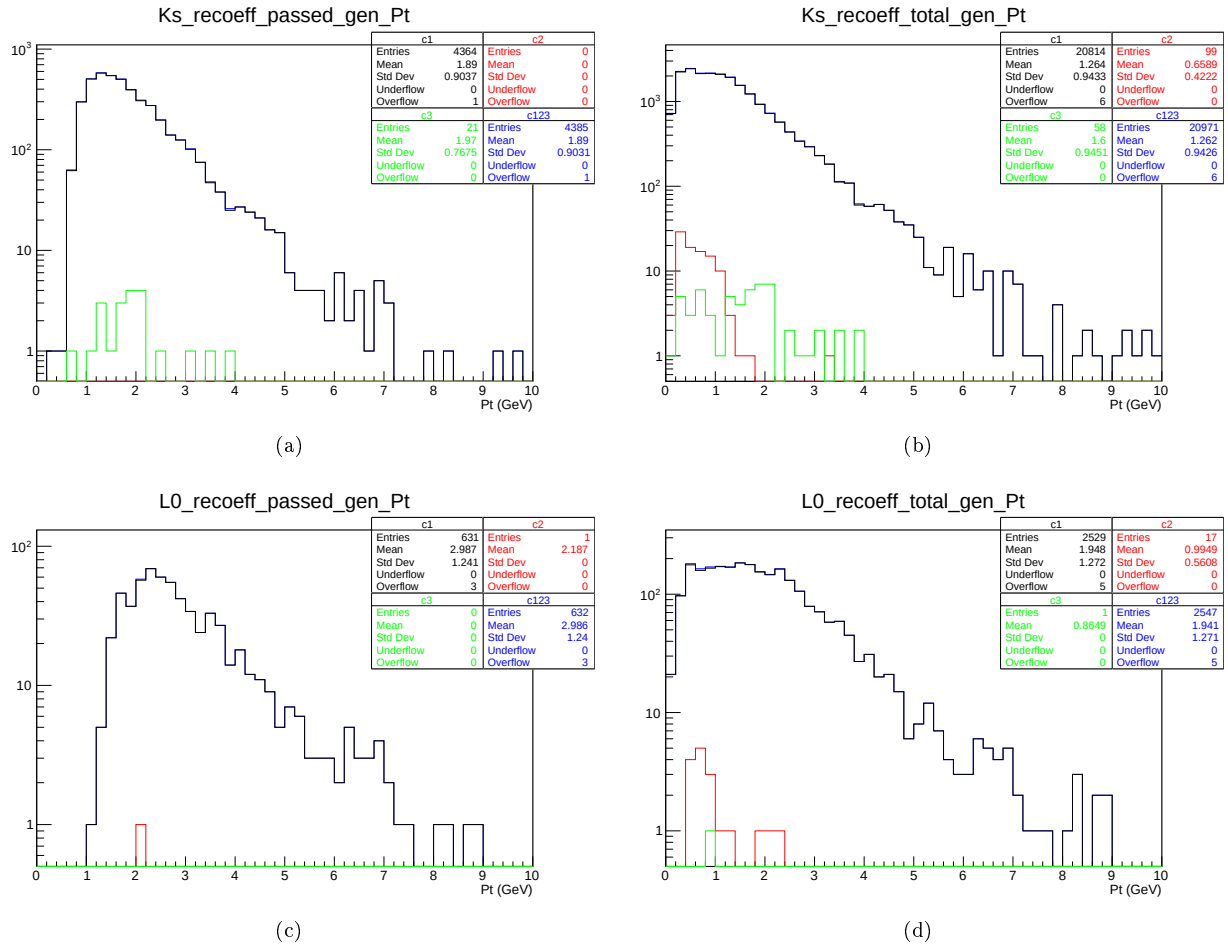

Figure A.1: The passed and total histograms for the Λ^0 and K_s^0 reconstruction efficiency plots in function of the p_T of the generator level particles with which the candidate reconstructed K_s^0 and Λ^0 are matched.

A.1.2 Pseudorapidity

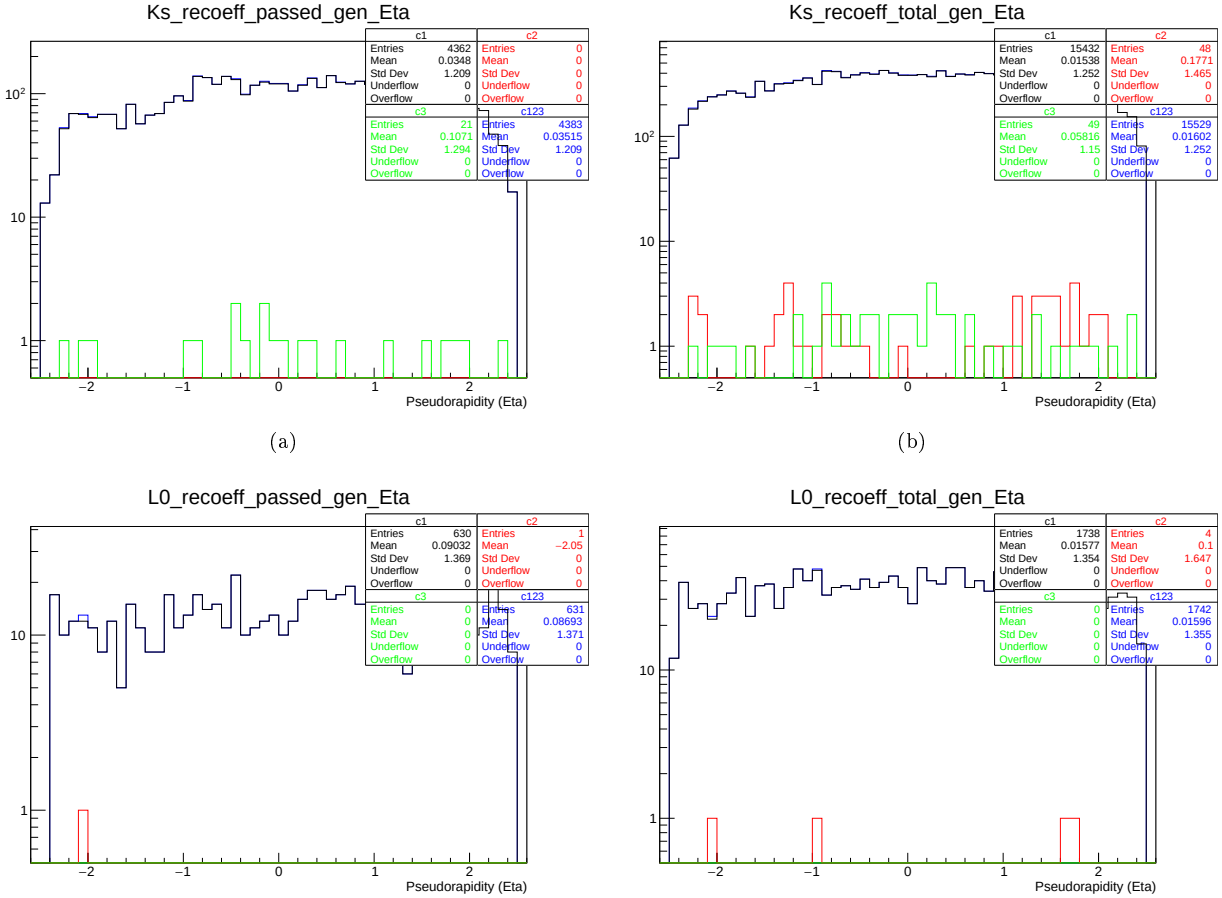

Figure A.2: The passed and total histograms for the Λ^0 and K_s^0 reconstruction efficiency plots in function of the pseudorapidity of the generator level particles with which the candidate reconstructed K_s^0 and Λ^0 are matched.

A.1.3 Reco efficiencies - dz

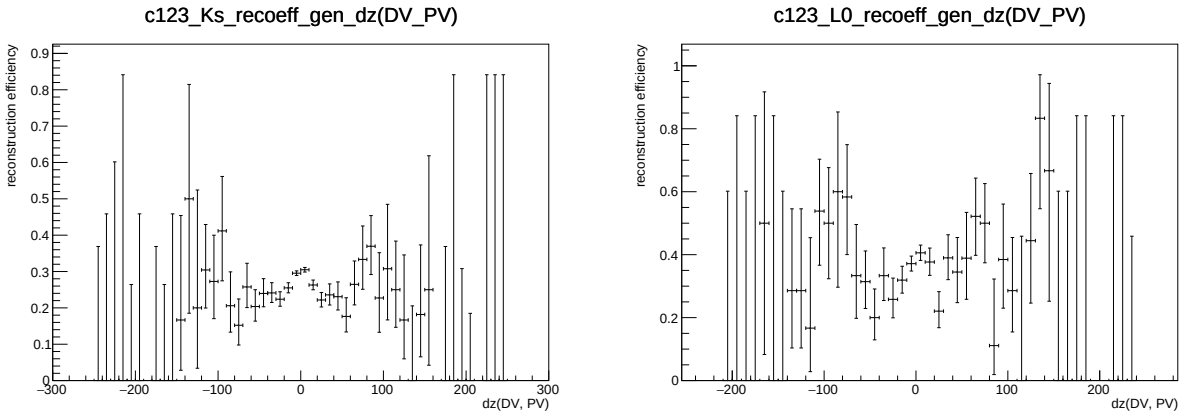

(a) (b)

Figure A.3: Reconstruction efficiencies of the K_s^0 and the Λ^0 in function of distance in the z-coordinate between the PV and the K_s^0 or Λ^0 decay vertex.

A.2 Primary vertex distribution

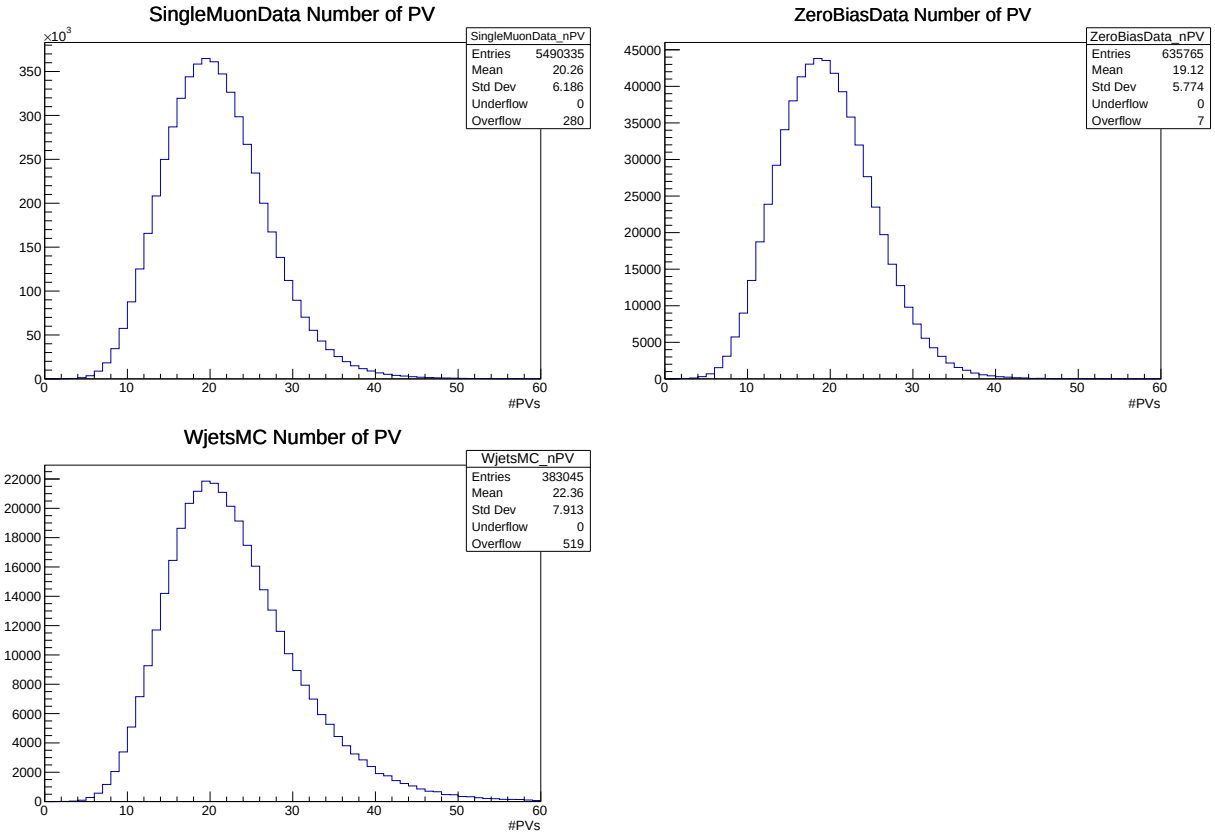

Figure A.4: The distribution of the number of primary vertices per event in the Single Muon data sample, the Zero Bias data sample and the W jets MC sample. The average number of primary vertices is per event is approximately 20.

A.3 S candidate daughters delta distributions with dz to PV0 cuts

A.3.1 dz PCA to PV0 above 1mm

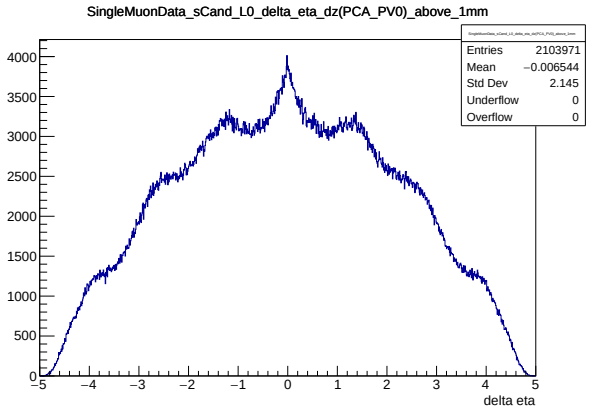

(a)

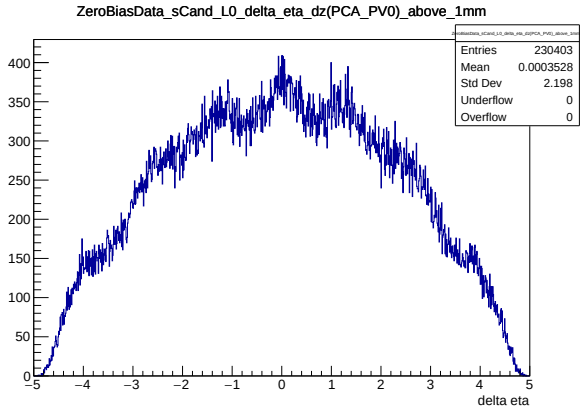

(b)

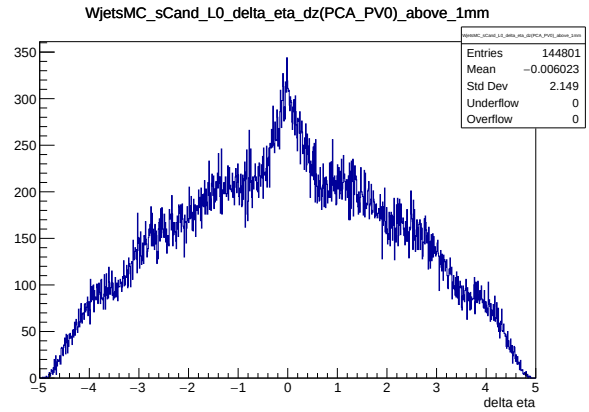

(c)

Figure A.5: These figures show the distributions of $\Delta\eta = \eta_{K_s^0} - \eta_{\Lambda^0\left(\bar{\Lambda}^0\right)}$ between the S candidates' daughter K_s^0 and $\Lambda^0\left(\bar{\Lambda}^0\right)$, with a cut on the distance in the z direction between PCA of the extrapolated S candidates' momentum to the $PV\,(0)$, and the $PV\,(0)$ itself. This distance has to be greater that 1mm. This is done for the Single Muon data sample, the W jets Monte Carlo sample, and the Zero Bias data sample.

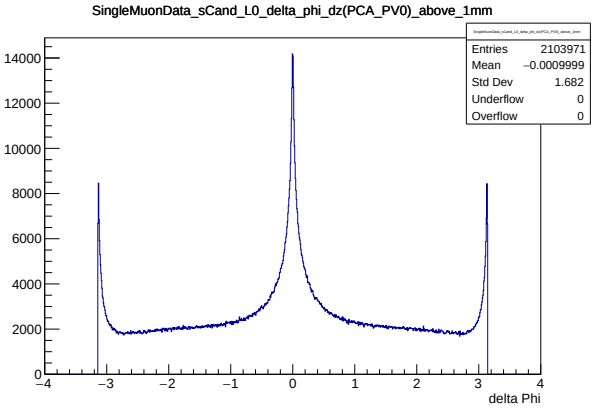

(a)

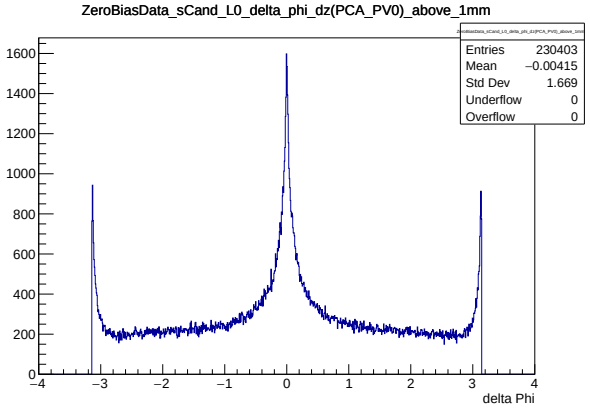

(b)

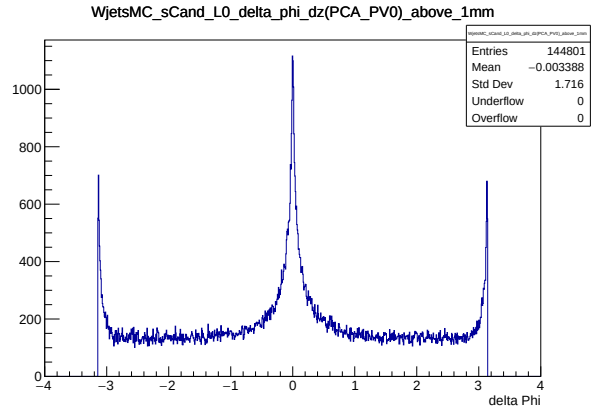

(c)

Figure A.6: These figures show the distributions of $\Delta\phi = \phi_{K_s^0} - \phi_{\Lambda^0\left(\bar{\Lambda}^0\right)}$ between the S candidates' daughter K_s^0 and $\Lambda^0\left(\bar{\Lambda}^0\right)$, with a cut on the distance in the z direction between PCA of the extrapolated S candidates' momentum to the $PV\,(0)$, and the $PV\,(0)$ itself. This distance has to be greater that 1mm. This is done for the Single Muon data sample, the W jets Monte Carlo sample, and the Zero Bias data sample.

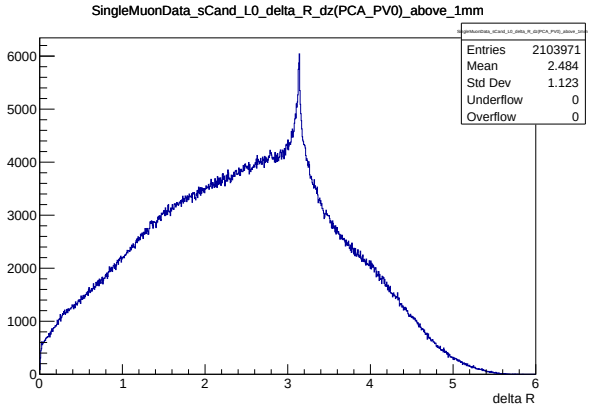

(a)

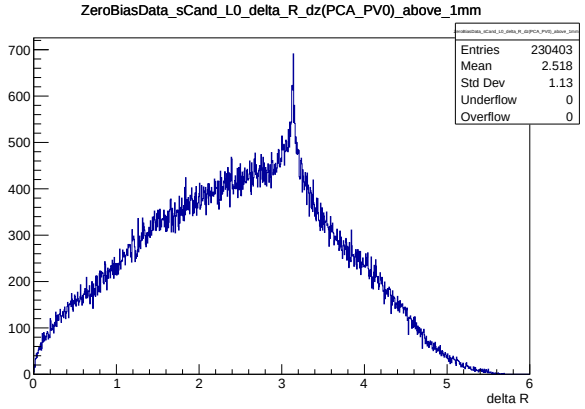

(b)

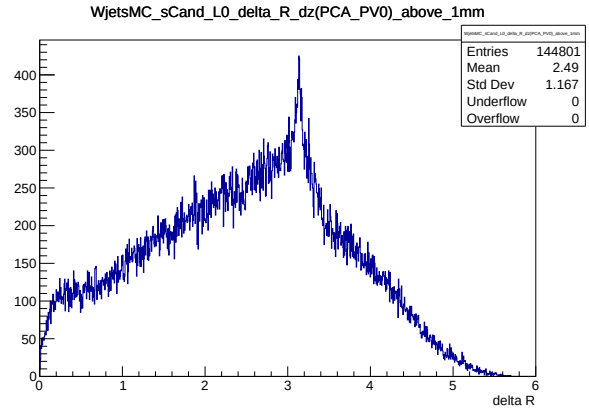

(c)

Figure A.7: These figures show the distributions of $\Delta R = \sqrt{\Delta\phi^2_{K^0_s,\Lambda^0} + \Delta\eta^2_{K^0_s,\Lambda^0}}$ between the S candidates' daughter K^0_s and Λ^0 $\left(\bar{\Lambda}^0\right)$, with a cut on the distance in the z direction between PCA of the extrapolated S candidates' momentum to the $PV\,(0)$, and the $PV\,(0)$ itself. This distance has to be greater that 1mm. This is done for the Single Muon data sample, the W jets Monte Carlo sample, and the Zero Bias data sample.

A.3.2 dz PCA to PV0 below 1mm

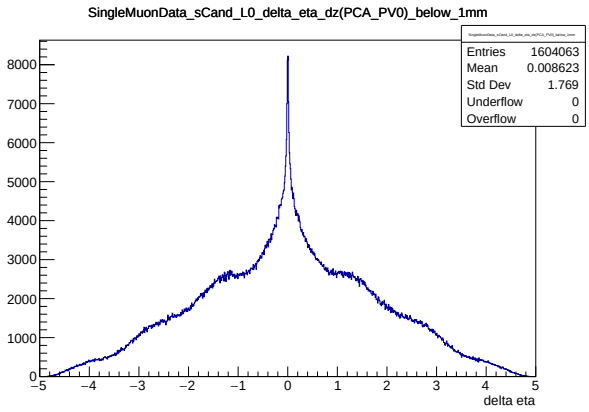

(a)

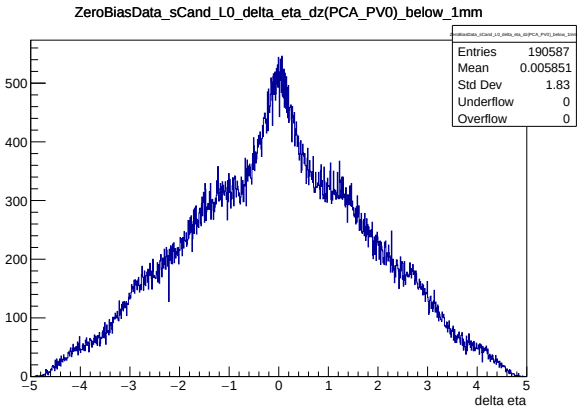

(b)

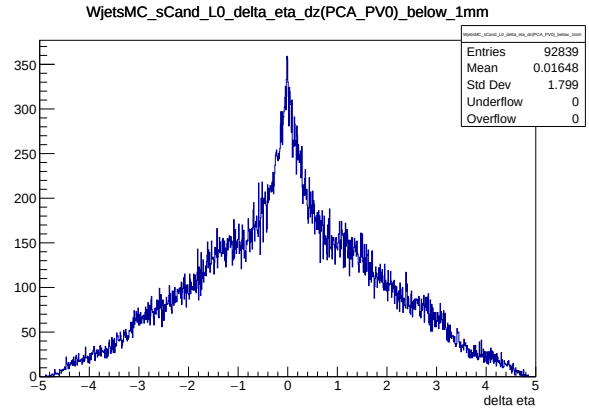

(c)

Figure A.8: These figures show the distributions of $\Delta\eta = \eta_{K_s^0} - \eta_{\Lambda^0}$ between the S candidates' daughter K_s^0 and Λ^0, with a cut on the distance in the z direction between PCA of the extrapolated S candidates' momentum to the $PV\,(0)$, and the $PV\,(0)$ itself. This distance has to be less that 1mm. This is done for the Single Muon data sample, the W jets Monte Carlo sample, and the Zero Bias data sample.

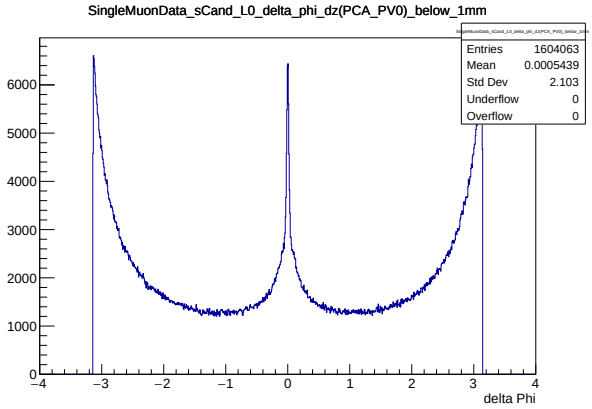

(a)

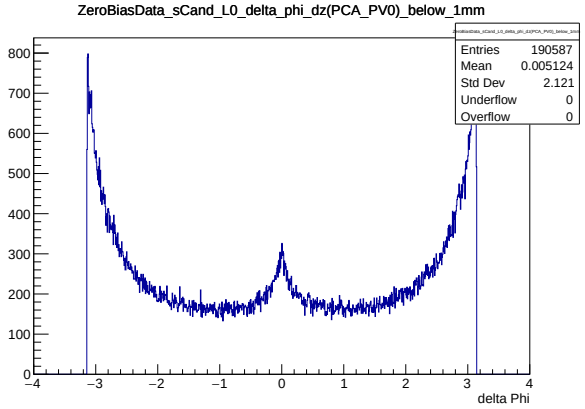

(b)

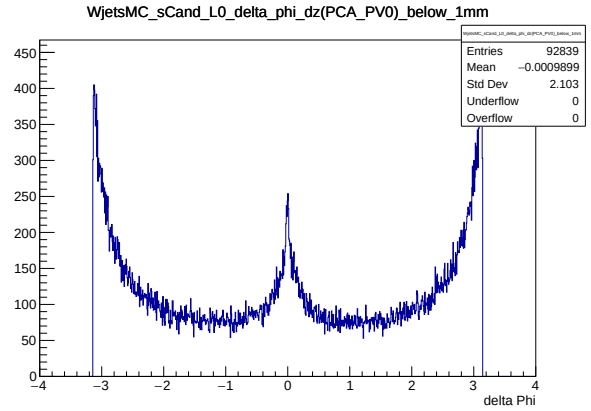

(c)

Figure A.9: These figures show the distributions of $\Delta\phi = \phi_{K_s^0} - \phi_{\Lambda^0\left(\bar{\Lambda}^0\right)}$ between the S candidates' daughter K_s^0 and Λ^0 $\left(\bar{\Lambda}^0\right)$, with a cut on the distance in the z direction between PCA of the extrapolated S candidates' momentum to the $PV\,(0)$, and the $PV\,(0)$ itself. This distance has to be less that 1mm. This is done for the Single Muon data sample, the W jets Monte Carlo sample, and the Zero Bias data sample.

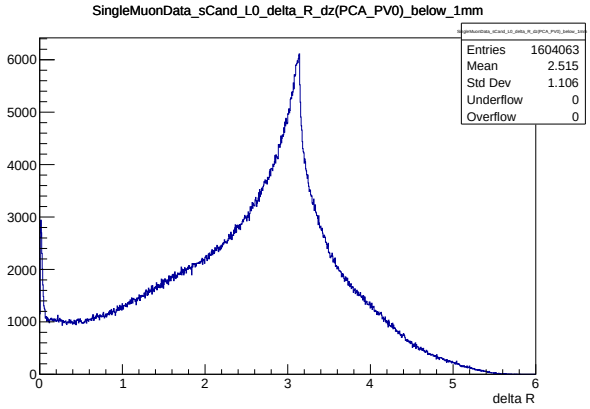

(a)

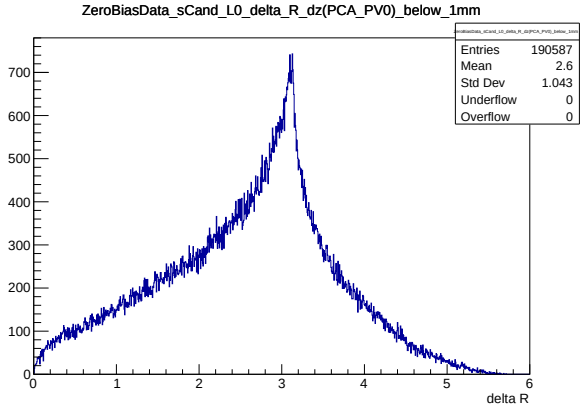

(b)

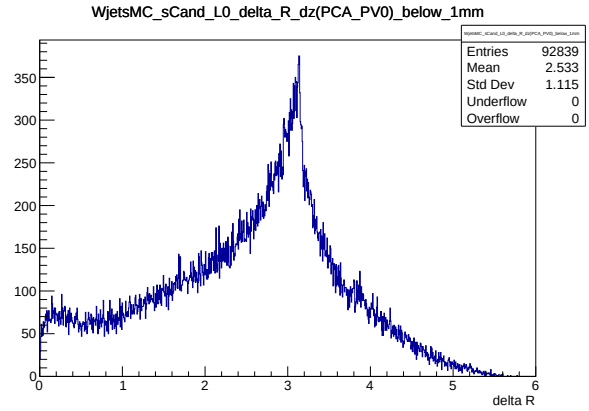

(c)

Figure A.10: These figures show the distributions of $\Delta R = \sqrt{\Delta\phi^2_{K^0_s,\Lambda^0} + \Delta\eta^2_{K^0_s,\Lambda^0}}$ between the S candidates' daughter K^0_s and Λ^0 $\left(\bar{\Lambda}^0\right)$, with a cut on the distance in the z direction between PCA of the extrapolated S candidates' momentum to the $PV\,(0)$, and the $PV\,(0)$ itself. This distance has to be less that 1mm. This is done for the Single Muon data sample, the W jets Monte Carlo sample, and the Zero Bias data sample.

A.4 S candidate position scatter plots

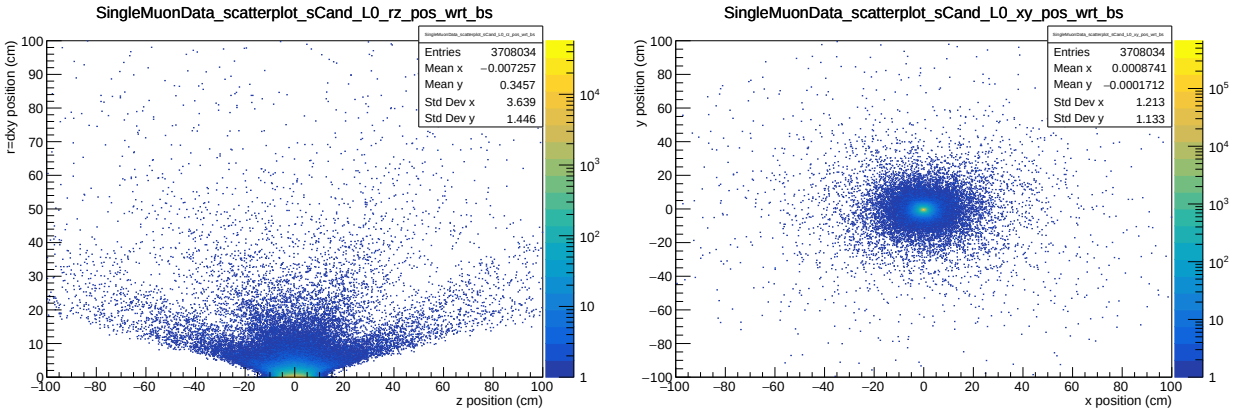

(a) (b)

Figure A.11: Two dimensional scatter plots of the fitted S candidate's vertex position with respect to the beamspot. The first sub-figure has the position in the z direction on the x-axis and the radius in the xy-plane on the y-axis. The second figure has the x position on the x-axis and the y-position on the y-axis. This is for the Single Muon data sample. The Zero Bias data sample and W jets Monte Carlo sample show similar results.

A.5 S candidate K_s^0 and Λ^0 daughter p_T and η distributions

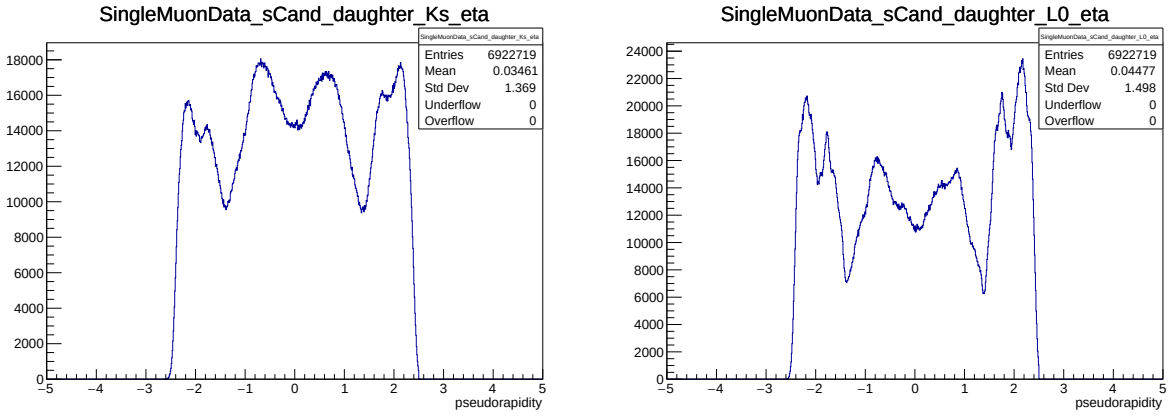

Figure A.12: The η distributions of the S candidate's K_s^0 and Λ^0 daughters in Single Muon data. This is only for S candidates involving a Λ^0 and not an $\bar{\Lambda}^0$.

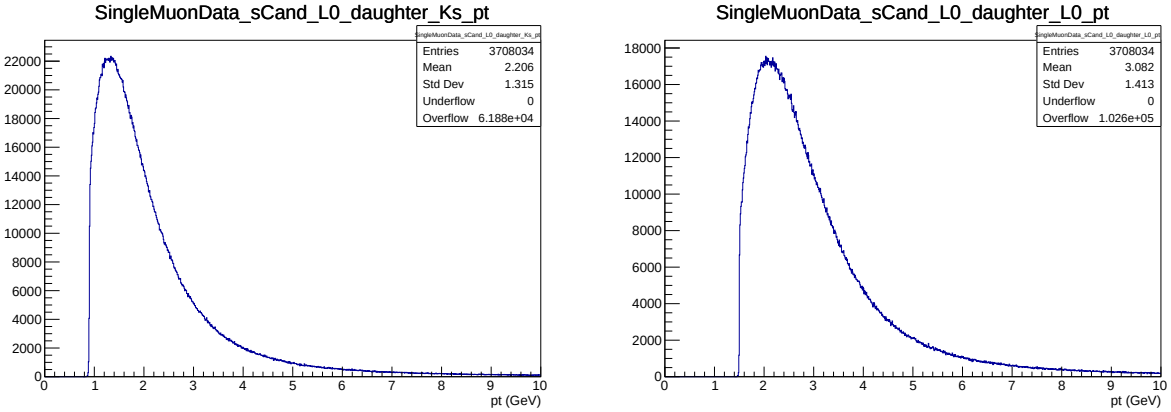

Figure A.13: The p_T distributions of the S candidate's K_s^0 and Λ^0 daughters. This is only for S candidates involving a Λ^0 and not an $\bar{\Lambda}^0$. The cut-offs reflect the cut at 0.9GeV and 1.5GeV as discussed previously. This is for the Single Muon data sample.

A.6 $\Delta\phi - \Delta\eta$ scatter plots

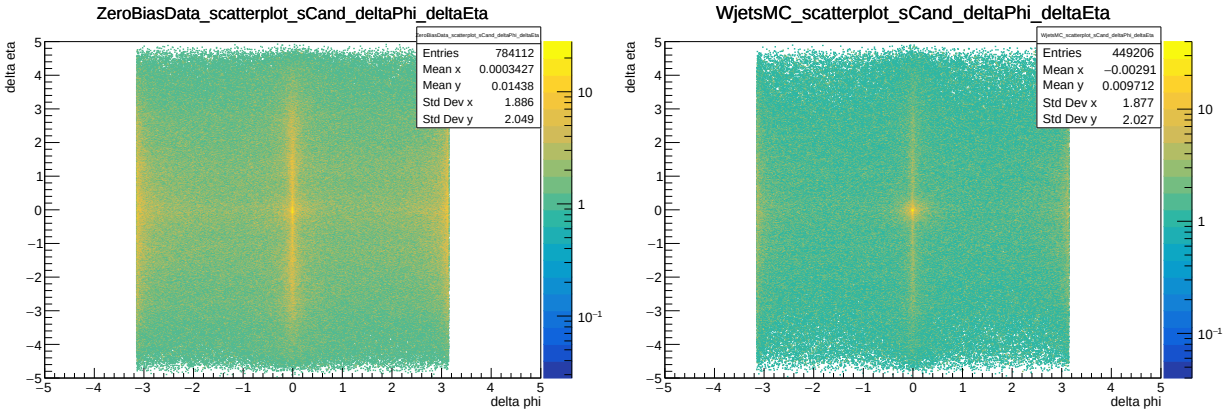

Figure A.14: A 2D scatter plot between S candidate's $\Delta\phi$ and $\Delta\eta$ for the Zero Bias data and W+jets Monte Carlo samples.